SYNTHESIS OF TIN, SILVER AND THEIR ALLOY NANOPARTICLES FOR LEAD-FREE INTERCONNECT APPLICATIONS

A Thesis
Presented to
The Academic Faculty

by

Hongjin Jiang

In Partial Fulfillment
of the Requirements for the Degree
Doctor of Philosophy in the
School of Chemistry and Biochemistry

Georgia Institute of Technology
April 2008

SYNTHESIS OF TIN, SILVER AND THEIR ALLOY NANOPARTICLES FOR LEAD-FREE INTERCONNECT APPLICATIONS

Approved by:

Dr. C. P. Wong, Advisor
School of Materials Science and Engineering
Georgia Institute of Technology

Dr. Z. John Zhang
School of Chemistry and Biochemistry
Georgia Institute of Technology

Dr. Boris Mizaikoff
School of Chemistry and Biochemistry
Georgia Institute of Technology

Dr. Z. L. Wang
School of Materials Science and Engineering
Georgia Institute of Technology

Dr. Rigoberto Hernandez
School of Chemistry and Biochemistry
Georgia Institute of Technology

Date Approved: March 24, 2008

ACKNOWLEDGEMENTS

I would like to express my sincere gratitude to my advisor, Dr. C. P. Wong for his guidance, inspiration, and financial support throughout the course of this research. He always encouraged me to work hard and at the same time gave me the freedom to direct my progress. I would also like to extend my gratitude to Dr. Z. L. Wang, Dr. Rigoberto Hernandez, Dr. Boris Mizaikoff and Dr. Z. John Zhang for serving on my Ph. D committee as well as providing important instructions and recommendations. I very appreciate the helps from the faculty and staff members in the School of Chemistry and Biochemistry, especially Dr. Cam Tyson, School of Materials Science and Engineering and National Science Foundation Microsystems Packaging Research Center too.

My special thanks go to my fellow co-workers in Dr. Wong's group, especially Dr. Kyoung-sik Moon. He has always been working with me on all my research projects, providing me invaluable suggestions and helps. I also received discussions and helps from Dr. Zhuqing Zhang, Dr. Jianwen Xu, Dr. Hai Dong, Dr. Yangyang Sun, Dr. Lingbo Zhu, Dr. Yi Li, Ms. Jiongxin Lu, Mr. Yonghao Xiu, Ms. Gusuel Yun, Mr. Qizhen Liang, Mr. Rongwei Zhang, Mr. Wei Lin and Mr. Owen Hildreth. I would like to thank the undergraduate students who worked with me during the PhD study too. They are Mr. Taylor Giddens, Mr. John D Brown, Ms. Katy Lin and Ms. Jessey Huang.

I would like to acknowledge Dr. Z. L. Wang and Dr. Yong Ding for their helps on the high resolution transmission electron microscopy training and image analysis.

Special appreciation is extended to Intel Corporation and National Science Foundation for their interests and supports on this work.

Finally, I would like to thank my family for their continuous support and encouragement throughout my Ph.D. study.

TABLE OF CONTENTS

LIST OF TABLES

LIST OF FIGURES

SUMMARY

SnPb solders have long been used as interconnect materials in microelectronic packaging. Due to the health threat of lead to human beings, the use of lead-free interconnect materials is imperative. Three kinds of lead-free interconnect materials are being investigated, namely lead-free metal solders (SnAg, SnAgCu, etc.), electrically conductive adhesives (ECAs) and carbon nanotubes (CNTs). However, there are still limitations for the full utilization of these lead-free interconnect materials in the microelectronic packaging, such as higher melting point of lead-free metal solders, lower electrical conductivity of the ECAs and poor adhesion of CNTs to substrates.

This thesis is devoted to the research and development of low processing temperature lead-free interconnect materials for microelectronic packaging applications with an emphasis on fundamental studies of nanoparticles synthesis, dispersion and oxidation prevention, and nanocomposites fabrication.

Oxide-free tin (Sn), tin/silver (96.5Sn3.5Ag) and tin/silver/copper (96.5Sn3.0Ag0.5Cu) alloy nanoparticles with different sizes were synthesized by a low temperature chemical reduction method. Both size dependent melting point and latent heat of fusion of the synthesized nanoparticles were obtained. The nano lead-free solder pastes/composites created by dispersing the SnAg or SnAgCu alloy nanoparticles into an acidic type flux spread and wet on the cleaned copper surface at 220 to 230 ^{o}C. This study demonstrated the feasibility of nano sized SnAg or SnAgCu alloy particle pastes for low processing temperature lead-free interconnect applications in microelectronic packaging.

Surface functionalized silver nanoparticles and silver fakes were used as fillers for electrically conductive adhesives (ECAs) applications. During the curing of epoxy resin (150 ^{o}C), the surfactants were debonded from the particles and at the same time the oxide layers on the particle surfaces were removed which facilitated the sintering of Ag nanoparticles. The contact interfaces between fillers were significantly reduced and an ultra highly conductive ECA with a resistivity of 5×10^{-6} Ω.cm was obtained.

To enhance the adhesion of carbon nanotube (CNT) films to substrates, an ultra highly conductive ECA were used as a media to transfer the CNT films to copper substrates. The polymer wetted along the CNTs during curing process by the capillary force. An ohmic contact was formed between the copper substrates and the transferred CNTs. This process could overcome the serious obstacles of integration of CNTs into integrated circuits and microelectronic device packages by offering low processing temperatures and improved adhesion of CNTs to substrates. The transferred CNTs can be used to simultaneously form electrical and mechanical connections between chips and substrates.

CHAPTER I

INTRODUCTION AND BACKGROUND

1.1 Brief Introduction of Electronic Packaging

The major function of electronic packaging is to protect, power and cool the microelectronic chips or components and provide electrical and mechanical connections between the microelectronic parts and the outside world. The detailed functions of the electronic packaging are: (1) to provide a path for electric current that power the circuits on the IC; (2) to distribute the signals on and off of the IC chip; (3) to remove the heat generated by circuits on the IC and (4) to support and protect the IC chip from hostile environment.

Packaging is an art based on the science of establishing interconnections ranging from first-level packaging to second-level packaging and third level packaging (Figure 1.1.1) [1]. First-level packaging refers to the techniques and processes to establish the interconnections between an IC chip and the substrate. The main interconnection techniques used for first-level packaging are flip-chip, wire bonding and tape automated bonding (TAB). Second-level packaging consists of the processes and technologies to establish the interconnections between the first-level package and a printed wiring board (PWB). The current second-level packaging technologies include pin through hole (PTH), peripheral surface mount technology (SMT) and surface mount array (SMA) technology. Third-level package is the process to incorporate the second-level packages onto a motherboard.

The packaging technologies are under fast evolutions nowdays due to the dramatic changes in the electronics industry. With the requirements toward low cost,

miniaturization and high performance, the IC chips can be connected to the integrated board directly by using flip-chip technology [2].

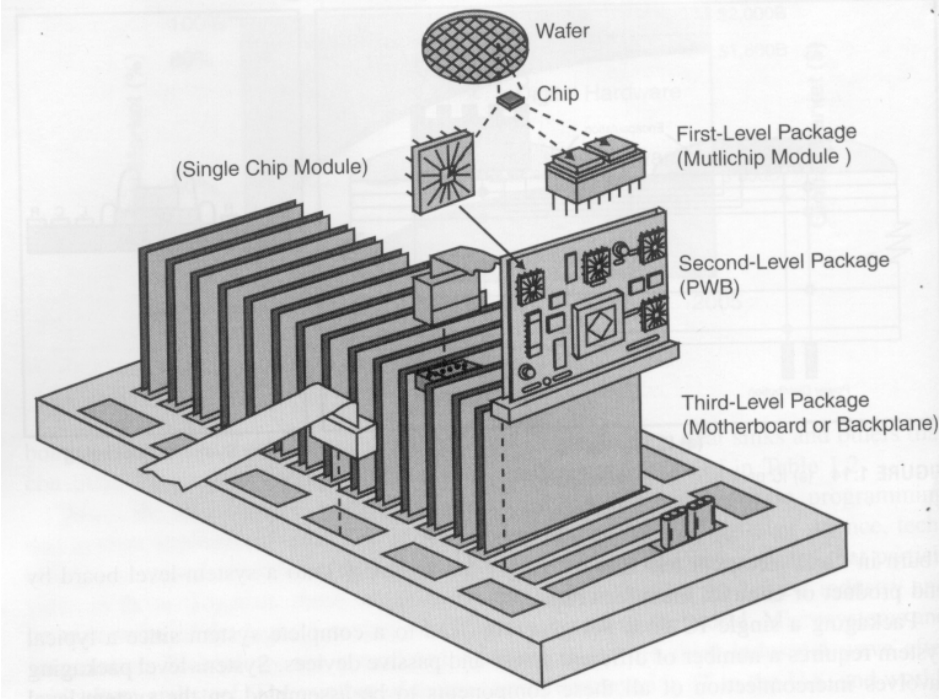

Figure 1.1.1 The electronic packaging hierarchy.

Flip-chip technology is a face-down attachment of the active side of the silicon die onto the substrate through solders. The generic concept of flip-chip technology is schematically shown in Figure 1.1.2. Flip-chip technology provides many advantages over wire bonding and tape automated bonding, such as high I/O density, short interconnections, self-alignment, better heat dissipation from the back of the die, smaller foot print area, lower profile, fewer assembly steps and easy handle before assembly. The flip-chip technology can either be used inside a package or directly on a substrate. If used inside a package, the chip is connected to a redistribution interposer through solder joints. This technique is called flip-chip in package (FCIP). The chip can also be directly

connected to a PWB through the solder joints, which is called flip-chip on board (FCOB) or direct chip attach (DCA).

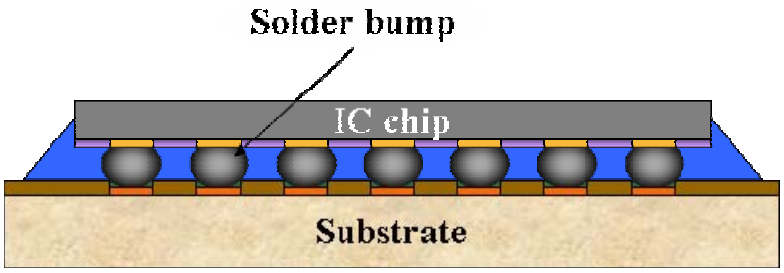

Figure 1.1.2 Schematic of Flip-chip package.

1.2 Solders

Although the electronics industry has made considerable advances over the past few decades, the essential requirements of communications among all types of components in all electronic systems remain unchanged. Components need to be electrically connected for power, ground and signal transmissions. Tin/lead (Sn/Pb) solder alloys have been used as the interconnect material in most areas of electronic packaging for a long time, including interconnection technologies such as pin through hole (PTH), surface mount techniques (SMT), ball grid array (BGA), chip scale packaging (CSP) (Figure 1.2.1), flip chip, etc.

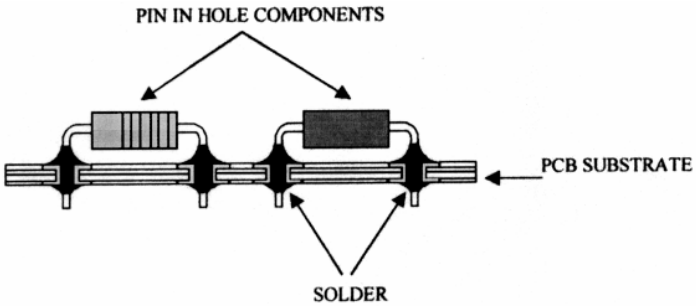

Figure 1.2.1 Schematic structures of PTH, SMT and BGA packages using solder interconnects.

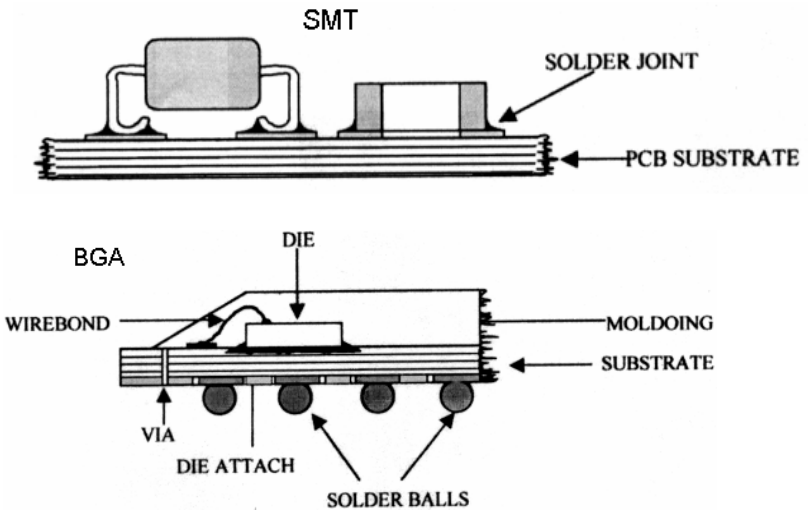

Figure 1.2.1 Continued

Many types of solder materials are available for the electronics interconnect, such as paste, wire, ball, bead, ingot and ribbon/foil. The solder paste is a mixture of over 90% of pre-alloyed solder powders and a chemical flux-vehicle that has a creamy, butter-like consistency. The flux-vehicle portion of the paste is made with rosin or resin, activators, viscosity control additives, flux chemicals, stabilizers and solvents. Solder pastes have been commonly used in electronics assembly for printed wiring board (PWB) assembly in surface mount technology applications. Pastes can be “printed” through a stencil onto the circuit pads. After printing, components are placed onto the bonding pad areas of the circuit and are held temporarily by the tackiness of the paste. Boards are then sent through a reflow oven where a specific temperature profile evaporates the solvent, activates the flux, and melts the solder alloy. The type of flux used is dependant upon the desired activity and whether cleaning is an option.

The three basic flux formulations are: a) No-clean, b) Rosin, Mildly Activated (RMA) and c) Water-Soluble. The No-clean formulations are mildly active fluxes which produce

nonconductive and non-corrosive post-soldering residues that can be safely left on the assembly with no corrosion concern, and cleaning is not required. No-clean flux residues can be removed after soldering if desired. Cleaning procedures are generally similar to RMA flux residue removal. RMA formulations were precursors to No-clean formulations. However, the RMA flux residues may be conductive and/or corrosive after soldering. Removal of the flux residues is recommended. RMA flux residues, being rosin-based and organic in nature, are generally removed with a solvent. The Water-Soluble fluxes are higher activity fluxes designed for removal after soldering. The flux residues can be cleaned with water which is typically heated and applied by a pressurized spray. Water-soluble flux residues are corrosive and conductive after soldering, therefore removal is mandatory.

There are increasing concerns nowadays about the use of tin/lead alloy solders. Lead, a major component in solder, has long been recognized as a health threat to human beings. The major concern is that lead from discarded consumer electronics products in landfills could leach into underground water and eventually into drinking water system (Figure 1.2.2) [3]. According to the latest report [US Geological Survey, 2001], the total lead consumption by the US industries was 52,400 metric tons in 2000. More than 10% of that (5,430 metric tons) was used to produce solder alloys. Worst of all, most of the electronic products have a very short service life (e.g., cell phones, pagers, electronic toys, PDA, etc.), which often end up in landfills in just a few months or years. Recycling of lead-containing consumer electronic products has been proven to be very difficult, compared to that of lead-containing batteries or cathode ray tubes (CRT) displays. Therefore, the electronic manufacturers would prefer to use lead-free interconnect materials.

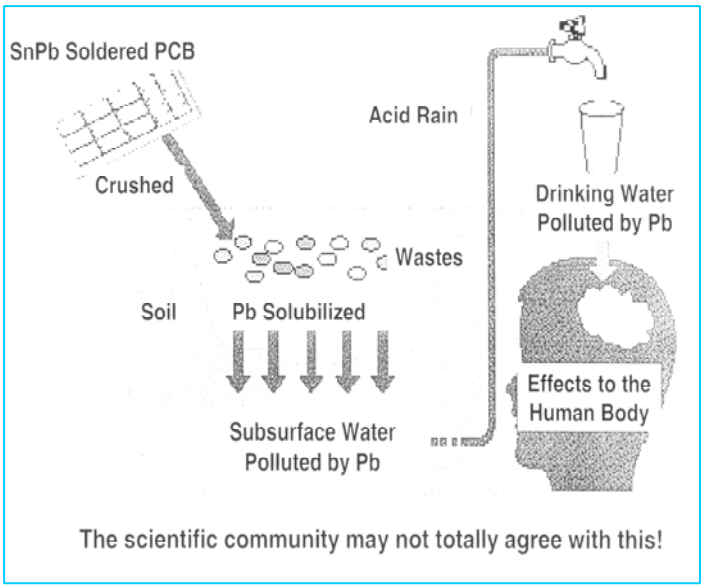

Figure 1.2.2 the schematic of how Pb from solder materials affects the human beings.

A variety of lead-free solder alloys have been investigated as potential replacements for tin lead solders. Lead-free candidates and their respective melting points are listed in Table .1. While there is broad agreement that there will be no decrease in replacement of tin lead with other alloys, two alloy families, tin-silver-copper (SnAgCu) and tin-copper (SnCu) seem to be generating the most interest. SnAgCu alloy composition (with or without the addition of a fourth element) appears to be the most popular replacement, which has also been chosen to be the benchmark, with SnPb being the baseline, for testing any other alloys to be included in the listing to be provided to the industry. Concerns with this alloy family include higher processing temperatures, poorer wettability due to their higher surface tension and their compatibility with lead bearing finishes. The SnCu alloy composition is a low cost alternative for wave soldering, and is compatible with most lead bearing finishes. Process considerations must be addressed with this alloy, which has a higher melting temperature than most SnAgCu alloys.

Table 1.2.1 Lead-free alloys

Alloys	Melting Point
Sn96.5Ag3.5	221 °C
Sn20Au80	280 (mainly used in interconnects for optoelectronic packaging)
Sn99.3/Cu0.7	227 °C
Sn96.5Ag3.0Cu0.5	217 °C
SnAgCuX(Sb, In)	Ranging according to compositions, usually above 210 °C
SnAgBi	Ranging according to compositions, usually above 200 °C
Sn95Sb5	232 – 240 °C
Sn91Zn9	199 °C
SnZnAgAlGa	189°C
Sn42Bi58	138 °C
Sn/Pb (comparison)	183 °C

As can be seen in Table 1.2.1, the melting points of the Sn/Ag/Cu and Sn/Cu alloys are more than 30 ~ 40 °C higher than that of the eutectic Sn/Pb alloy. Therefore, the reflow temperature for soldering components on assembly boards should be raised at least by 30 ~ 40 °C. The higher reflow temperature leads to higher thermal stress on components and substrates, which adversely affects their reliability. It is also considered likely to have an increased tendency of the pop-corning found in the plastic encapsulated ICs during the reflow process. In addition, the high required temperature brings the serious warpage issue of organic board substrates into focus. Furthermore, heat-sensitive components such as electrolytic capacitors might not survive the high processing temperatures in the lead-free assembly. The solders tend to be re-oxidized at high reflow temperatures and their wettability becomes worsened unless expensive nitrogen reflow is used. To obtain acceptable wetting of lead-free alloys, more aggressive and higher temperature flux chemicals are required, due to the fact that lead-free alloys have a much higher surface tension than the SnPb eutectic solder. Strong flux chemicals are, however, not preferred

for PWB boards due to their corrosive nature. In addition to the device reliability, a higher reflow temperature also requires higher power consumption, which results in higher cost. Therefore, novel approaches to suppress the melting point of lead-free alloys and improve the wettability are required, which result in various advantages such as device reliability, cost and energy saving.

1.3 Electrically Conductive Adhesives

Polymer-based conductive adhesives are proposed as one of the lead-free candidates, which composed of polymer matrix and conductive fillers. The conductive fillers provide the electrical properties and the polymer matrices provide the physical and mechanical properties. Comparing to conventional SnPb solders, the advantages of the conductive adhesives are low processing temperature, lower cost, environmental friendly, process simplicity and no subsequent cleaning steps, etc. However, there are several big issues which limit the utilization of ECAs in microelectronic packaging, such as lower electrical conductivity, unstable contact resistance and lack of re-workability.

There are three kinds of conductive adhesives: isotropic conductive adhesives (ICAs) [4], anisotropic conductive adhesives/films (ACAs/ACFs) [5] and nonconductive adhesives/films (NCAs/NCFs) [6]. The difference between ICAs and ACAs/NCAs is based on the percolation theory as shown in Figure 1.3.1. The ICAs generally consist of an epoxy resin with high loading of conductive fillers and conducts electricity equally in all directions (Figure 1.3.2 (a)). The ACAs/ACFs have lower conductive filler content and thus provide unidirectional conductivity in the vertical or Z direction (Figure 1.3.2 (b)). The NCAs/NCFs, on the other hand, do not consist of any conductive fillers, which

maintain pure mechanical contacts between the bumps and pads by the compressive force (Figure 1.3.2 (c)).

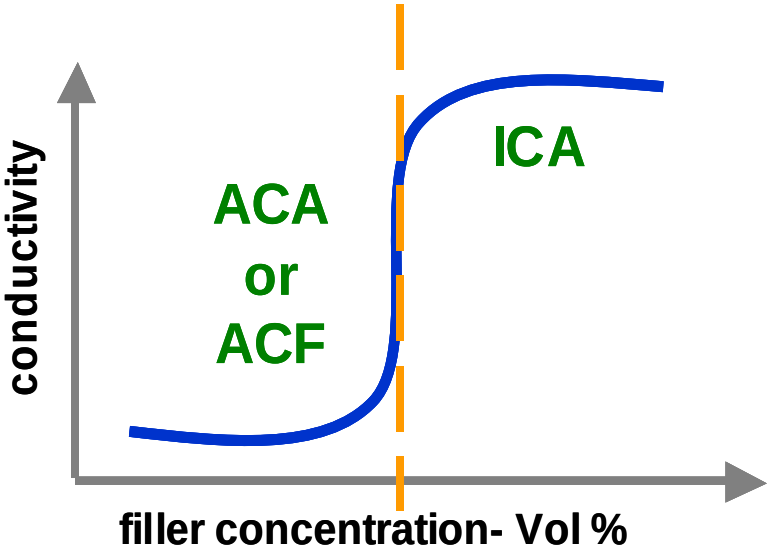

Figure 1.3.1 Typical percolation curve of conductive adhesives.

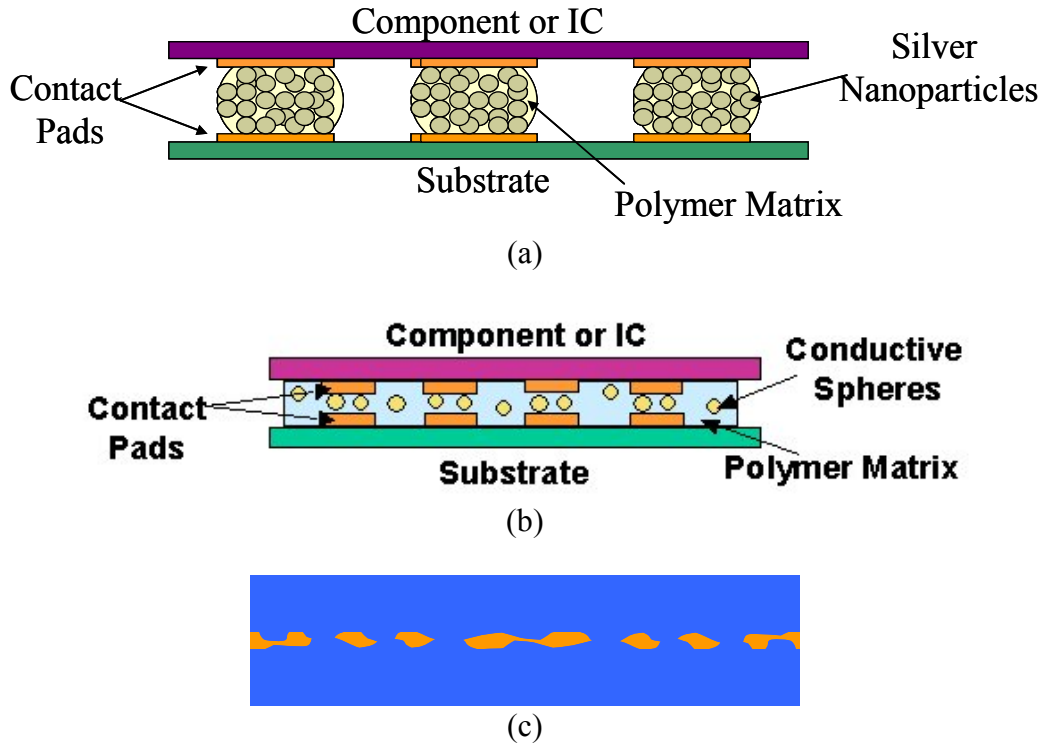

Figure 1.3.2 Schematic illustration of (a) ICA, (b) ACA/ACF and (c) NCA/NCF joints.

For ICAs to be used for flip-chip applications, it is necessary to apply them selectively on the contact pads which are to be electrically interconnected. To precisely print the ICA pastes, screen and stencil printing are most commonly used. Unlike the ACA flip-chip bonding process, a separate underfilling step would be required with ICA flip-chip bonding to improve the long-term reliability of the device. The difficulties for the ICA flip-chip bonding technology are poor processability and small process window in handling the flip-chip module directly after assembly.

For ACAs/NCAs to be used for flip-chip applications, due to the lower or absence of filler loading, heat and pressure are applied simultaneously to the stack-up until the particles or the contact pads are bridged together. Because of the anisotropy, ACAs/NCAs may be deposited over the entire contact pads, which greatly facilitate the materials application. Also the fine pitch applications can be easily achieved by using ACAs/or NCAs. The fine pitch capability of ACA/ACF is limited by the size of the conductive fillers, which can be several microns to a few nanometers in diameter.

Although the many advantages from ICAs, ACAs and NCAs, several limitations will hinder the wide applications of ECAs as the interconnect materials in microelectronic packaging, such as lower electrical conductivity, poor impact strength. Therefore, improving the electrical properties of ECAs is necessary.

1.4 Carbon Nanotubes as Interconnect Materials

Carbon nanotubes (CNTs) offer many promising characteristics for future electronic and device applications [7, 8] due to their extremely high thermal conductivities [9], outstanding mechanical properties [10] and very high electrical conductivities by the

ballistic effect. Although the ballistic transport in multiwalled CNTs (MWCNTs) displays an electrical resistance of 12.9 KΩ [11], an array or film of thousands of parallel CNTs can be used as a promising interconnect material in electronic and photonic devices. Till now, several chemical vapor deposition (CVD) methods have been developed to produce well aligned CNT films and arrays [12-14]. In these methods, almost every catalytic particle can produce a nanotube, and bundling of neighboring tubes leads to collective vertical growth due to the Van der Walls force among them. Recently, the synthesis of well aligned open-ended CNT films was reported [12]. The open-ended CNT films can improve the electrical conductance of MWCNTs because recent studies have demonstrated that the internal walls of MWCNTs can participate in the electrical transport as well, therefore enabling larger current carrying capability [15].

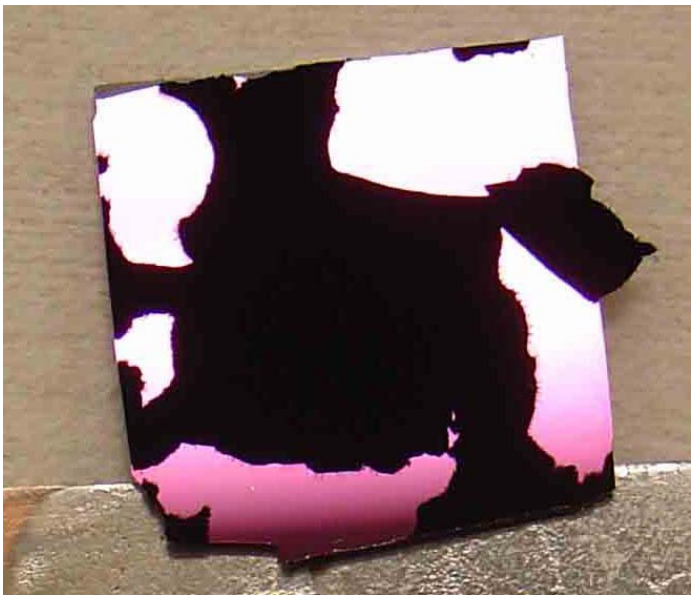

Figure 1.4.1 The delamination between the CNT film and substrate.

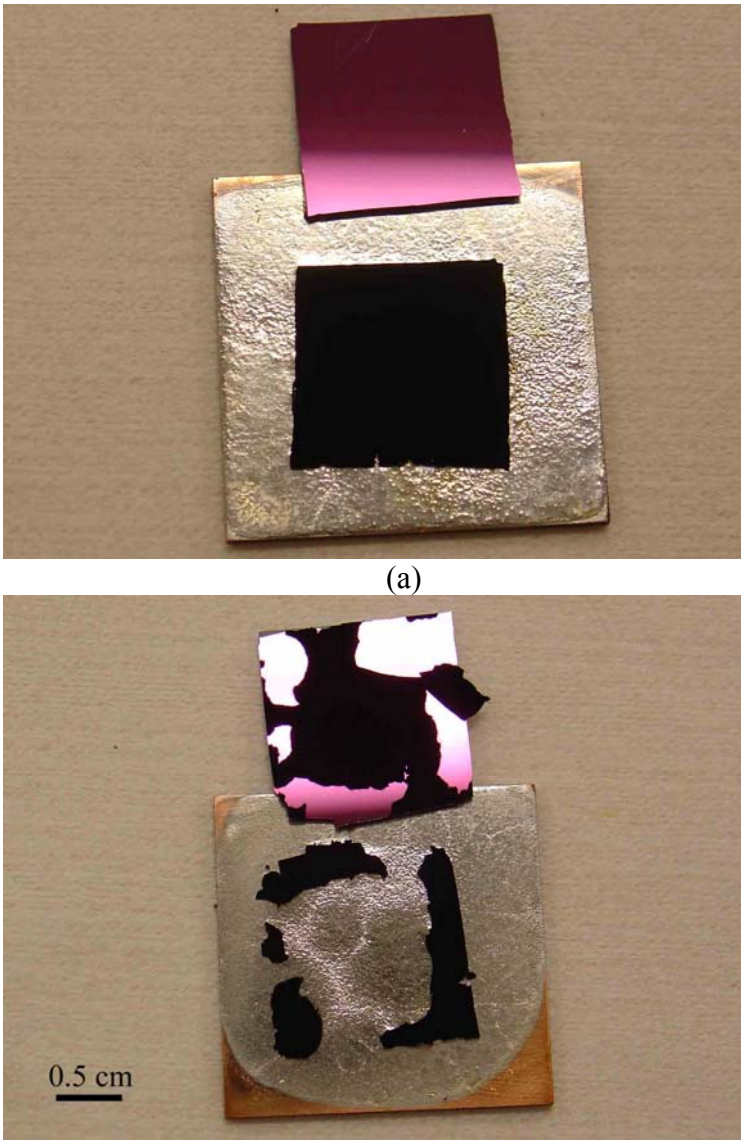

(a)

(b)

Figure 1.4.2 The transferred CNTs by SnPb solders: (a) the open-ended CNTs; (b) the close-ended CNTs.

Although CNTs have many excellent properties, there are still some limitations which hinder the full unitizations of CNTs as interconnect materials in microelectronic packaging, such as high processing temperature and poor adhesion between CNTs and substrates, etc. Figure 1.4.1 showed that the delamination happened between the CNT films and substrates sue to the poor adhesion of CNTs. The CNTs can not be directly

prepared on the chips, substrates and components due to its high processing temperature. The poor adhesion between CNTs and substrates will result in long term reliability issues and high contact resistance.

Therefore, a novel CNT transfer process is necessary, rather than directly grow the CNTs on the device. Our group has first reported the successfully transferring of open-ended CNT films to copper substrates by eutectic SnPb solders at 250 ^{o}C [16]. The open-ended CNT films can be transferred to copper substrate due to the molten solders wetting along the inside and outside of the tubes through the capillary force (Figure 1.4.2 (a)). This process could overcome the serious obstacles of integration of CNTs into integrated circuits and microelectronic device packages by offering low process temperatures and improved adhesion of CNTs to the substrates. However, there are still some limitations for this transfer process. Figure 1.4.2 (b) showed that the close-ended CNT films can not be successfully transferred by using eutectic solders as transferring media. Also, the transferring process by the solders is complicated and higher cost, including paste dispensing, reflow, cleaning and polishing process, etc.

Following our idea, another two research groups also worked on the CNT transfer technology. They used silver pastes [17] and 70 nm thickness of gold layer [18] to transfer the CNT bundles or films to conductive substrates, respectively. However, the process temperatures used are 530 °C and 800 °C, respectively, which are still too high to be compatible with microelectronic processes.

Therefore, a simple, low cost and low temperature transferring process is necessary. At the same time, this process should enable the CNT films or bundles to be easily transferred to different kinds of substrates.

1.5 Research Objectives and Approaches

1.5.1 Nano lead-free solder pastes

The melting point of many materials can be dramatically reduced by decreasing their sizes. The melting and freezing behavior of finite systems have been of considerable theoretical and experimental interests for many years. As early as 1888, J.J. Thomson suggested that the freezing temperature of a finite particle depends on the physical and chemical properties of the surface. It was not until 1909, however, that an explicit expression for a size-dependent solid-liquid coexistence temperature first appeared. By considering a system consisting of small solid and liquid spheres of equal mass in equilibrium with their common vapor, it was shown that the temperature of the triple point was inversely proportion to the particle size. A similar conclusion was later reached based on the conditions for equilibrium between a solid spherical core and a thin surrounding liquid shell. Systematic experimental studies of the melting and freezing behavior of small particles began to appear in the late 1940s and early 1950s: first in a series of experiments on the freezing behavior of isolated micrometer sized metallic droplets, and later in an electron diffraction study of the melting and freezing temperatures of vapor-deposited discontinuous films consisting of nanometer-sized islands of Pb, Sn, and Bi. These studies demonstrated that small molten particles could often be dramatically undercooled, and that solid particles melted significantly below their bulk melting temperature. To date, the size dependent melting point has been found in a lot of materials both theoretically and experimentally [19-25].The high ratio of the surface area to volume of nanoparticles has been known as one of the driving forces for the size-dependent melting point depression.

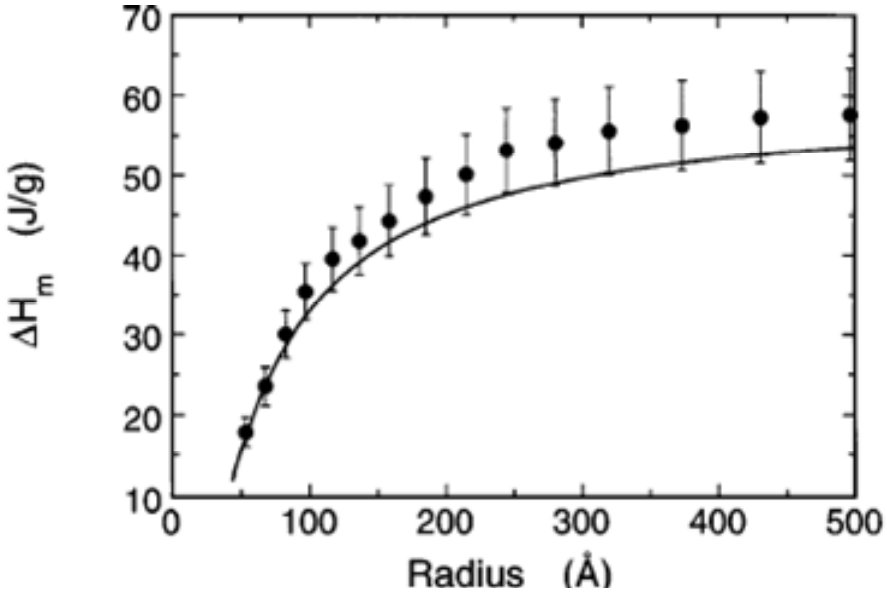

(a)

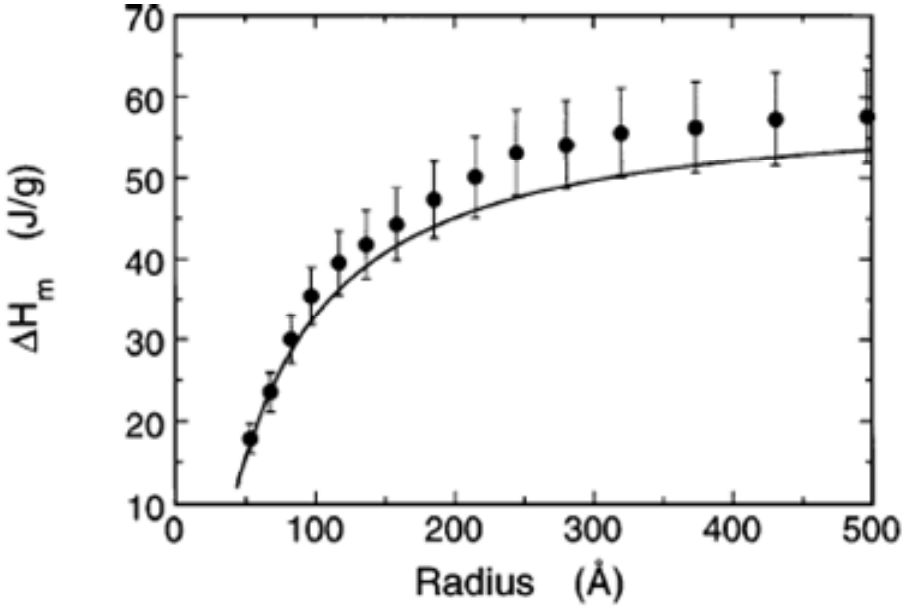

(b)

Figure 1.5.1 The size dependent melting point (a) and latent of heat of fusion (b) of Sn nanoparticles.

Lai et al studied the melting behavior of single Sn nanoparticle with a very sensitive scanning nanocalorimetric technique [19]. Their experiments successfully demonstrated

the size dependent melting point and latent heat of fusion (Figure 1.5.1), which can be explained by a solid core melting following the gradual surface melting for small particles.

Since the nano materials have lower melting point, our research objective is trying to synthesize lead-free alloy nanoparticles for low melting point interconnect applications. However, due to their low chemical potential, tin and its alloys are easily oxidized. Especially, nano sized tin alloy particles are more easily oxidized because of their higher surface area to volume ratio. Therefore, trapping each nanoparticle with surfactants is critical not only for good dispersion, but also in order to protect them from oxidation. The surfactants could cover on the particle surfaces and prevent the diffusion of oxygen to particles.

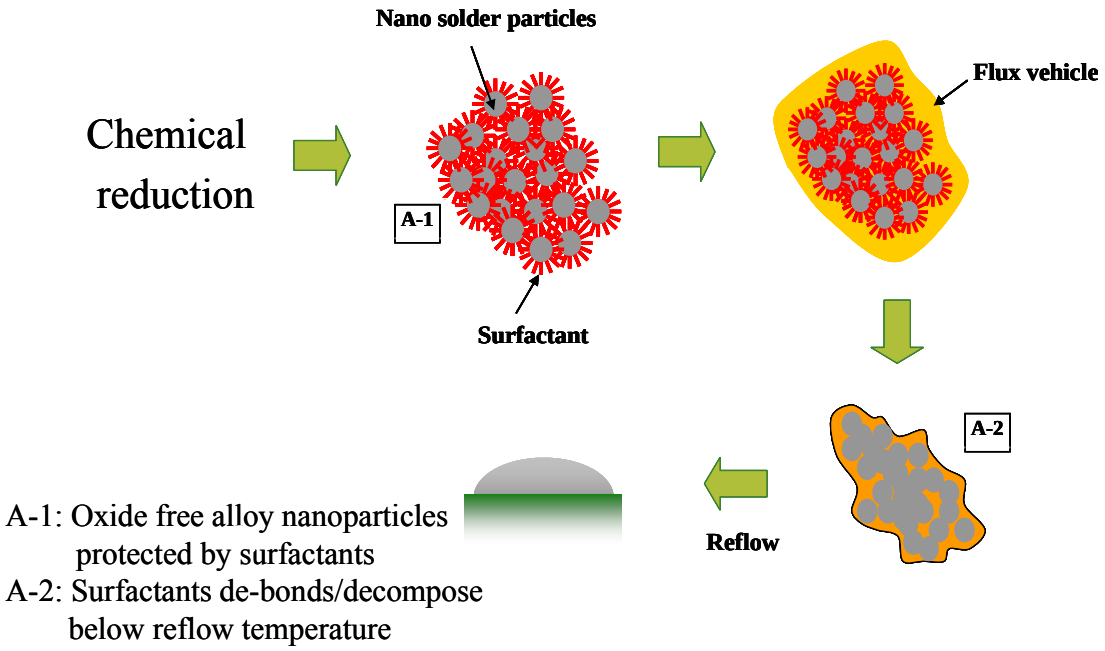

Figure 1.5.2 The schematics of nanoparticles pastes for interconnect applications.

Our procedures of using nano-sized lead-free alloy particles as low melting temperature interconnect materials are shown Figure 1.5.2. The surfactant coated Sn and its alloy nanoparticles were synthesized by the chemical reduction method. Flux and vehicles were created for the nano-sized fillers. The lead-free alloy nanoparticle pastes could wet on the copper surface to form the solder bump at a lower reflow temperature.

1.5.2 Highly conductive adhesives

The overall resistance of the isotropic conductive adhesive is the sum of the resistance of fillers, the resistance between fillers and the resistance between filler and pads (equation 1.5.1). In order to decrease the overall contact resistance, the reduction of the number of contact points between the particles may be obviously effective.

$$R_{\text{total}} = R_{\text{btw fillers}} + R_{\text{filler to bond pad}} + R_{\text{fillers}} \tag{1.5.1}$$

Although the nanocomposite takes advantage for the fine pitch application, the increased contact resistance between the nanoparticles may reduce the electrical performance of the nanocomposites. The number of contacts between the small particles is larger than that between the large particles as shown in Figures 1.5.3 (a) and (b). If nanoparticles are sintered together, the contact points between fillers will be fewer. This will lead to smaller contact resistance (Figure 1.5.3 (c)). In order to improve the electrical properties of the nanocomposite, sintering of nanoparticles in the polymer matrix during the curing process was proposed. However, there are still challenges to fabricate the nanocomposites, one of which is the dispersion of the fillers in the polymer matrix. This is due to their large surface area that increases the viscosity of the formulation

dramatically. For this reason, fabricating the high filler loading nanocomposite is difficult. Therefore, enhancement of dispersion capability of nanoparticles is of great importance. Our approach is to surface functionalize the silver nanoparticles with organic surfactants. The surfactants will help the dispersion of Ag nanoparticles in the epoxy resin. During the curing of epoxy resin (150 ^{o}C), the surfactants were debonded from the particles and at the same time the oxide layers on the particle surfaces were removed which facilitated the sintering of Ag nanoparticles.

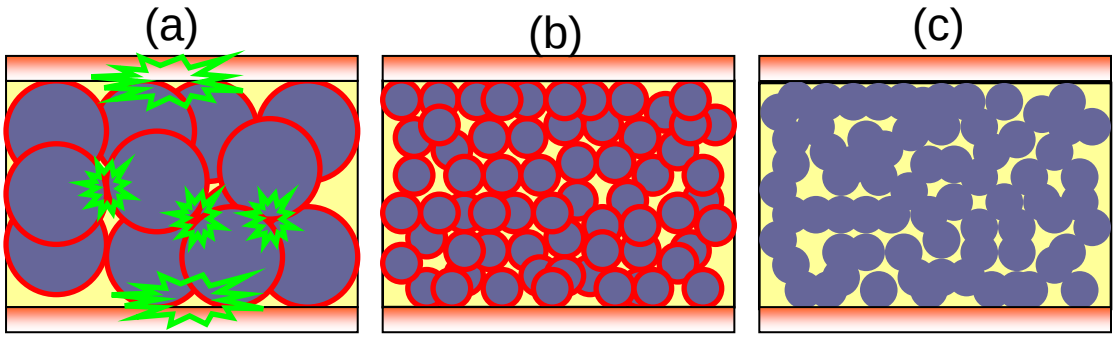

Figure 1.5.3 Schematic of particles between metal pads.

1.5.3 Adhesion enhancement of CNTs to substrates

In order to provide a simple and low cost process for transferring CNT films or bundles to different kinds of substrates, the conductive adhesives/polymer composites were proposed as the transfer media. Polymer can provide many excellent properties, such as easily wetting on many kinds of substrates, flexible design, process simple and lower cost, etc.

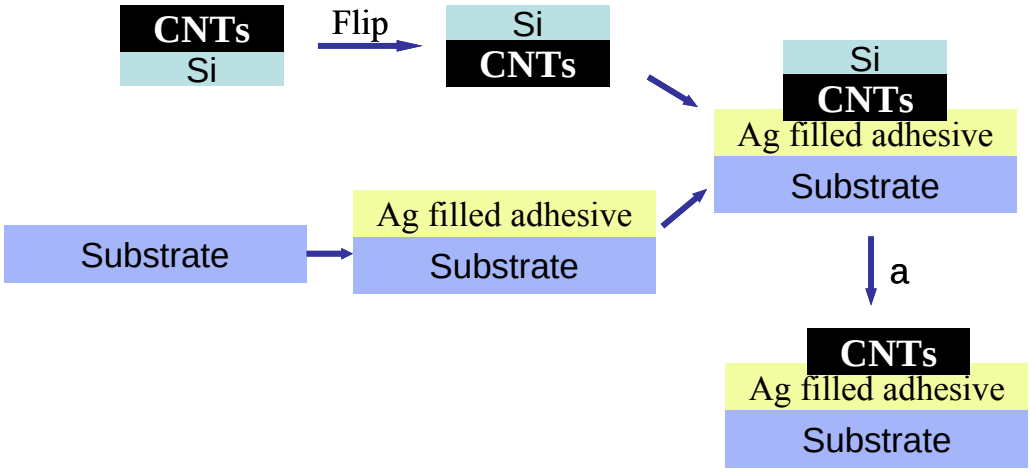

a: Cure the conductive adhesive and remove Si.

Figure 1.5.4 Schematic diagram of CNT films transferred via conductive adhesives.

Figure 1.5.4 showed the process we used to transfer CNT films to copper substrate. The conductive adhesives were stencil-printed on the copper substrate first. The silicon substrate with a CNT film was flipped over and pressed down to the adhesives with a certain pressure by hands. The conductive adhesives were cured at 150 °C for one and a half hours. Thereafter, the silicon substrate was removed. Thus, the CNT film can form the electrical and mechanical connections onto the copper surface by the conductive adhesives. This process enables CNTs to be transferred and implemented into integrated circuits and microelectronic device packages at low temperature (150 °C) and with improved adhesion of CNT films or arrays to the substrates.

1.6 Outline of This Dissertation

Chapter 1 briefly overviews the functions of electronic packaging and flip-chip technology, then introduces the current issues for the lead-free interconnect materials. The scope of this thesis is also introduced which includes the objectives and approaches

to develop low processing temperature lead-free interconnect materials. In chapter 2, the synthesis and characterization of different kinds of metal nanoparticles, such as Ag, Sn, SnIn, SnAg and SnAgCu alloy nanoparticles are described. In chapter 3, a brief introduction of solder pastes was described first, followed by the preliminary wetting studies of SnAg and SnAgCu alloy nanoparticles pastes on the cleaned copper surface. In chapter 4, ultra highly conductive isotropic conductive adhesives were prepared and a high performance nonconductive adhesives/films was formulated by dispersing a small amounts of CNTs (0.03 wt%) to increase the thermal conductivity and at the same time to decrease the coefficient of thermal expansion. Chapter 5 mainly discussed about the in-situ surface functionalization of CNTs by using trace amount of water during the chemical vapor deposition synthesis process and the transfer of CNT films to copper substrate by the conductive adhesives/polymer composites. Summary and future works are given in chapter 6.

CHAPTER II

SYNTHESIS AND CHARACTERIZATION OF SILVER, TIN AND THEIR ALLOY NANOPARTICLES

2.1 Synthesis and Characterization of Ag Nanoparticles

2.1.1 Introduction

Polymer nano composites have drawn much attention due to their unique thermal, electrical, mechanical and optical properties [26,27]. In particular, conductive nanoparticles such as silver and gold in a polymer matrix have shown a unique electrical property called Coulomb blockade [28,29], which is beneficial for electronic device applications [29]. However, the dispersion of nanoparticles into a polymer matrix has been a bottle neck for nano composite fabrication. One of the best ways to uniformly disperse nanoparticles in a polymer is the *in situ* synthesis of the nanoparticles in a polymer matrix. In the current research, the silver nanoparticles were synthesized for the nano composite applications.

Synthesis of metal nanoparticles has been going on for centuries. The silver particle was first mentioned by Vanlentinus in 1677 [27]. Many studies on silver nanoparticle synthesis have been conducted due to their unique properties in catalysis [30,31], electronics [32] and optics [33]. Usually chemical reduction methods were used to synthesize silver nanoparticles. Typical reducing agents include polyols [34,35], $NaBH_4$ [36-38], N_2H_4 [39], sodium citrate [40], and N,N-dimethyformamide [41]. The polyol process is commonly used for preparation of easily reducible metals [42]. The polyols, such as ethylene glycol, diethylene glycol or a mixture of them, can act as the reducing agents as well as solvents in which the metal salts can be dissolved [35] or suspended

[43]. In the polyol process, capping agents are used to protect nanoparticles from sintering with each other to form large particles. Poly(N-vinylpyrrolidone) (PVP) is one of the commonly used capping agents, which can passivate the surface of silver nanoparticles and prevent the possibility of silver-silver particle bond formation [42].

Some of the chemical reducing reactions can be carried out at room temperature [36,38]. But most of them need elevated temperatures for a higher reaction rate. The energy used to heat up the media can be conventional thermal heating [34,35], laser irradiation [44,45], ultrasonic [42], fixed frequency microwave radiation [43,46], UV irradiation [47] etc. Microwave radiation is known to have a faster heating rate than the conventional heating through conduction and convection. Yanagida [43], Komarneni [46] and Liu [48] have reported the use of a fixed frequency microwave (2.45 GHz) to synthesize platinum and silver nanoparticles. The microwave radiation heats up a material through its dielectric loss, which converts the radiation energy into thermal energy.

The average power dissipated (P_{av}) (W) by the material in the microwave field can be expressed as equation (2.1.1), in which ω is the applied angular frequency (Hz), E_{rms} is the electric field intensity (V/m), ε_0 is the permittivity of free space (F/m), ε''_{eff} is the effective dielectric loss factor of the material, and V is the volume of the material being heated (m^3). It can be seen from this equation that the higher the dielectric loss of a material, the higher the energy that can be absorbed. The penetration depth of a microwave is defined by equation (2.1.2), in which D_p is the depth of penetration of microwaves into the material (m), λ_0 is the wavelength of the microwaves (m), and ε' is the dielectric constant of the material. It can be seen that the penetration depth is proportional to the wavelength of applied microwave.

$$P_{av} = \omega \varepsilon_0 \varepsilon''_{eff} E^2_{rms} V \tag{2.1.1}$$

$$D_p = \frac{\lambda_0 (\varepsilon')^{1/2}}{(2\pi \varepsilon''_{eff})} \tag{2.1.2}$$

Therefore, by varying frequency (wavelength) of the applied field, a microwave can penetrate a target material with different depths. Based on this principle, variable frequency microwave (VFM) was developed to heat up the material quickly and uniformly. VFM has been used for thermoset polymers [49] curing and Sn alloys soldering [50]. These studies have shown that the VFM heating provided faster and more uniform heating profile than the conventional thermal heating methods such as convection or conduction ovens.

In this section, VFM synthesis of silver nanoparticles is discussed. It has been shown that using fixed frequency microwave radiation, fast reaction and narrow distribution of the nanoparticles can be achieved in comparison with the conventional heating methods [44,45]. Compared to the fixed frequency microwave, VFM provides more uniform heating, which can lead to a more homogenous nucleation. In addition, VFM can also heat metals without an arcing problem. The fast reaction rate of VFM method provides an important advantage for the *in situ* formation of nanoparticles in a thermosetting polymer, such as epoxy resin and polyester. In such cases, uniformly distributed nanoparticles must be formed prior to curing of the thermosetting polymers since nucleation and growth of nanoparticles could be hindered by crosslinking reaction. Therefore, a fast heating rate, uniform heating profile and precise temperature control are required. To achieve this requirement, a VFM synthetic method of siliver nanoparticles is proposed in this section. The polyol process to synthesize silver nanoparticles by VFM radiation method was used.

The reactions between a VFM method and a conventional heating method were compared. Effects of silver nitrate and PVP concentrations, reaction time and reaction temperature effect on particle size were also discussed.

2.1.2 Experimental

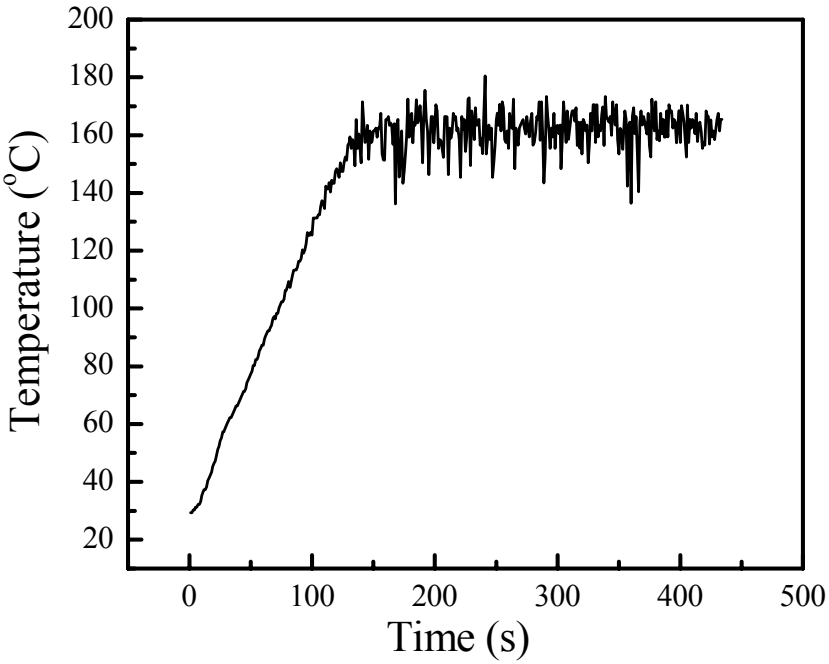

Figure 2.1.1 The heating profile of variable frequency microwave during the synthesis of nanoparticles.

First, specified amounts of silver nitrate (99+%, Aldrich) and PVP (1.0634 g, M_w = 55000, Aldrich.) were dissolved in 20 ml ethylene glycol (Fisher), respectively. The amount of PVP and silver nitrate are shown in Table 2.1.1. For microwave heating, a 3 ml silver nitrate solution and a 3 ml PVP solution were put into a 20 ml vial together and stirred at room temperature for one minute. The stirring bar was then removed and the solution was placed into the variable frequency microwave oven chamber (VFM, MicroCure 2100, Lamda Technologies Co.) to react for 1 min at 160 °C. The center frequency of the microwave, the bandwidth and the sweeping time were 6.425 GHz, 1.15

GHz and 0.1 sec., respectively. The sample temperature was monitored by a built-in thermocouple immersed in a solution. The ramping rate was set at 2 °C/sec. The applied power was controlled via a temperature feedback module. The heating profile of VFM is shown in Figure 2.1.1.

For a thermal heating reaction, a 3 ml silver nitrate solution and a 3 ml PVP solution were put into a 20 ml vial equipped with a magnetic stirring bar. Then the vial was put into a 160 °C oil bath to react for 5 min. The temperature of the solution was monitored using a thermometer. It took 3.5 to 4 min for the solution in the vial to reach the temperature of 160 °C with the above experiment conditions.

The UV-visible absorption behaviors for silver nanoparticle suspensions were recorded by using UV/vis spectrophotometer (Beckman DU 520 general purpose with 1 cm quartz). Transmission electron microscopy (TEM, Hitachi 100C TEM) was used to observe the nanoparticles synthesized. TEM samples were prepared by dispersing a few drops of silver colloid on a carbon film supported by the copper grids.

2.1.3 Results and Discussion

2.1.3.1 Comparison between VFM and conventional heating methods

Figure 2.1.2 shows a comparison of the UV-visible absorption of silver nanoparticles produced by VFM radiation and thermal heating, where the concentration of $AgNO_3$ and PVP, and the reaction temperature were the same. After the reaction, both the solutions were diluted to the same extent for the UV test (dilute to 5 times of the original). Absorbance of silver nanoparticle suspension produced by VFM radiation was much higher than that of thermal heating. Based on Beer's law, a UV-vis absorbance is directly proportional to the path length and the concentration of the suspension. From the figure,

we can conclude that the suspension by VFM has a higher concentration of Ag nanoparticles.

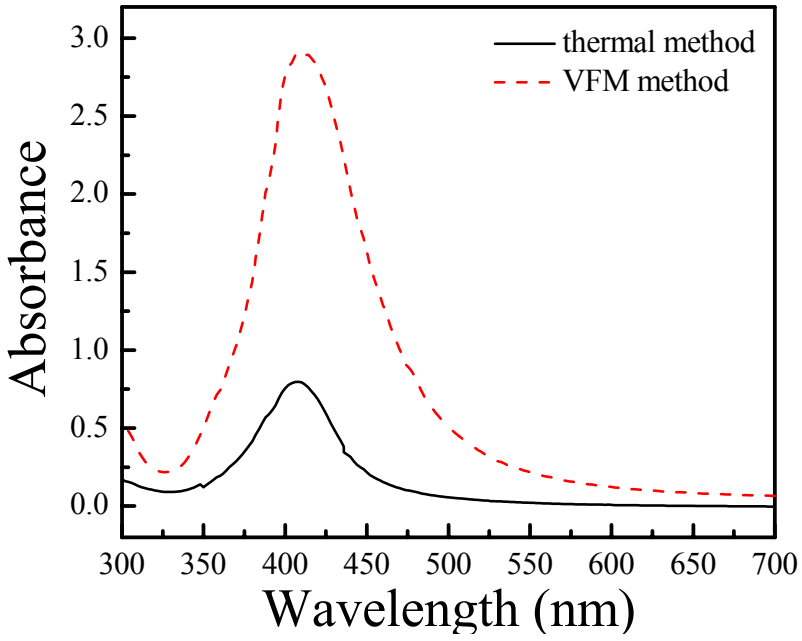

Figure 2.1.2. The UV-visible curves of silver nanoparticles produced by VFM radiation and thermal method at the same temperature of 160 °C for 5 min. The concentration of silver nitrate and PVP are the same.

Table 2.1.1 Preparation of PVP-stabilized silver nanoparticles by VFM radiation and conventional thermal heating.

No.	$AgNO_3$/PVP (g/g)	Average Diameter (nm)	Standard Deviation (nm)	Relative standard Deviation
1	0.0267/0.5317	15.51	5.59	0.36
2	0.0267/0.5317	24.40	9.62	0.39
3	0.01335/0.5317	15.44	5.29	0.34
4	0.0267/0.5317	14.42	6.68	0.46

Nos.1-3 were prepared by VFM radiation method, 1 and 3 at 160 °C; 2 at 180 °C. No. 4 was prepared by conventional heating method at 160 °C.

Table 2.1.1 summarized the results of particle size analysis for nano silver synthesized via both VFM radiation and conventional heating methods. The average diameter and relative standard deviation of particle sizes at different reaction conditions are shown in the table. The average particle size and standard deviation were counted from the particle

pictures taken in the TEM (Figure 2.1.3, 2.1.4, 2.1.5 and 2.1.6). Figures 2.1.3, 2.1.4 and 2.1.5 show the TEM images of silver nanoparticles which were synthesized by VFM radiation under different reaction conditions. It can be seen that with the increase of the concentration of silver nitrate and the reaction temperature, the average diameter of silver nanoparticles increases and the size distribution becomes broader.

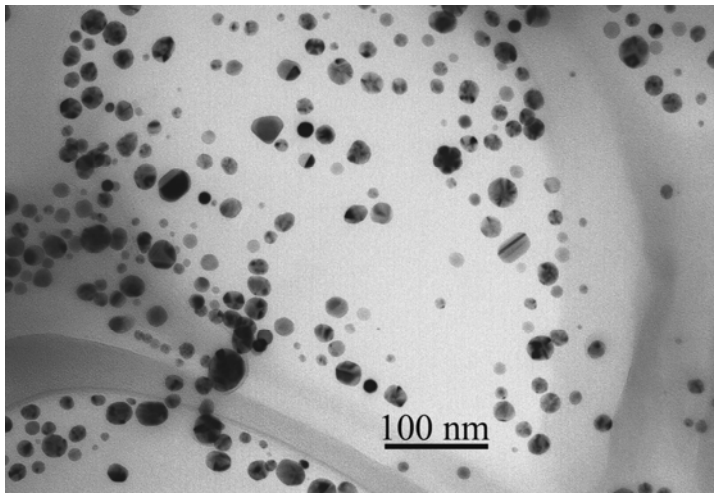

Figure 2.1.3. TEM micrographs for silver nanoparticles under the reaction of $AgNO_3$=0.0267 g in 20ml ethylene glycol, PVP=0.5317 g in 20 ml ethylene glycol at 160 °C by VFM radiation. The reaction time is 1 min.

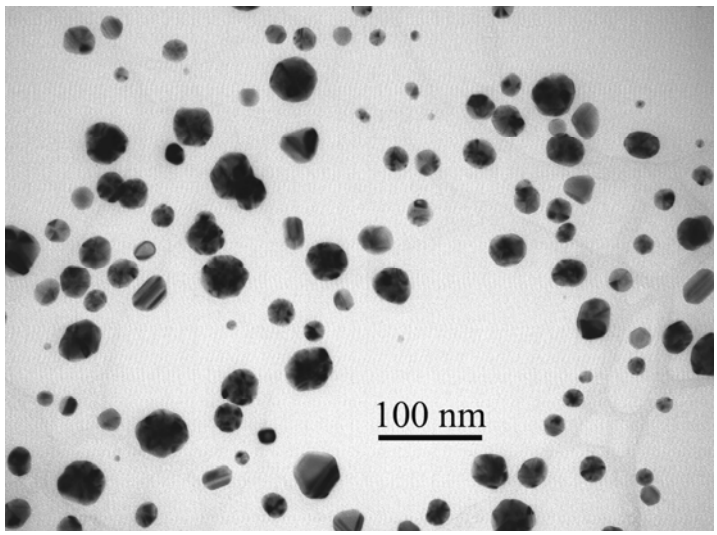

Figure 2.1.4. TEM micrographs for silver nanoparticles under the reaction of $AgNO_3$=0.0267 g in 20ml ethylene glycol, PVP=0.5317 g in 20 ml ethylene glycol at 180 °C by VFM radiation. The reaction time is 1 min.

Figure 2.1.6 shows the TEM image of silver nanoparticles which were synthesized at 160 °C for 5 min by the conventional heating method. Comparing these four pictures and the data in Table 2.1.1, it can be seen that the silver nanoparticles synthesized by VFM method have a narrow size distribution because the heating by VFM is more uniform. It has been known that keeping uniform temperature distribution and heating rate for the entire solution were two important factors to achieve narrow distribution of nanoparticles [51]. VFM can penetrate the reaction solution with different wavelength of the microwave to heat the whole solution quickly and uniformly. On the contrary, the conventional heating method heats a solution from the outside to inside slowly, due to the limited thermal conductivity of the reaction vehicle and the solution, leading to unevenness of heat conduction. From the above data and analysis, it is obvious that VFM radiation is very suitable for the preparation of narrowly dispersed nano-sized particles.

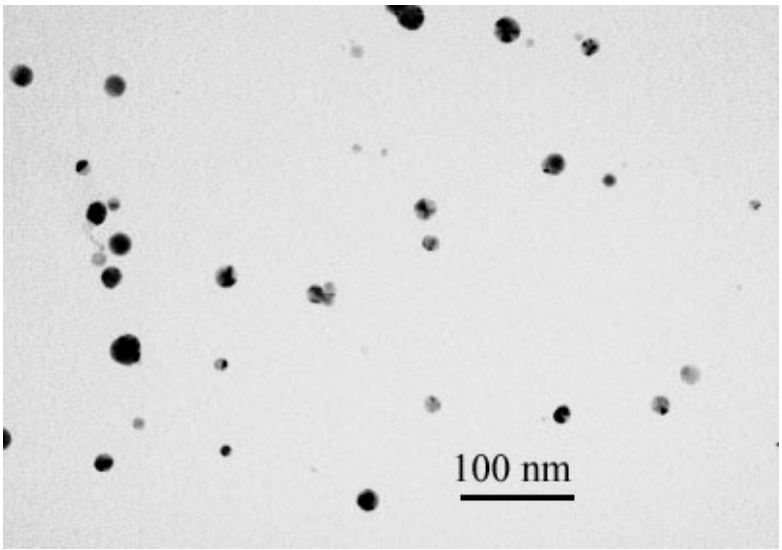

Figure 2.1.5. TEM micrographs for silver nanoparticles under the reaction of $AgNO_3$=0.01335 g in 20ml ethylene glycol, PVP=0.5317 g in 20 ml ethylene glycol at 160 °C by VFM radiation. The reaction time is 1 min.

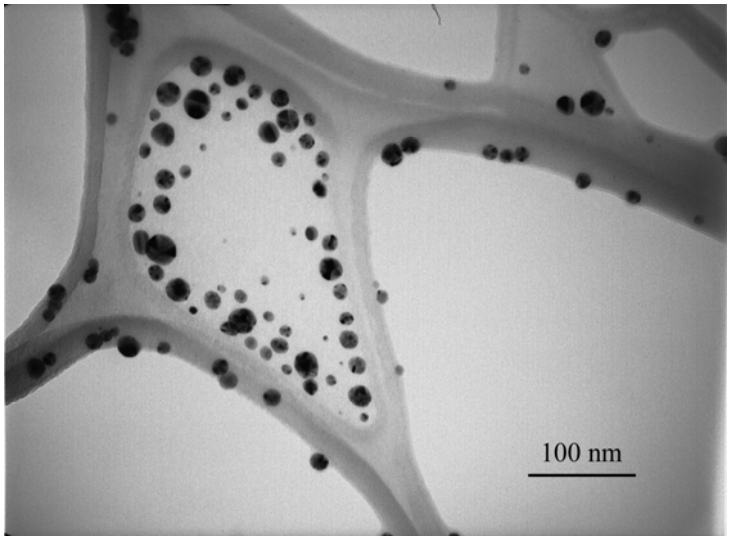

Figure 2.1.6. TEM micrographs for silver nanoparticles under the reaction of $AgNO_3$=0.0267 g in 20ml ethylene glycol, PVP=0.5317 g in 20 ml ethylene glycol at 160 °C by conventional thermal heating. The reaction time is 5 min.

Many efforts have been made to study the chemical reactions by using the microwave radiation [44,45]. It has been well known that the microwave effect on nanoparticle synthesis can be divided into thermal effect and non-thermal effect [52,53]. The thermal effect refers to the significant heating rate acceleration that can be achieved by microwave radiation. Not only the heating is faster through microwave radiation, but also the temperature distribution of the solution is more uniform. As such, this has led to the fast reaction rate and narrow size distribution of the Ag nanoparticles in the current study. The non-thermal effect relates to the inherent characteristics of microwaves other than the thermal effects. In our VFM experiment, it took about 1 min to reach the desired reaction temperature and another min at the temperature to synthesize the Ag nanoparticles. In the control experiment in an oil bath, it took about 3.5 to 4 min to reach the desired reaction temperature and another 1 to 1.5 min at this temperature to synthesize Ag nanoparticles. Comparing these two temperature profiles, we can conclude that the duration at high

temperature for the thermal method was approximately the same as, if not longer than the VFM method. However, a much higher concentration of Ag nanoparticles was observed in the VFM experiment than that of the thermal experiment with comparable average particle size. Therefore, it can be known that the microwave radiation significantly promoted the yield of the nanoparticles without interfering considerably with the particle growth process.

2.1.3.2 Effect of the concentration of $AgNO_3$ and PVP, reaction time and reaction temperature

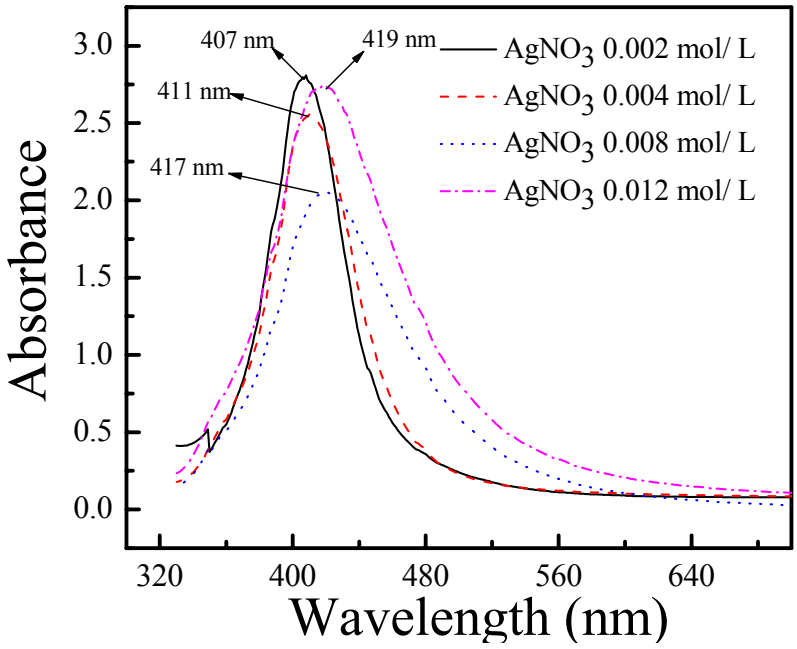

Figure 2.1.7. The UV-visible curves of silver nanoparticles produced under different concentrations of silver nitrate by VFM for 5 min at 160 °C. The concentration of PVP is the same (9.7×10^{-6} mol/L).

Figure 2.1.7 shows the UV-visible spectra of silver nanoparticles suspension produced with different concentrations of silver nitrate by the VFM radiation. It can be seen that with the increasing concentration of silver nitrate, there was a red shift in the absorption peak of the spectrum. It has long been known that the maximum absorbance peak shifts

to a longer wavelength (red shift) when the particle size becomes larger [54]. This result indicates that increasing concentrations of silver ion can promote the growth of silver nanoparticles and lead to increasing particle size. This size increase was further confirmed by the TEM results (Figures 2.1.3 and 2.1.5) and the size analysis data in Table 2.1.1. Huang *et al* [55] also found this phenomenon when they prepared stable colloidal silver nanoparticles by reduction of silver nitrate with 254 nm UV light in the presence of PVP.

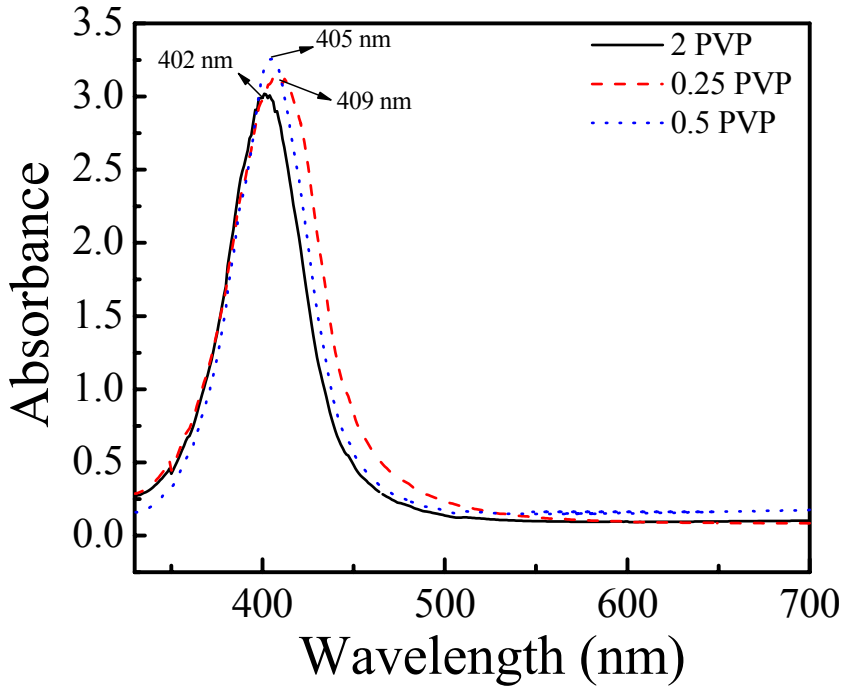

Figure 2.1.8. The UV-visible curves of silver nanoparticles produced under different concentrations of PVP by VFM for 1 min at 160 °C. The concentration of silver nitrate was the same (0.002 mol/L).

Figure 2.1.8 shows the UV-visible spectra of silver nanoparticles produced under different concentrations of PVP by VFM radiation. It can be seen that with the increase of the PVP concentration, the maximum absorbance wavelength decreased and the smaller

nanoparticles could be obtained. It was also found by Pal on his gold nanoparticle synthesis that increasing concentrations of PVP limited the particle size through the restriction of particle growth [56]. The nitrogen atoms in PVP molecules coordinate with the nanoclusters, resulting in the capping effect to limit the particle growth.

The UV-visible spectra of silver nanoparticles produced under different reaction times by VFM radiation are shown in Figure 2.1.9. With a longer reaction time, a red shift of the absorption peak on the UV-visible spectrum was observed. This was mainly due to the fact that the particles grew with time and that longer reaction time can also promote the particle aggregation to form larger particles, leading to a red shift of the absorption peak [57].

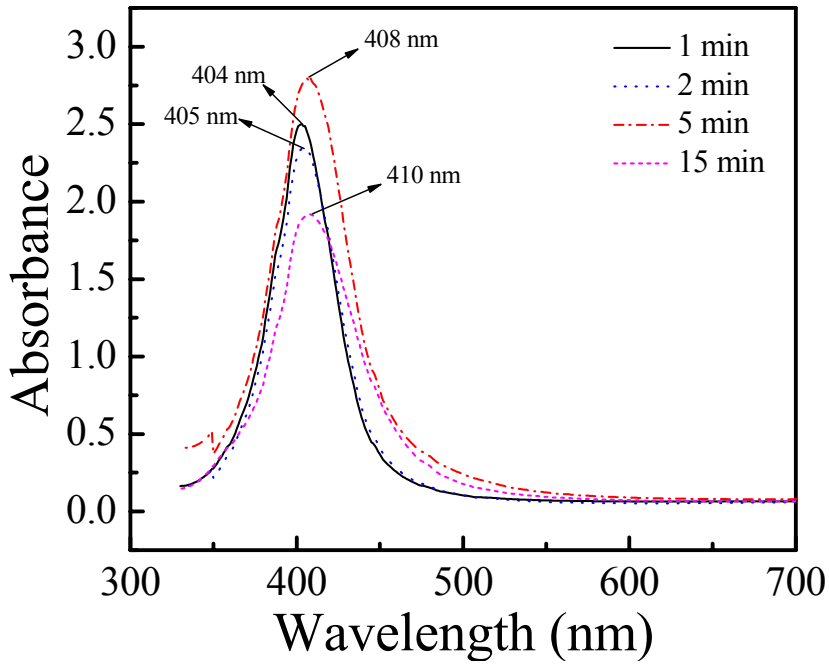

Figure 2.1.9. The UV-visible curves of silver nanoparticles produced under different reaction time by VFM at 160 °C. The concentrations of silver nitrate (0.02 mol/L) and PVP (9.7×10^{-6} mol/L) are the same. After the reaction, the solutions were not diluted to the same extent.

The UV-visible spectra of silver nanoparticles produced under different reaction temperatures by VFM radiation are shown in Figure 2.1.10. The high reaction temperature resulted in a red shift of the absorption peak, indicating that the size of silver nanoparticles increased with the increase of reaction temperature when all the other reaction conditions were identical. The result suggested that the growth of silver nanoparticles was enhanced with the increase of reaction temperature. This was also observed by Esumi when they synthesized silver nanoparticles by UV irradiation [17] (Carotenuto et al., 2000).

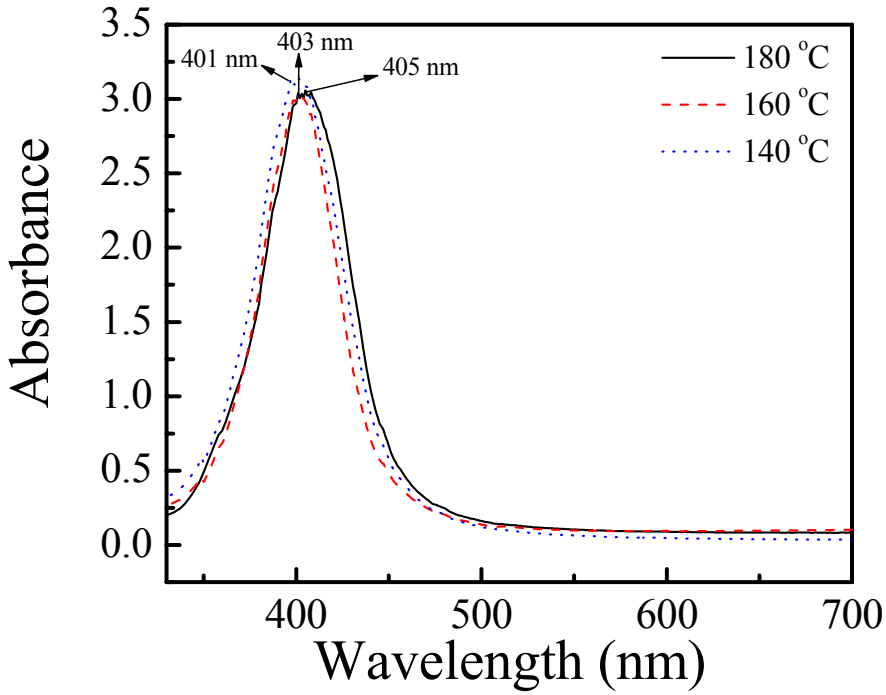

Figure 2.1.10. The UV-visible curves of silver nanoparticles produced under different reaction temperature by VFM for 1 min. The concentrations of silver nitrate (0.02 mol/L) and PVP (1.94×10^{-5} mol/L) are the same.

The above results showed that the effects of time, temperature, and concentrations of reactant and capping agent on the particle size in VFM synthesis are similar to those in the conventional synthesis using thermal heating or UV irradiation. This suggests that the

growth mechanism of the nanoparticles in VFM synthesis is not much different from that in thermal heating methods. However, the strong UV absorption of the nanoparticle suspension using VFM synthesis suggests that the microwave radiation significantly enhanced the nucleation process and therefore resulted in a high concentration of Ag nanoparticles. The mechanism is still under investigation.

2.1.4 Summary

Silver nanoparticles were synthesized by a reduction method where VFM radiation was used as a heating source. Compared to a conventional heating method, VFM provided a much faster reaction, resulting in a higher concentration of Ag nanoparticles with the same temperature exposure and duration. Other conditions, such as the concentration of silver nitrate and PVP, reaction temperature and reaction time also have effects on the size and distribution of the nanoparticles. The size of the particles increased with increasing the concentration of silver nitrate and with decreasing the concentration of PVP. Also a longer reaction time and higher reaction temperature increased the size of silver nanoparticles. These effects of reaction conditions on the size and distribution of silver nanoparticles for both VFM reaction and conventional thermal reaction were almost identical. It can be concluded that VFM heating had a strong effect on the yield of the nanoparticles while it did not interfere with the particle growth in the current experiments. By using VFM synthesis method, the higher yield and narrower distribution of Ag nanoparticles was achieved.

2.2 Synthesis and Characterization of SnIn Alloy Nanoparticles

2.2.1 Introduction

Nanoparticles show different properties from bulk materials because of their large surface area to volume ratio and quantum size effect [58]. Nowadays, materials with different properties are being demanded, especially having properties that are altogether different from those of the individual constituent materials. Bimetallic alloy nanoparticles are such a kind of materials with special properties that are different from either constituent in relation to their optical, catalytic and electronic properties [59].

Till now, two kinds of methods have been developed to synthesize bimetallic alloy nanoparticles. One is called "bottom-up" method, the most studied chemical reduction technique; the other one is the physical method called "top-down" approach. The chemical reduction method for the preparation of bimetallic nanoparticles can be divided into two groups: one is the co-reduction of two different kinds of metal precursor salts. For instance, El-Sayed [40] and Murphy [60] used simultaneous reduction of silver and gold salts to form Ag/Au alloy nanoparticles with size of 18 nm and less than 10 nm, respectively. The other one is successive reduction of two metal salts, which is usually carried out to prepare a core-shell structure of bimetallic nanoparticles. For example, seed-mediated techniques were used to synthesize core-shell type Ag/Au bimetallic nanoparticles [61]. The "top-down" approach is basically a physical method that has been developed to synthesize monometallic [62] or bimetallic nanoparticles [63]. Using this "top-down" technique, nanoparticles can be synthesized in gram quantity directly from the bulk materials without going through complex reaction procedures and without the

need of manipulative skills. But it is only suitable for the low melting point metals [62] and their alloys [63].

Recently many researches on size or shape dependent properties for nanocrystals and their synthesis methodology have been reported [64], where interesting and exotic phenomenon were observed. Therefore, a discovery for a certain structure or form that has not been seen before, can open a new area of science, research or applications. In this section, a nanobundle structure of SnIn nanoparticles is first reported, which was a collection of nanoparticles created under a certain environment. This size controllable bundle structure can be used for various types of devices such as nano/micron sized channels, etc.

In this section, a one-step gram-level synthetic procedure was used to prepare SnIn alloy nanoparticles with different shapes and sizes. The effect of the capping agent on the size of nanobundles and nanoparticles of SnIn was investigated. The possible mechanisms on the formation of different structures and sizes were discussed as well. In addition, the composition of the as-synthesized SnIn alloy nanobundles was studied by using high resolution transmission electron microscopy (HRTEM).

2.2.2 Synthesis of SnIn nanoparticles

All materials were used as received. The SnIn bulk alloys (52 % In/48 % Sn) were obtained from Indium Corporation. Poly(N-vinylpyrrolidone) (PVP, M_w = 55000) was purchased from Aldrich. Ethylene glycol purchased from Fisher Scientific was used as solvent.

In a typical experiment, 0.3 g SnIn bulk alloy and 1.0 g PVP were placed into a 250 ml flask equipped with a magnetic stirrer. Then, 60 ml ethylene glycol was added to this

flask. The solution was heated to 180 ºC and stirred for 48 hours. The suspension was cooled down to room temperature, centrifuged at 4,000 rpm for 30 min, then washed with ethanol and dried.

The shape and size of SnIn alloy nanoparticles were observed by using transmission electron microscopy (TEM, JEOL 100C). TEM samples were prepared by dispersing the particles in ethanol using an ultrasonic bath and then by placing some drops of SnIn alloy nanoparticle suspension onto a carbon film coated copper grids. HRTEM (Hitachi 2000K) was used to study the crystal structure of SnIn alloy nanobundles. The weight loss of the capping agents on the SnIn nanobundle surfaces was investigated by thermogravimetric analysis (TGA, 2050 from Thermal Advantages Inc.). A fourier-transform infrared (FTIR) spectroscope was used (Nicolet, Magna IR 560) to characterize the PVP and ethylene glycol capped on the SnIn nanobundles. The as-synthesized SnIn alloy nanobundles were mixed with dried KBr and pressed to form the semi-transparent pellets. The FTIR spectrums were collected in the wavelength range from 400 to 4000 cm^{-1}.

2.2.3 Results and Discussion

PVP was used as capping agents for the nanoparticle synthesis. It has already been found that there are direct interactions between oxygen atom of PVP and metal particles by X-ray photoelectron spectroscopic studies [65]. PVPs are adsorbed on the surface of metallic particles to prevent them from aggregation. At the same time, they can restrict the growth of nanoparticles. Therefore, it is expected that smaller size particles are formed in a more concentrated PVP solution. Similar results have already been obtained from other polymers as well [66].

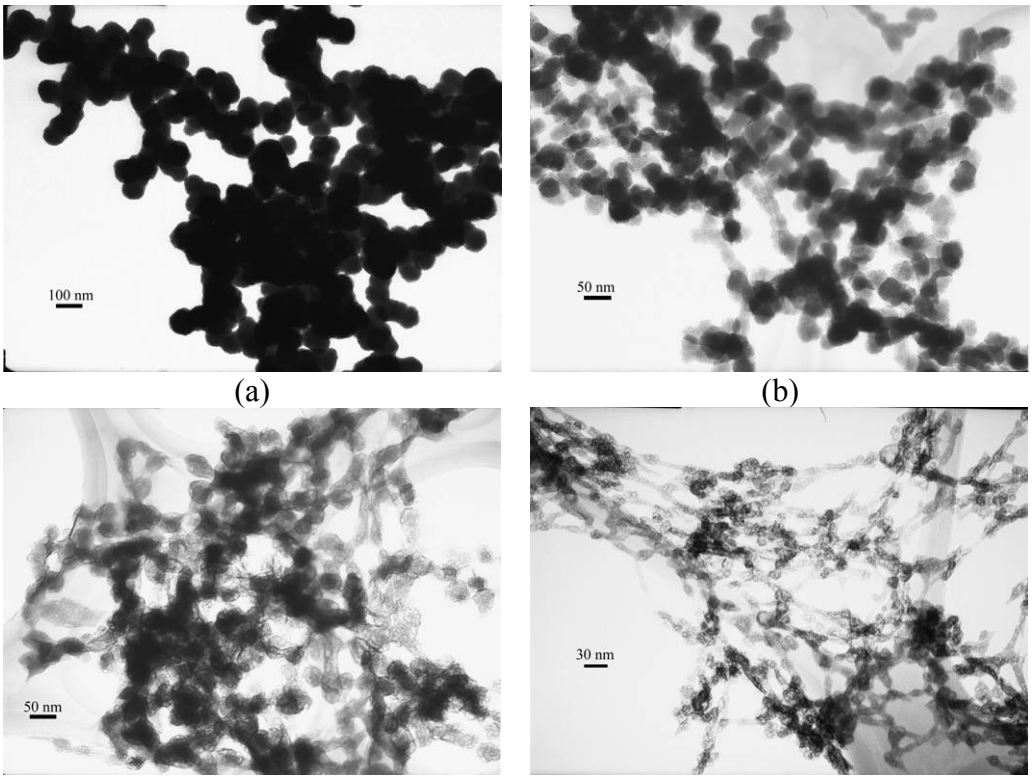

(a) (b)

(c) (d)

Figure 2.2.1. TEM images of SnIn nanoparticles which were synthesized by different concentration of PVP (M_w = 55000) in ethylene glycol: (a) 0.045 M; (b) 0.075 M; (c) 0.15 M and (d) 0.18 M.

In our study, discrete spherical SnIn alloy nanoparticles were formed when the PVP (M_w = 55000) concentration was in the range of 0.045 M to 0.18 M (Figure 2.2.1, average particle size from (a): ~70 nm, (b): ~40 nm, (c): ~30 nm to (d): ~10 nm). The concentration of PVP was varied by changing the amount of PVP, while keeping the same amount of ethylene glycol and SnIn bulk alloy. In this range, the increased concentration of PVP led to smaller sized particles. If the concentration of PVP was further increased to 0.20 M, besides spherical nanoparticles, SnIn nanobundles were also formed. With a further increase of PVP concentration (up to 0.30 M), only nanobundles were produced (Figure 2.2.2). The size of the nanobundles was getting smaller with

higher concentration of PVP, which could limit the bundle size through the restriction of bundle growth.

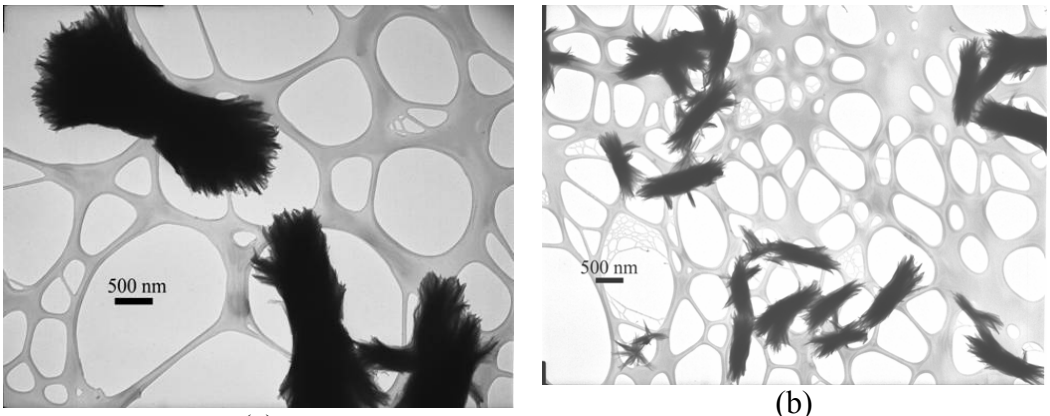

(a) (b)

Figure 2.2.2 TEM images of SnIn nanobundles which were synthesized by different concentration of PVP (M_w = 55000) in ethylene glycol: (a) 0.225 M and (b) 0.30 M.

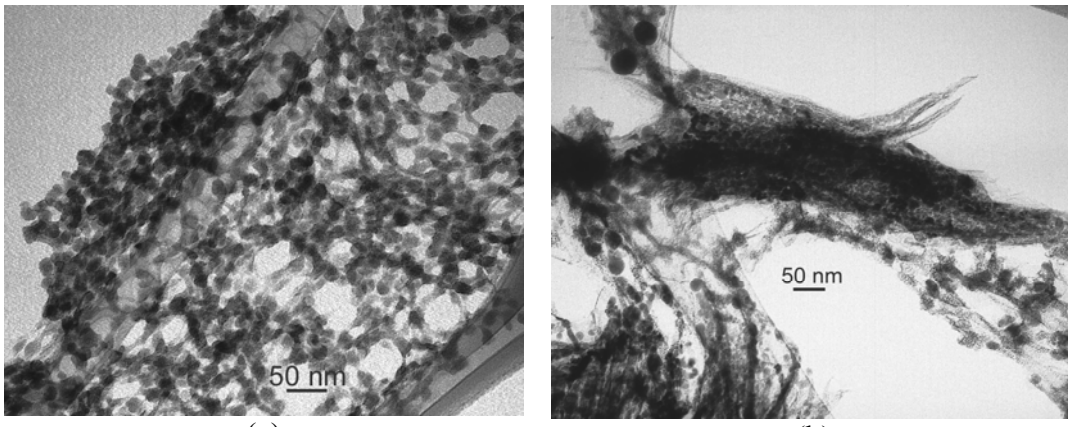

(a) (b)

Figure 2.2.3. The TEM images of SnIn nanoparticles/nanobundles prepared by 0.3 g SnIn bulk alloy in 0.225 M PVP for 24 hours (a) and 36 hours (b), respectively.

In order to study how the nanobundles were formed, the reaction in Figure 2.2.2 (a) was stopped at different intermediate stages. At 24 hours, only particles were observed in the solution (Figure 2.2.3 (a)), where the particles were connected with each other due to the existence of large amounts of polymers. At 36 hours, the nanobundles formed (Figure 2.2.3 (b)). It can be clearly seen that a large number of nanoparticles were embedded in

the nanobundles. And after 48 hrs, nanobundles with dense structure were observed (Figure 2.2.2 (a)). The particles inside the bundles interact with each other to form aggregates or collapse and then grow up due to surface energy minimization.

From the above characterization and analysis, it can be known that in the lower concentration range (less than 0.20M), PVP acts as a capping agent for the spherical particles. However, at much higher concentrations, in addition to being a capping agent, some of the PVP chains presumably connect with each other, which initialize the bundle formation. The schematics of the mechanism for the SnIn nanobundle formation we proposed are shown in figure 2.2.4.

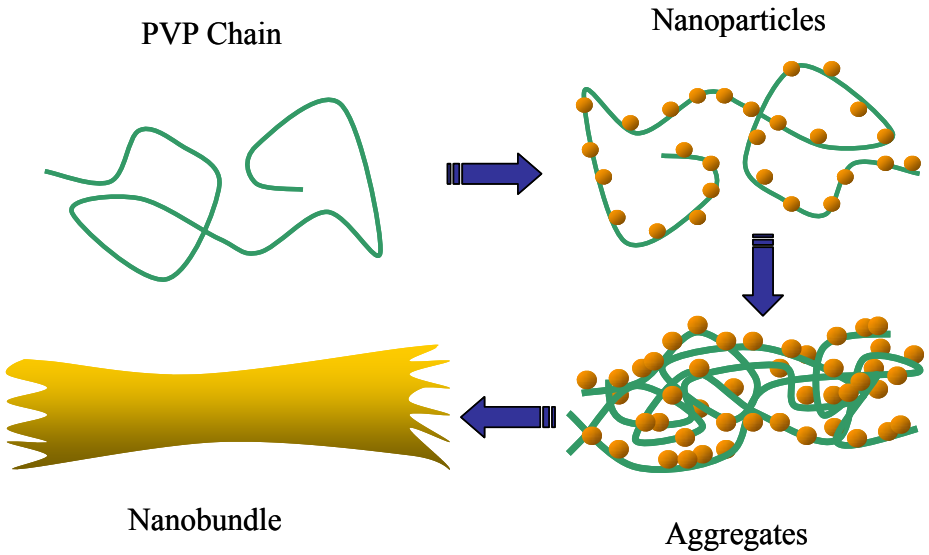

Figure 2.2.4. Schematic of the nanobundle formation mechanism.

TGA measurements were conducted in nitrogen atmosphere to study the amounts of PVP and ethylene glycol capped on the particles or bundles. Figure 2.2.5 shows the TGA results of the SnIn nanobundles in figure 2.2.2 (a). Most of the solvents inside the SnIn nanobundles were removed below 150 ºC. The PVP and ethylene glycol capped in/on the bundles gradually decomposed between 150 ºC and 450 ºC. The weight ratio of SnIn metal parts to polymer in this sample was 2.16:1. It was also found from the TGA

measurements that the metal to polymer weight ratio would decrease with the increase of the concentration of PVP used. These results clearly showed that there were large amounts of PVP and ethylene glycol capped in/on the bundles. These large amounts of polymer connect with each other which initialize the nanobundle formation.

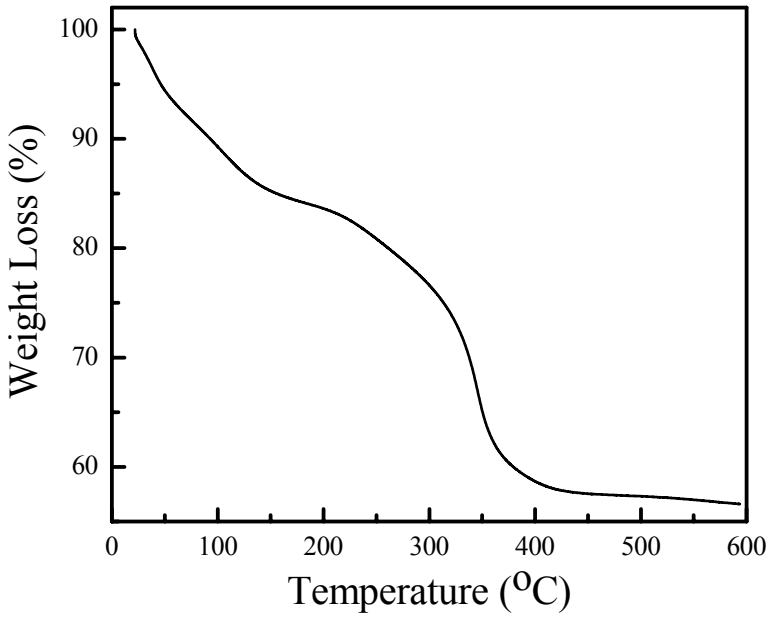

Figure 2.2.5 Thermogravimetric curves of SnIn nanobundles in figure 2.2.2 (a).

The IR spectrum of the as-synthesized SnIn nanobundles is shown in figure 2.2.6 which is compared with that of PVP and ethylene glycol, respectively. For PVP, the peak at 1679 cm^{-1} can be assigned to the C=O stretching. However, on the IR spectrum of the SnIn nanobundles, the peak of the C=O stretching was shifted to 1664 cm^{-1}. This significant ($\sim$15 cm^{-1}) blue shift is attributed to the coordination bonds formed between the SnIn particles and PVP [67]. The C=O bond would thus has less electron density as the new coordination bonds were formed, and this weakening would result in the apparent frequency shift. At the same time, it was found that the peak for the hydroxyl group bending shifted from 1654 cm^{-1} to 1614 cm^{-1} when the SnIn nanobundles were

produced, which was also due to the coordination bond formed between the SnIn bundles and the hydroxyl groups of ethylene glycol.

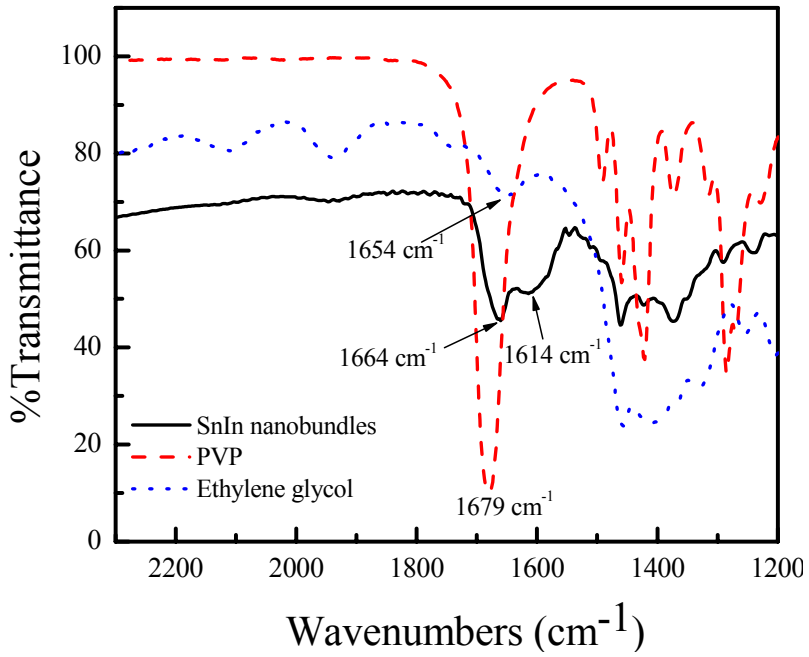

Figure 2.2.6. IR spectra of ethylene glycol, PVP and the as-synthesized SnIn nanobundles.

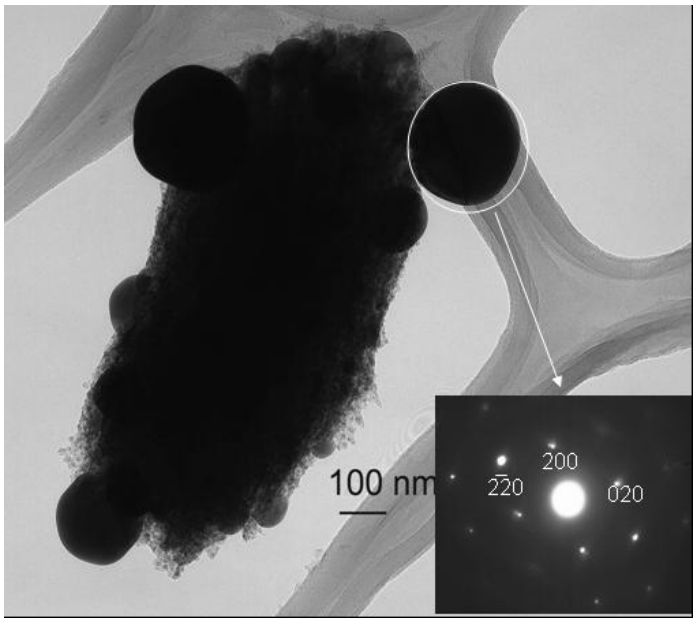

Figure 2.2.7. TEM image of SnIn nanobundles and electron diffraction pattern of the nanoparticles.

A little higher resolution TEM image of SnIn nanobundles is shown in figure 2.2.7. During the TEM examinations, it was observed that some particles came out of the nanobundles and grew into big ones. The nanoparticles inside the bundles have even lower melting point than its bulk materials (117 ºC) because of its larger surface area to volume ratio [19] and the energy from electron beam leads to the melting of nanoparticles in the bundles. The melted nanoparticles flowed out and grew into big ones. The inset of figure 2.2.7 is the electron diffraction (ED) pattern of one of the grown big particles. The spots observed in the ED pattern are readily indexed to the crystal planes of tetragonal β-In_3Sn along reflection zone axis: 001. It was also found from the energy dispersion spectrum (EDS) of HRTEM that the weight ratio of In to Sn in the nanobundles in figure 2.2.2 (a) was around 4:1. Both the results from TEM diffraction pattern and EDS show that the metal parts in the bundles in figure 2.2.2 (a) are composed of β-In_3Sn, certain amounts of indium or indium oxide.

2.2.4 Summary

Nano SnIn structures in the forms of particles and bundles were synthesized from SnIn bulk alloy at a temperature of 180 ºC in ethylene glycol medium in the presence of PVP as capping agents. It was observed that the concentration of the capping agents affected both the particle size and shape. The certain concentration of capping agents can direct the formation of the nanobundles in a particular direction through surface energy minimization. Although the fundamental basis of shape selectivity for this system has not yet been fully understood, it is believed that smaller particles can serve as the seeds in directing the transformation of small particles into aggregates to form bundles at the

elevated temperatures. TEM characterizations show that the metal parts in the bundles are composed of β-In_3Sn, certain amounts of indium or indium oxide.

2.3 Synthesis and Characterization of Sn Nanoparticles

2.3.1 Introduction

In electronic devices, tin and some of its alloys are being used as interconnect materials in on-chip and off-chip applications. Due to their high melting point (220-240 ºC), a high reflow temperature will be needed in the electronics manufacturing process. This high process temperature in electronics assembly has adverse effects not only on energy consumption, but also on substrate warpage, thermal stress and popcorn cracking in molding compounds, resulting in poor reliability of the devices. Therefore studies on lowering processing temperature of Sn are being paid attention.

The melting point of substances can be dramatically decreased when their size is reduced to nanometer size [19-25]. This is due to the high surface area to volume ratio for small particles, which as a consequence of the higher surface energy substantially affects the interior "bulk" properties of the material, resulting in a decrease of the melting point. The outer surface of the nanoparticles plays a relevant role in the melting point depression.

Till now, transmission electron microscopy (TEM) and nanocalorimeter have been used to study the melting behavior of single Sn nanoparticle or cluster. At the melting point, the diffraction pattern of the crystal structure in TEM exhibited the order-disorder transition [68]. However, unlike calorimeters, TEM can not measure the latent heat of fusion (ΔH_m), which is very useful to understand the thermodynamics of a finite material system. Lai *et al.* investigated the melting process of supported Sn clusters by

nanocalorimeter [19] and found the melting point depended nonlinearly on the inverse of the cluster radius R, which was in contrast to the traditional description of the melting behavior of small particles. They first reported a particle-size-dependent reduction of ΔH_m for Sn nanoparticles. Bachels *et al.* studied the melting behavior of isolated Sn nanoparticles or clusters by nanocalorimeter as well [20]. The melting point of the investigated Sn clusters was found to be lowered by 125 K and the latent heat of fusion per atom was reduced by 35% compared to bulk Sn. However, for both the TEM and nanocalorimetric measurements, the single element of Sn nanoparticle or the cluster was synthesized by the deposition method inside the measurement equipments in order to prevent the particles from oxidation. Although this synthesis method was sufficiently sophisticated for the pure observation, the real world synthesis and the characterization possess more experimental parameters to consider such as oxidation during moving samples and differences in melting/wetting behavior on different substrate materials.

In this section, Sn nanoparticles were synthesized by chemical reduction method. This method is more suitable for the Sn nanoparticle synthesis because the chemical reduction can use a low temperature, resulting in a better control of thermal oxidation of Sn nanoparticles. During the synthesis process, surfactants were used to protect the Sn nanoparticle from oxidation. The conventional differential scanning calorimetry (DSC) was first used to investigate the melting behavior of the as-synthesized different sized Sn nanoparticle powders. Both the size dependency of the melting point and the latent heat of fusion are presented.

2.3.2 Synthesis of Sn nanoparticles

2.3.2.1 Materials. Tin (II) acetate, sodium borohydride, and anhydrous methanol were used as precursors, reducing agents and solvents respectively. These chemicals were all purchased from Aldrich and used without further purification.

2.3.2.2 Synthesis. A certain amount of tin (II) acetate and surfactants were mixed into a 60 ml anhydrous methanol solution. The solution was stirred and nitrogen purged for 2 hours. Then, 0.1 g sodium borohydride was added to the solution and the reaction continued for another 2 hours at room temperature.

2.3.2.3 Characterization. Transmission electron microscopy (TEM, JEOL 100C TEM) was used to observe the morphologies of the synthesized nanoparticles. TEM specimens were prepared by dispersing a few drops of the Sn nanoparticle solution onto a carbon film supported by copper grids. X-ray diffraction (XRD, PW 1800) and high resolution transmission electron microscopy (HRTEM, Hitachi 2000K TEM) were used to study the crystal structure of Sn nanoparticles. A thermogravimetric analyzer (TGA, 2050 from Thermal Advantages Inc.) was used to investigate the thermal degradation of the surfactants anchoring on the Sn nanoparticle surface. The melting point of the Sn nanoparticles was determined by a differential scanning calorimeter (DSC, TA Instruments, model 2970). A sample of about 10 mg was hermetically sealed into an aluminum pan and placed in the DSC cell under nitrogen purge. Dynamic scans were made on the samples at a heating rate of 5 ºC/min, from room temperature to 250 ºC.

2.3.3 Results and Discussion

Figure 2.3.1 (a) shows the TEM and inserted HRTEM images of Sn nanoparticles synthesized by using 2.1×10^{-4} mol tin (II) acetate as a precursor in the presence of 0.045 mol surfactants. The average particle size calculated from the TEM picture was around

61 nm and the obvious lattice fringes in HRTEM image implies the crystalline structure. The interplanar spacing was about 0.29 nm which corresponds to the orientation of (200) atomic planes of the tetragonal structure of Sn. In the XRD pattern (Figure 2.3.1 (b)), all the peaks can be indexed to a tetragonal cell of Sn with a = 0.582 and c = 0.317 nm. The relative intensity of the peaks was consistent with that of the Sn nanoparticles reported elsewhere [69]. No obvious peaks at 20.6°, 33.8° and 51.8° were found, which match the crystal planes of SnO_2: (100), (101) and (211) [70]. However, the obvious oxidation peaks of SnO_2 were observed from the XRD pattern of the Sn nanoparticles without surfactants. The XRD and HRTEM results showed that the Sn nanoparticles synthesized with surfactants were nearly oxide free.

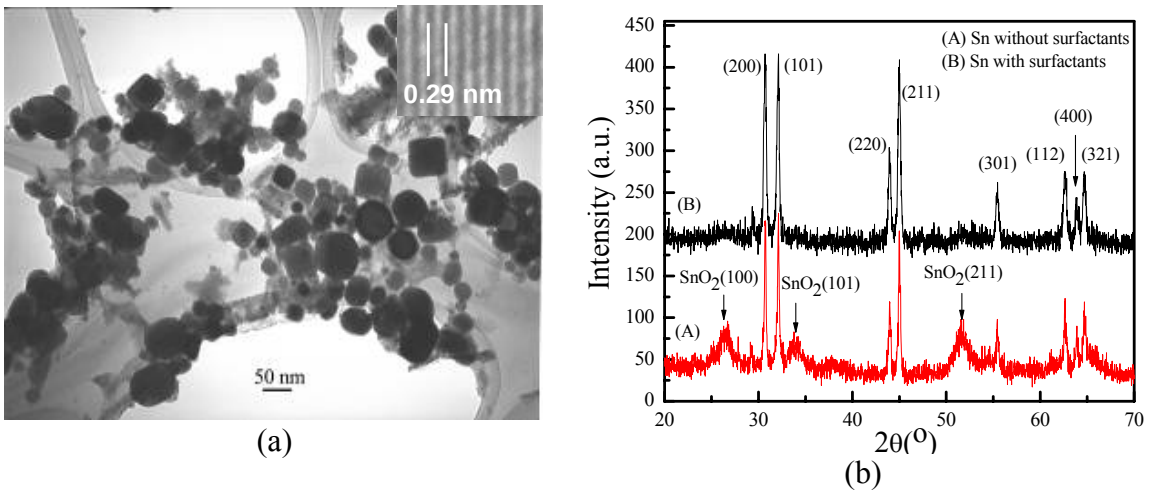

Figure 2.3.1. (a) TEM and inserted HRTEM images; (b) XRD of Sn nanoparticles which were synthesized by using 2.1×10^{-4} mol tin (II) acetate as a precursor in the presence of 0.045 mol surfactants.

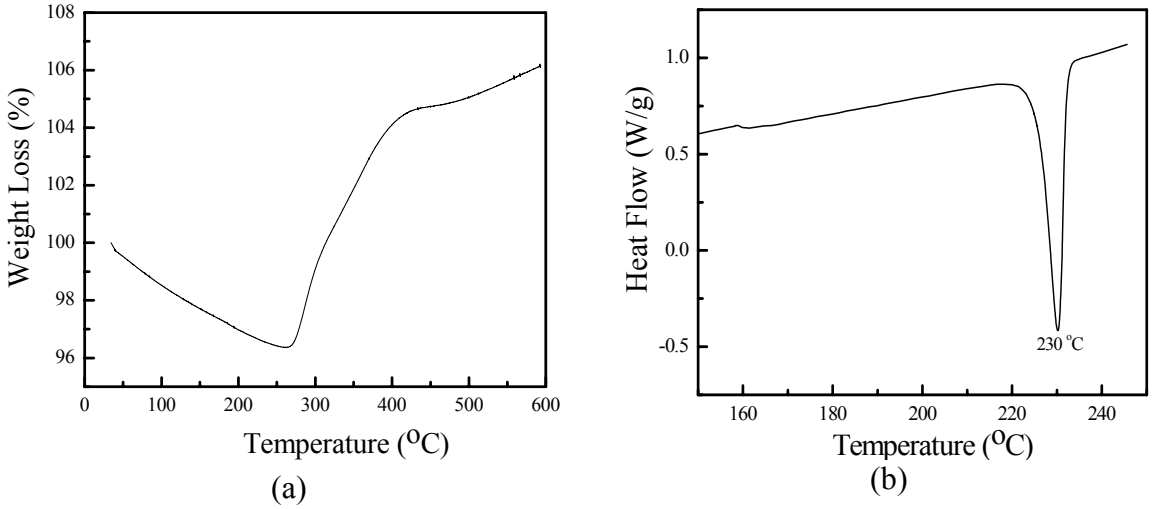

Figure 2.3.2. TGA (a) and DSC (b) curves of the as-synthesized Sn nanoparticles.

Figure 2.3.2 (a) shows the TGA curve of the as-synthesized Sn nanoparticles. The weight loss at below 275 ºC may be due to the evaporation of absorbed moisture and the decomposition of the surfactants. Above 275 ºC, the weight gain was observed. This may be attributed to thermal oxidation of the pure Sn nanoparticles. The TGA results showed that the Sn nanoparticles were covered with the surfactants by ~4 wt% to the particle weight. And these surfactants can protect the Sn nanoparticles from oxidation. Figure 2.3.2 (b) shows the thermal profiles of the as-synthesized Sn nanoparticles obtained from DSC where the melting point (T_m) was observed at 230 ºC. Compared to the T_m of micron sized Sn particles, the Sn nanoparticles exhibited the T_m depression by 2-3 ºC.

The oxide-free Sn nanoparticles were obtained by using the different molar ratios between a precursor and a surfactant. Thus, different sized Sn nanoparticles can be obtained.

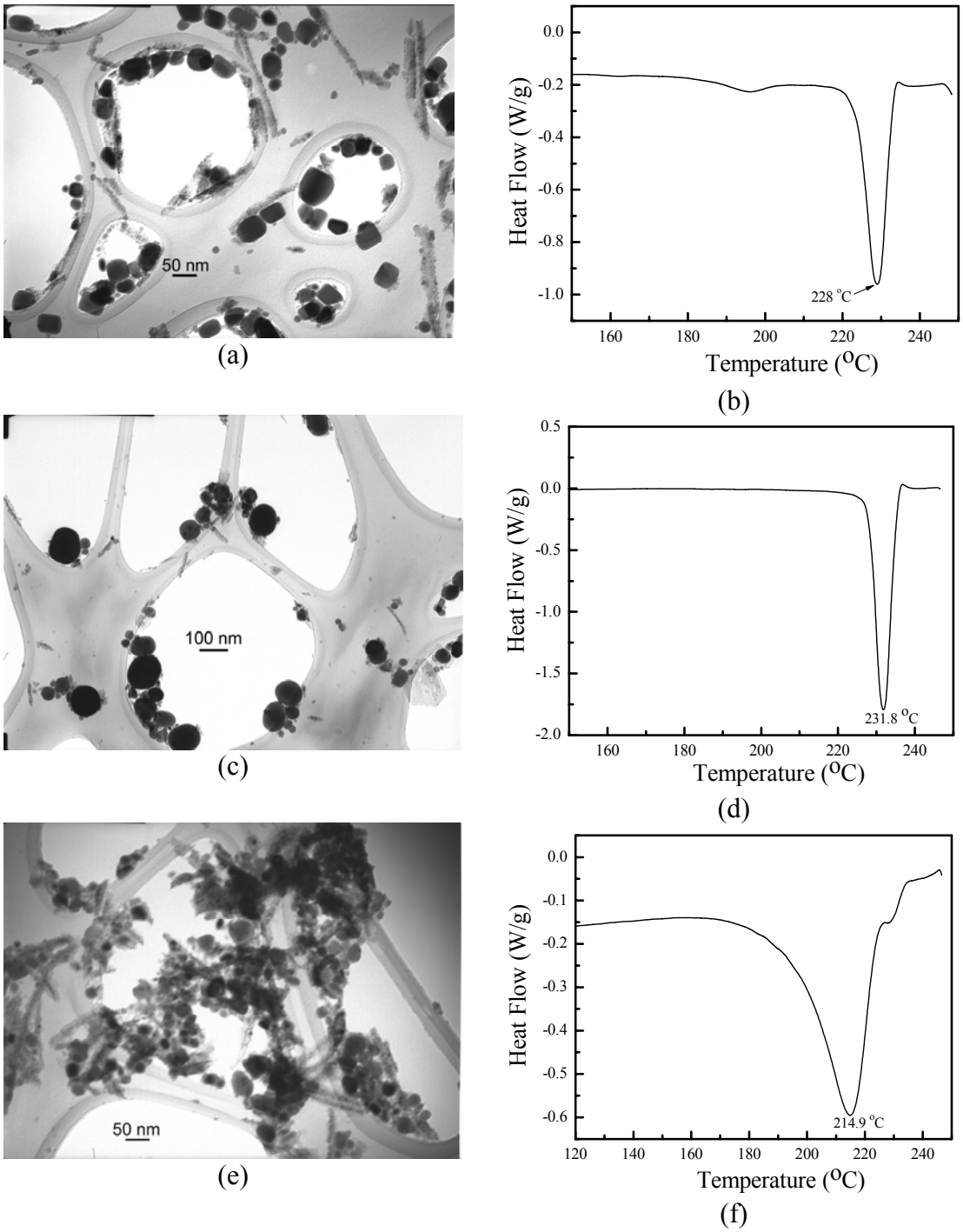

Figure 2.3.3. TEM image and thermal behavior of Sn nanoparticles which were synthesized by using 4.2×10^{-4} mol (a) and (b), 1.1×10^{-3} mol (c) and (d), 1.75×10^{-4} mol (e) and (f) tin (II) acetate as a precursor in the presence of 0.045 mol surfactants.

Figure 2.3.3 (a) and (b) show the TEM image and DSC profile of the Sn nanoparticles which were synthesized by using 4.2×10^{-4} mol tin (II) acetate as a precursor in the

presence of 0.045 mol surfactants. The average particle size was around 52 nm. The melting point of the Sn nanoparticles was around 228.0 ºC, which was 4 ºC lower than that of micron sized Sn particles. Figure 2.3.3 (c) and (d) show the TEM image and DSC profile of the Sn nanoparticles which were synthesized by using 1.1×10^{-3} mol tin (II) acetate as a precursor in the presence of 0.045 mol surfactants. The average particle size was around 85 nm. The melting point of the as-synthesized Sn nanopartiles was 231.8 ºC, which was still lower than the melting point of micron sized Sn particles. The TEM image of Sn nanoparticles which were synthesized by using 1.75×10^{-4} mol tin (II) acetate as a precursor in the presence of 0.045 mol surfactants is shown in Figure 2.3.3 (e). The average particle size was around 26 nm. The melting point of these particles was around 214.9 ºC, which was 17.7 ºC lower than that of micron sized Sn particles (Figure 2.3.3 (f)). The melting transition of this sample took place over a temperature range of about 60 ºC, which was much wider than the other three samples. This phenomenon can be attributed to a broadening of the phase transition due to the finite size effect [71] and wide size distribution of the Sn nanoparticles. Schmidt *et al.* also found a melting temperature range of 60 K for cluster size with the number of atoms between 70 and 200 [22].

From Table 2.3.1, it can be seen that the larger molar ratios between the surfactants and the precursors were used, the smaller the particle size was. This is because a larger amount of surfactants can restrict the growth of Sn nanoparticles. The surfactant molecules coordinate with the nanoclusters, resulting in the capping effect to restrict the particle growth. This was also found by Pal *et al.* on their gold nanoparticle synthesis that increasing the concentrations of surfactants would limit the particle size through the

restriction of particle growth [56]. The DSC results showed size dependent melting depression behavior and size dependent latent heat of fusion.

Table 2.3.1 Melting points and heat of fusion of different sized Sn nanoparticles

Samples	Surfactants /Precursor	Average Size (nm)	Melting point (ºC)	ΔH (J/g)
1	N/A	Micron Size	232.6	60.0
2	$0.045/1.1\times10^{-3}$	85 ± 10	231.8	32.1
3	$0.045/2.1\times10^{-4}$	61 ± 10	230.0	24.5
4	$0.045/4.2\times10^{-4}$	52 ± 8	228.0	28.7
5	$0.045/1.75\times10^{-4}$	26 ± 10	214.9	27.4

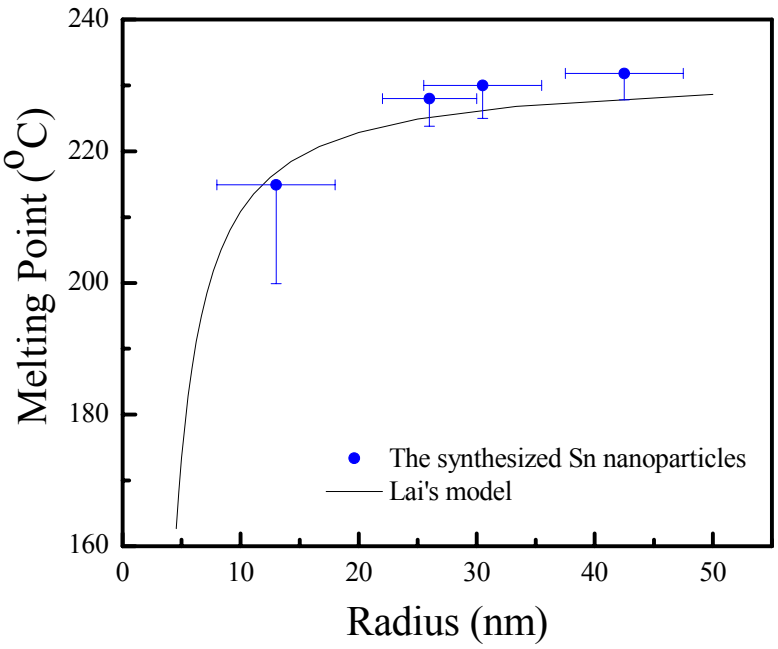

Figure 2.3.4. Size dependence of the melting points of Sn nanoparticles (Y error bars stand for the melting temperature from the onset point to the peak point of DSC curves). The solid line is calculated from equation (2.3.1) by Lai *et al* [19].

Figure 2.3.4 shows the size dependence of the melting points of the synthesized Sn nanoparticle powders, which was compared with Lai *et al.*'s model [19]. The solid line was calculated from equation (2.3.1). Lai *et al.* obtained this equation based on the model

of Hanszen [72] in which it was assumed that the solid particle was embedded in a thin liquid overlayer and the melting temperature was taken to be the temperature of equilibrium between the solid sphere core and the liquid overlayer of a given critical thickness t_0.

$$T_r = 232 - 782\left\{\frac{\sigma_{sl}}{15.8(r - t_0)} - \frac{1}{r}\right\} \qquad (2.3.1)$$

where T_r (ºC) is the melting points of particles with a radius of r (Å). t_0 (Å) is the critical thickness of the liquid layer. σ_{sl} is the interfacial surface tension between the solid and liquid, the liquid and its vapor. From their experiment, σ_{sl} is determined to be 48 ± 8 mN/m and the best fit for t_0 is 18 Å.

It is found that our experimental results are in reasonable agreement with the Lai *et al.*'s model and the melting point depends nonlinearly on the cluster radius.

From table 1, it could also be found that the latent heat of fusion of the different sized Sn nanoparticles was smaller than that of micron sized Sn powders. Ercolessi *et al.* have found that ΔH_m of gold nanoparticles decreases steadily from 114 meV/atom (bulk) to 23 meV/atom (N = 879) and 10 meV/atom (N = 477) by molecular dynamic simulation [73]. It is also found by experiments that the normalized heat of fusion of Sn nanoparticles decreases markedly from the bulk value (58.9 J/g) by as much as 70% when the particle size is reduced, which can be interpreted as a solid core melting following the gradual surface melting for small particles [19]. We tried to compare the heat of fusion (ΔH_m) of our synthesized Sn particles with Lai *et al.*'s model as well [19]. It was found that the ΔH_m values of our Sn particles were smaller than those of their models. This might be

due to the existence of the surfactants, solvents and some small amounts of oxides which might develop from the heating process of DSC test.

2.3.4 Summary

Sn nanoparticles of various sizes were successfully synthesized via chemical reduction method. Surfactants were used to prevent the synthesized Sn nanoparticles from aggregation and oxidation. The HRTEM and XRD characterizations showed that the as-synthesized Sn nanoparticles were almost at the oxide free status. DSC results showed that different sized Sn nanoparticles had different melting point depression behavior, which matched reasonably with Lai *et al.*'s model. The heat of fusion of the as-synthesized Sn nanoparticles was smaller than that of micron sized Sn powders.

2.4 Synthesis and Characterization of SnAg Alloy Nanoparticles

2.4.1 Introduction

Tin/lead (Sn/Pb) eutectic solders have long been used as an electrical interconnect material in the electronic packaging field. Lead, one of the components in the solder, has been recognized as health threat to human beings and natural environment. Due to these concerns, the investigation of an alternative to lead-free solder is imperative. Tin/silver (96.5Sn3.5Ag) is one of the promising alternatives for Sn/Pb solders [74]. However, the melting point (T_m) of 96.5Sn3.5Ag alloy is more than 30 ºC higher than that of eutectic Sn/Pb solders. The higher T_m requires the higher reflow temperature in the electronics manufacturing process, which has adverse effects not only on energy consumption, but also on the package reliability, such as substrate warpage, thermal stress and popcorn

cracking in molding compounds. Therefore, industry's attentions have been paid on lowering the processing temperature of the lead-free metals.

Duh et al has reported Sn-3.5Ag-xCu (x = 0.2, 0.5, 1.0) nanoparticles synthesis for the lead-free solder application [75], where the differential scanning calorimetry (DSC) profile showed the melting (endothermic) peak of their SnAgCu alloy nanoparticles at ~216 °C, which is the melting point of the micron meter sized SnAgCu alloy powders. No obvious melting point depression from their particles might be due to the surface oxidation or heavy agglomeration of the nanoparticles.

Transmission electron microscopy (TEM), a nanocalorimeter and DSC have been used to study the melting behavior of non noble metal nanoparticles or clusters, such as tin nanoparticles. In the TEM characterizations, at the melting point the diffraction pattern of the crystal structure exhibited order-disorder transition [68]. However, it could not measure the latent heat of fusion (ΔH_m). Therefore, the nanocalorimeter was used to investigate the melting process of Sn nanoclusters [19]. It was found that the melting point depended nonlinearly on the inverse of the cluster radius. And a particle-size-dependent reduction of ΔH_m for Sn nanoparticles was first found by the nanocalorimetric technique. However, for both the TEM and nanocalorimetric measurements, a single Sn nanoparticle or a cluster was synthesized by the deposition method inside the equipment directly in order to prevent the particles from oxidation. Although these synthesis methods were sufficiently sophisticated for the pure observation, the real world synthesis and characterization possess more experimental parameters to consider such as oxidation during moving samples. Our group has reported the synthesis of Sn nanoparticles which

were protected from oxidation by particle surface capping and their melting point depression behavior was first studied by a conventional DSC [76].

In this section, a low temperature chemical reduction method was used to synthesize different size SnAg alloy nanoparticles for lead-free solder applications. The average diameter of the particles can be achieved down to 10 nm. Surfactants/stabilizing agents were employed to prevent oxidation of the synthesized SnAg alloy nanoparticles. The microstructures of the synthesized SnAg nanoparticles were characterized by X-ray diffraction (XRD) and high resolution transmission electron microscopy (HRTEM) and the thermal behaviors of the nanoparticles were studied by the conventional DSC. In addition, the wetting test result for nano solder pastes filled with the as-synthesized 64 nm (average diameter) SnAg alloy nanoparticles was discussed.

2.4.2 Synthesis of SnAg alloy nanoparticles

2.4.2.1 Materials. Tin (II) 2-ethylhexanoate, silver nitrate, sodium borohydride, 1,10-phenanthroline [77] and anhydrous methanol were used as precursors, reducing agents, surfactants and solvents respectively. These chemicals were all purchased from Aldrich and used without further purification.

2.4.2.2 Synthesis. In a typical experiment, 7.4×10^{-4} mol tin (II) 2-ethylhexanoate, 3.0×10^{-5} mol silver nitrate (weight ratio of Sn/Ag ≈ 96.5/3.5) and 5.6×10^{-4} mol 1,10-phenanthroline [77] were mixed into a 60 ml anhydrous methanol solution. The solution was stirred and nitrogen purged for 2 hours. Thereafter, 5.0×10^{-3} mol sodium borohydride was added to the solution and the reaction continued for 1 hour at 0 °C. The as-prepared nanoparticles in solution were centrifuged at 4000 rpm for 15 mins, then

washed with methanol for three times and dried in vacuum oven for 24 hours at room temperature. After drying, the powders were stored in a nitrogen box.

2.4.2.3 Characterization. Transmission electron microscopy (TEM, JEOL 100C TEM) was used to observe the morphologies of the synthesized nanoparticles. TEM specimens were prepared by dispersing a few drops of the SnAg alloy nanoparticle solution onto a carbon film supported by copper grids. X-ray diffraction (XRD, PW 1800) and high resolution transmission electron microscopy (HRTEM, Hitachi 2000K TEM) were used to study the crystal structure of SnAg alloy nanoparticles. A thermogravimetric analyzer (TGA, 2050 from Thermal Advantages Inc.) was used to investigate the thermal degradation of the surfactants anchoring on the SnAg nanoparticle surface. The melting point of the SnAg alloy nanoparticles was determined by a differential scanning calorimeter (DSC, TA Instruments, model 2970). A sample of about 5.0 mg was hermetically sealed into an aluminum pan and placed in the DSC cell under nitrogen purge. Dynamic scans were made on the samples at a heating rate of 5 ºC/min, from room temperature to 250 ºC. Thereafter, the sample was cooled to room temperature at a cooling rate of 5 ºC/min. The cross-section of solders on a copper foil surface after reflow was studied by scanning electron microscopy (SEM) and energy dispersion spectrometry (EDS) was used to study the composition of the IMC. The SEM is a Hitachi S-800 equipped with a thermally assisted field emission gun operating at 10 KeV.

2.4.3 Results and Discussion

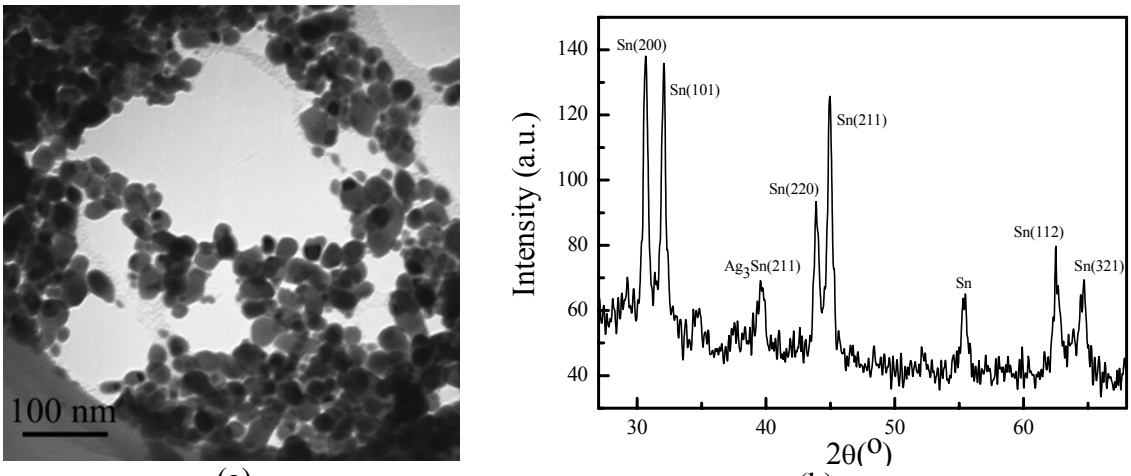

(a) (b)

Figure 2.4.1. The TEM image (a) and XRD patterns (b) of the SnAg alloy nanoparticles which were synthesized by using 7.4 $\times 10^{-4}$ mol tin (II) 2-ethylhexanoate and 3.0 $\times 10^{-5}$ mol silver nitrate as precursors in the presence of 5.6 $\times 10^{-4}$ mol surfactants.

Figure 2.4.1 (a) shows the TEM image of the SnAg alloy nanoparticles synthesized by using 7.4 $\times 10^{-4}$ mol tin (II) 2-ethylhexanoate and 3.0 $\times 10^{-5}$ mol silver nitrate as precursors in the presence of 5.6 $\times 10^{-4}$ mol surfactants at 0 °C. The average diameter of the particles was ~24.0 nm. The XRD patterns of the as-synthesized SnAg alloy nanoparticles are shown in Figure 2.4.1 (b). In addition to the peaks indexed to a tetragonal cell of Sn with a = 0.582 and c = 0.317 nm, the Ag_3Sn phase (~ 39.6°) was found in the XRD patterns, indicating the successful alloying of Sn and Ag after the reduction process [75, 78]. No prominent oxide peak was observed from the XRD patterns. This indicates that the surfactants could help to protect the synthesized SnAg alloy nanoparticles from oxidation [76,79].

Figure 2.4.2 shows the HRTEM image of the as-synthesized SnAg alloy nanoparticles, where the particles showed core-shell structures. The dark core and the brighter shell correspond to the crystalline metal and the amorphous organic surfactants respectively.

The surfactant shells on the particle surface protected the SnAg alloy nanoparticles from oxidation.

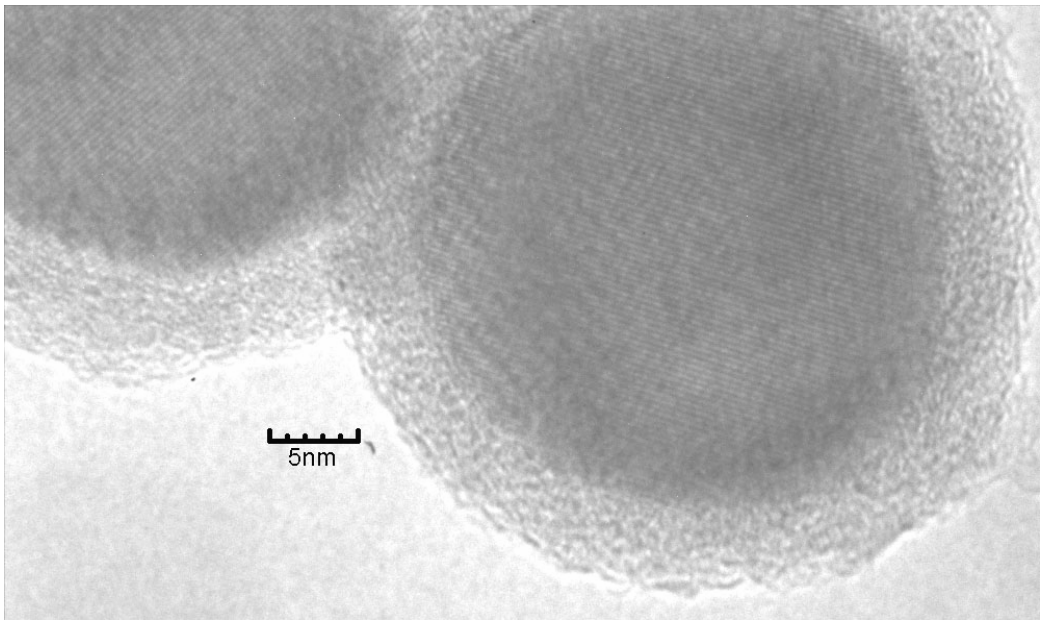

Figure 2.4.2. HRTEM image of SnAg alloy nanoparticles which were synthesized by using 7.4 $\times 10^{-4}$ mol tin (II) 2-ethylhexanoate and 3.0 $\times 10^{-5}$ mol silver nitrate as precursors in the presence of 5.6 $\times 10^{-4}$ mol surfactants.

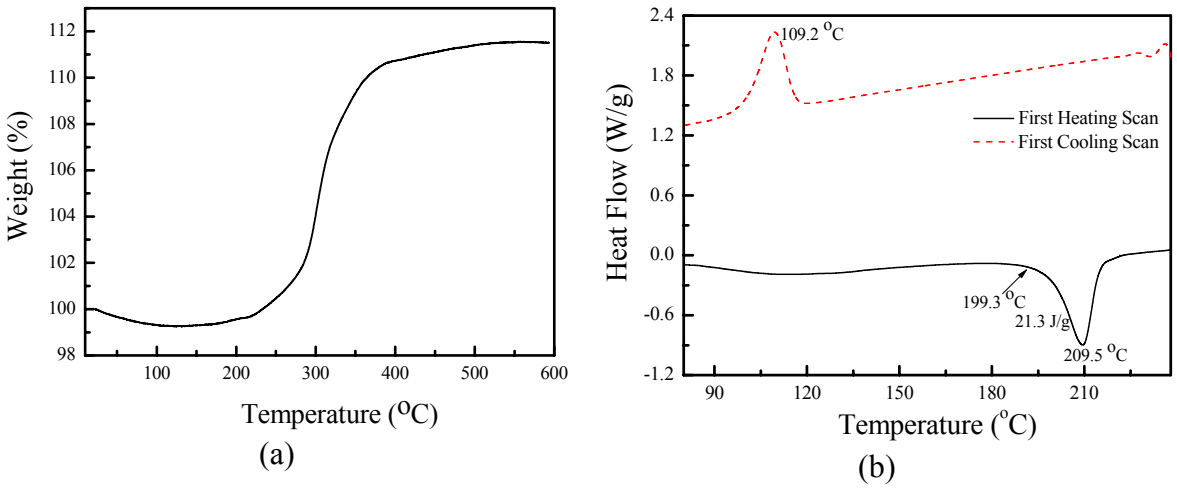

Figure 2.4.3 The TGA (a) and DSC (b) curves of the SnAg alloy nanoparticles which were synthesized by using 7.4 $\times 10^{-4}$ mol tin (II) 2-ethylhexanoate and 3.0 $\times 10^{-5}$ mol silver nitrate as precursors in the presence of 5.6 $\times 10^{-4}$ mol surfactants.

Figure 2.4.3 (a) shows the TGA curve of the dried SnAg alloy nanoparticles in nitrogen atmosphere. The weight loss at below 180 ºC might be due to the evaporation of small amount of absorbed moisture and surfactants. Above 180 ºC, the weight gain was observed, which was attributed to thermal oxidation of the SnAg alloy nanoparticles. Figure 2.4.3 (b) displays the thermal profile of the dried SnAg alloy nanoparticles. The melting point of the SnAg nanoparticles was found at ~209.5 ºC, about 13 ºC lower than that of the micron sized 96.5Sn3.5Ag particles (222.6 ºC). This was an obvious size dependent melting point depression. The latent heat of fusion (ΔH_m) of the SnAg alloy nanoparticles (24.2 J/g) was smaller than that of micron sized 96.5Sn3.5Ag powders (68.6 J/g). It has already been observed by experiments that the normalized heat of fusion of Sn nanoparticles decreases markedly from the bulk value by as much as 70% when the particle size is reduced. This can be interpreted as a solid core melting following the gradual surface melting for small particles [19]. The recrystallization peak of the as-synthesized SnAg alloy nanoparticles was found at 109.2 ºC, which was 91.2 ºC lower than that of the micron sized 96.5Sn3.5Ag particles (200.4 ºC). Such a super cooling effect in the recrystallization of the melted Sn nanoparticles has already been observed [80], which can be explained by the critical-sized stable grain that has to form for solidification to take place [81]. Solidification of the melted nanoparticles can only occur once the temperature is low enough so that the critical-size solidification grain can be accommodated in the small volume.

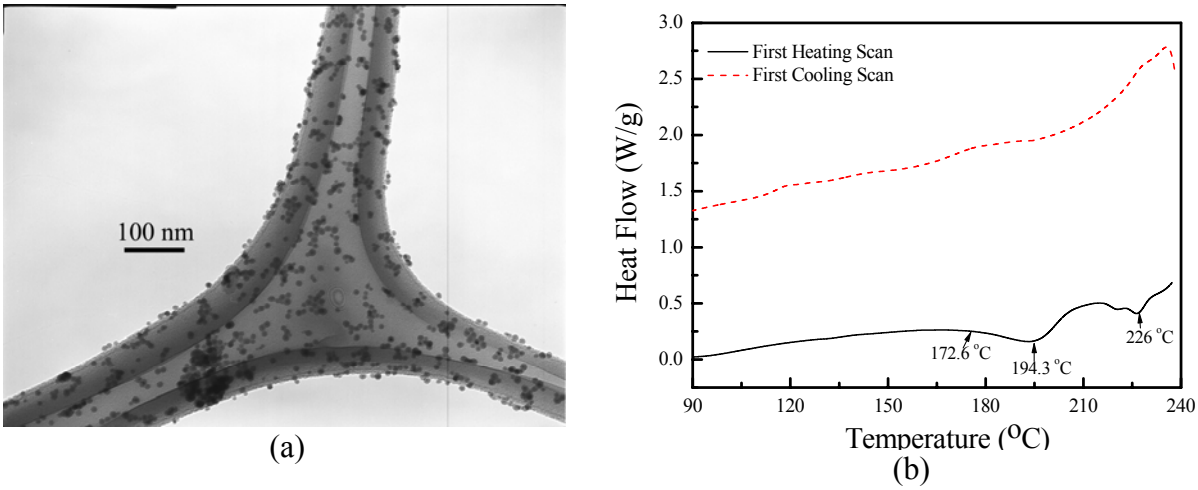

Figure 2.4.4. The TEM image (a) and DSC curves (b) of the SnAg alloy nanoparticles which were synthesized by using 7.4 $\times 10^{-4}$ mol tin (II) 2-ethylhexanoate and 3.0 $\times 10^{-5}$ mol silver nitrate as precursors in the presence of 1.1 $\times 10^{-3}$ mol surfactants.

The TEM image and the corresponding DSC curves of SnAg alloy nanoparticles which were synthesized by using 7.4 $\times 10^{-4}$ mol tin (II) 2-ethylhexanoate and 3.0 $\times 10^{-5}$ mol silver nitrate as precursors in the presence of 1.1 $\times 10^{-3}$ mol surfactants at ~ -20 °C are shown in Figure 2.4.4 (a) and (b). The average diameter of the as-synthesized nanoparticles was ~10 nm (Figure 2.4.4 (a)). From the DSC studies, the first peak melting temperature was 194.3 °C, which was about 28.3 °C lower than that of micron sized 96.5Sn3.5Ag particles (Figure 2.4.4 (b)). The onset peak temperature was 172.6 °C, which was 46.9 °C lower than that of micron sized particles (219.5 °C). The melting transition of this sample took place over a temperature range of about 21.7 ºC, much wider than the micron sized particles (3.1 °C). This phenomenon can be attributed to a broadening of the phase transition due to the finite size effect [82]. A small peak at 226.0 °C was also observed in the first heating scan, which might come from the melting of a very small amount of larger sized particles existing in this sample.

Table 2.4.1 The melting points and heat of fusion of the as-synthesized different sized SnAg alloy nanoparticles

No.	Surfactants (mol)	Reaction Temperature (°C)	Average Diameter (nm)	Melting point (°C)	ΔH_m (J/g)
1	5.6×10^{-4}	25	64	220.0	44.7
2	5.6×10^{-4}	0	24	209.5	24.2
3	8.0×10^{-4}	~ -10	17	206.0	15.1
4	1.1×10^{-3}	~ -20	10	194.3	9.95

The melting point and latent heat of fusion for micron sized 96.5Sn3.5Ag are 222.6 °C and 68.5 J/g respectively.

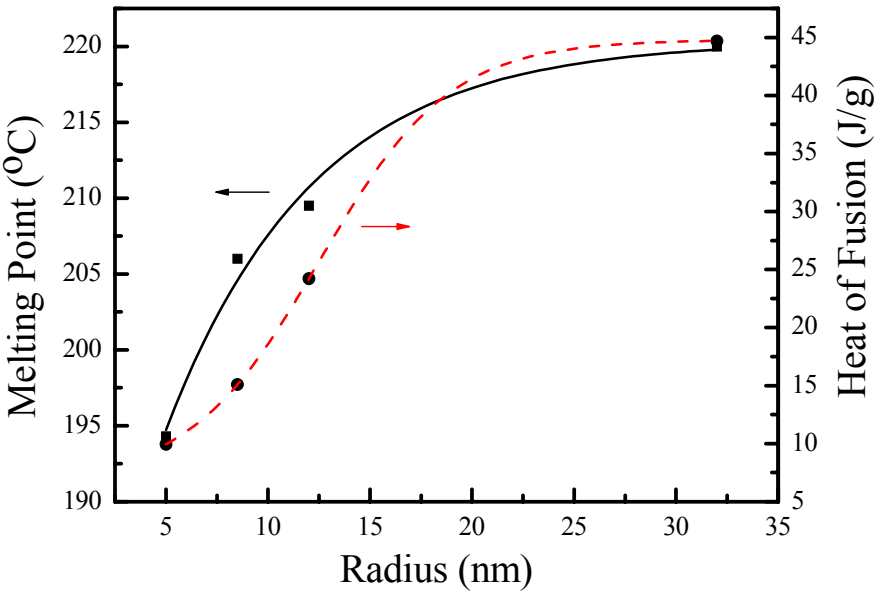

Figure 2.4.5. The relationship between the radius of the as-synthesized SnAg alloy nanoparticles and their corresponding melting points and heat of fusion respectively.

Table 2.4.1 shows the melting point and latent heat of fusion of different sized SnAg alloy nanoparticles. We plotted the melting point and ΔH_m *vs.* the corresponding particle radius in Figure 2.4.5. Both the particle size dependent melting point depression and latent heat of fusion have been observed. This is due to the surface pre-melting of nanoparticles. It has already been found that surface melting of small particles occurs in a continuous manner over a broad temperature range, whereas the homogeneous melting of the solid core occurs abruptly at the critical temperature T_m [83,84]. For smaller size metal nanoparticles, the surface melting is strongly enhanced by curvature effects.

Therefore with the decreasing of particle size, both the melting point and latent heat of fusion will decrease too. Among all the synthesized particles in table 2.4.1, the 10 nm (average diameter) SnAg alloy nanoparticles have a melting point at ~194.3 °C, which will be a good candidate for the low melting temperature lead-free solders and can solve the issues from the high temperature reflow for the micron sized lead-free particles.

2.4.4 Summary

SnAg alloy nanoparticles with various sizes were successfully synthesized for lead-free solder applications by the chemical reduction method. Surfactants were used to prevent the synthesized SnAg nanoparticles from oxidation. Both the size dependent melting point and latent heat of fusion were observed from the DSC profiles. This study demonstrated the viability of the SnAg alloy nanoparticles as a candidate for the low melting point lead-free interconnect materials.

2.5 Synthesis and Characterization of SnAgCu Alloy Nanoparticles

2.5.1 Introduction

Tin/silver/copper (96.5Sn3.0Ag0.5Cu) is one of the promising alternatives for Sn/Pb solders [85]. However, the melting point (T_m) of 96.5Sn3.0Ag0.5Cu alloy (217 ^oC) is more than 30 ºC higher than that of the eutectic Sn/Pb solder (183 ^oC) and this higher T_m requires a higher reflow temperature in the electronics manufacturing process. The high processing temperature for lead-free solders has adverse effects on not only energy consumption, but also the substrate warpage, thermal stress and popcorn cracking in molding compounds, resulting in poor reliability of the assembled devices. Therefore, studies on lowering the processing temperature of the lead-free metals are paid attention.

Our group has successfully synthesized nano sized SnAg (96.5Sn3.5Ag) binary alloy nanoparticles for low melting point lead-free solder applications [86]. The SnAg alloy nanoparticles were protected from oxidation by an organic surfactant. The surfactants could cover on the particle surface and prevent the diffusion of oxygen to the particle surfaces and therefore prevent them from oxidation. The melting point of the SnAg alloy nanoparticles could be achieved to as low as 194 ^{o}C with an average diameter of around 10 nm. The synthesized SnAg alloy nanoparticles pastes completely melted and wetted on the cleaned copper surface.

In this section, different sized 96.5Sn3.0Ag0.5Cu alloy nanoparticles were synthesized by the chemical reduction method because the SnAgCu materials are generally recognized as the first choice for lead-free solders. The small amounts of Cu could improve some of the properties of the solders, such as wetting properties, etc. Due to the easy oxidation of Sn alloy nanoparticles, surfactants/capping agents were still used to prevent the agglomeration and oxidation of the synthesized nanoparticles [76,86]. The crystal structures and compositions of the alloy nanoparticles were studied by X-ray diffraction (XRD). Differential scanning calorimetry (DSC) was used to study the melting point depression of the synthesized nanoparticles. At the same time, the fluxes for the 96.5Sn3.0Ag0.5Cu alloy nanoparticles were created. The wetting properties of the alloy nanoparticle pastes on the copper surfaces were studied as well.

2.5.2 Synthesis of SnAgCu alloy nanoparticles

Materials. Tin (II) 2-ethylhexanoate, silver nitrate, copper nitrate, sodium borohydride, and anhydrous methanol were used as precursors, reducing agents and solvents

respectively. These chemicals were all purchased from Aldrich and used without further purification.

Synthesis. In a typical experiment, 7.4×10^{-4} mol tin (II) 2-ethylhexanoate, 5.4×10^{-5} mol silver nitrate, 8.3×10^{-6} mol copper nitrate (weight ratio of Sn/Ag/Cu ≈ 96.5/3.0/0.5) and 5.6×10^{-4} mol 1,10-phenanthroline [77] were mixed into a 60 ml anhydrous methanol solution. The solution was stirred and nitrogen purged for 2 hours. Thereafter, 5.0×10^{-3} mol sodium borohydride was added to the solution and the reaction continued for 1 hour at 0 °C. The as-prepared nanoparticles in solution were centrifuged at 4000 rpm for 15 mins, then washed with methanol for three times and dried in vacuum oven for 24 hours at room temperature. After drying, the powders were stored in a nitrogen box.

Characterization. Transmission electron microscopy (TEM, JEOL 100C TEM) was used to observe the morphologies of the synthesized nanoparticles. TEM specimens were prepared by dispersing a few drops of the SnAgCu alloy nanoparticle solution onto a carbon film supported by copper grids. X-ray diffraction (XRD, PW 1800) was used to study the crystal structure of SnAgCu alloy nanoparticles. A thermogravimetric analyzer (TGA, 2050 from Thermal Advantages Inc.) was used to investigate the thermal degradation of the surfactants anchoring on the SnAgCu nanoparticle surface. The melting point of the SnAgCu alloy nanoparticles was determined by a differential scanning calorimeter (DSC, TA Instruments, model 2970). A sample of about 5.0 mg was hermetically sealed into an aluminum pan and placed in the DSC cell under nitrogen purge. Dynamic scans were made on the samples at a heating rate of 5 ºC/min, from room temperature to 250 ºC. Thereafter, the sample was cooled to room temperature at a cooling rate of 5 ºC/min. The cross-section of solders on a copper foil surface after reflow

was studied by scanning electron microscopy (SEM) and energy dispersion spectrometry (EDS) was used to study the composition of the IMC. The SEM is a Hitachi S-800 equipped with a thermally assisted field emission gun operating at 10 KeV.

2.5.3 Results and Discussion

SnAgCu alloy nanoparticles were synthesized by the chemical reduction method. Figure 2.5.1 shows the TEM image of the as-synthesized SnAgCu alloy nanoparticles. It can be calculated that the average diameter of the particles is around 20 nm.

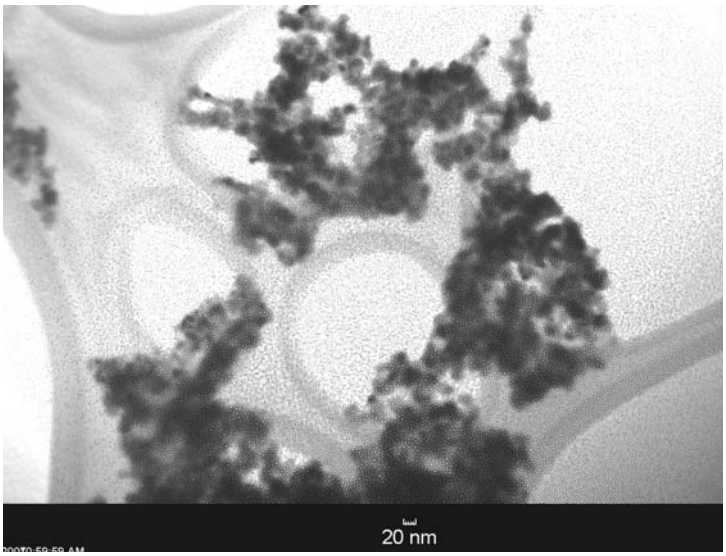

Figure 2.5.1. TEM image of SnAgCu alloy nanoparticles.

The XRD patterns of the as-synthesized SnAgCu alloy nanoparticles are shown in Figure 2.5.2. In addition to the peaks indexed to a tetragonal cell of Sn with a = 0.582 and c = 0.317 nm, the Ag_3Sn phase (39.6°) was found in the XRD patterns, indicating the successful alloying of Sn and Ag after the reduction process [75,78,86]. At the same time, Cu_6Sn_5 was formed which was due to the alloying of Sn and Cu [75]. No prominent

oxide peak was observed from the XRD patterns. This indicates that the surfactants could help to protect the synthesized SnAgCu alloy nanoparticles from oxidation [76,86]. Our HRTEM characterizations already showed that the surfactants covered on the particle surfaces and formed a core-shell structure. The core came from the crystalline metal particles and the shell might come from the amorphous surfactants. The amorphous surfactant shells on the particle surface could prevent the SnAgCu alloy nanoparticles from oxidation [86].

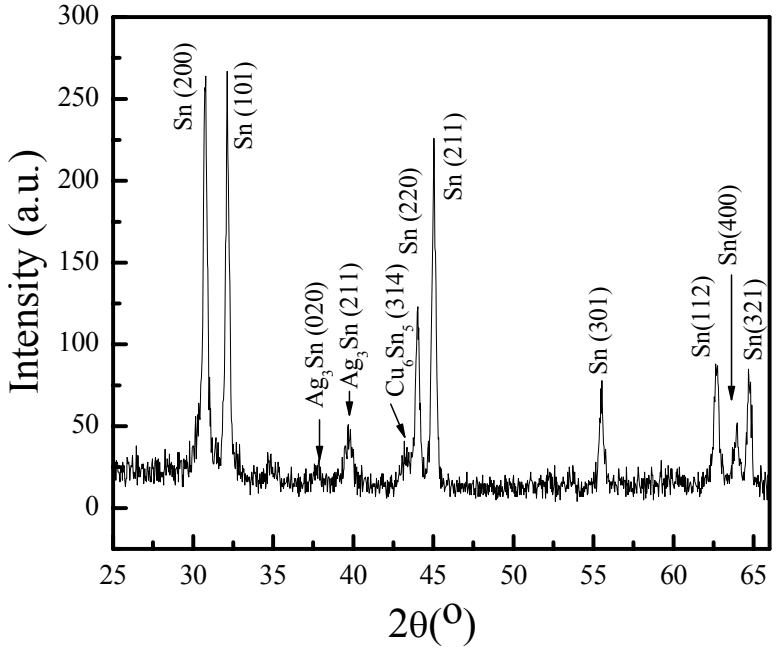

Figure 2.5.2 The XRD patterns of SnAgCu alloy nanoparticles.

Figure 2.5.3 shows the TGA curve of the as-synthesized dried SnAgCu alloy nanoparticles in nitrogen atmosphere. The weight loss below 180 °C might be due to the evaporation or decomposition of a small amount of absorbed moisture and surfactants.

Above 180 °C, the weight gain was observed, which was attributed to thermal oxidation of the SnAgCu alloy nanoparticles.

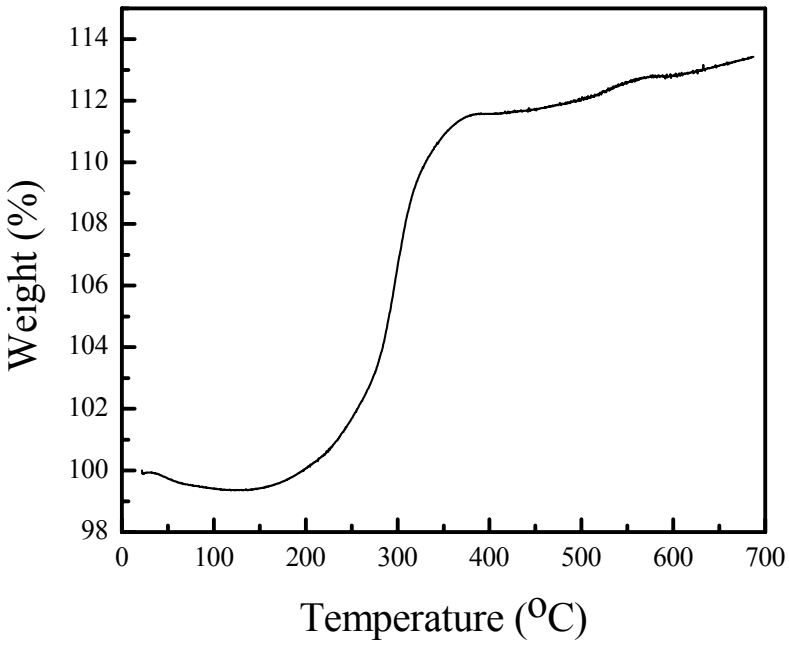

Figure 2.5.3. The TGA curve of SnAgCu alloy nanoparticles.

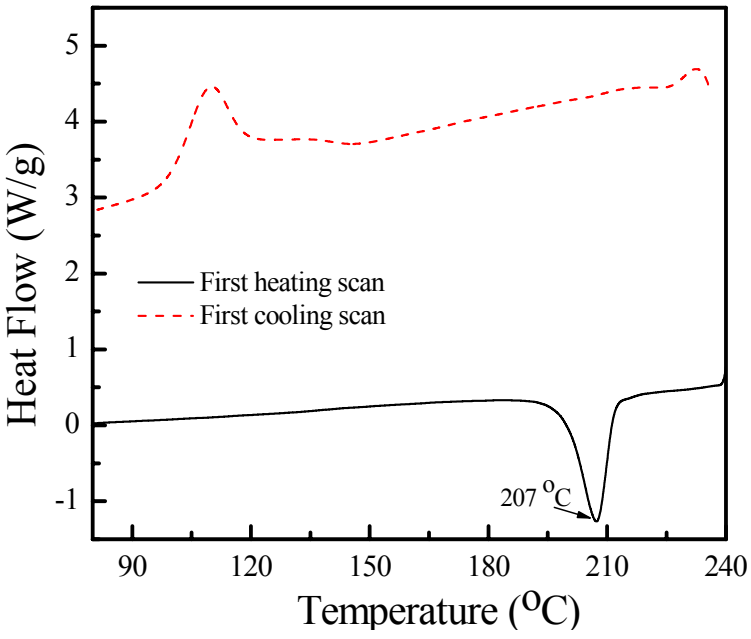

Figure 2.5.4. The DSC curves of SnAgCu alloy nanoparticles.

The thermal properties of the as-synthesized SnAgCu alloy nanoparticles were studied by a differential scanning calorimeter (Figure 2.5.4). In the first heating scan of the DSC curve, an endothermic peak point at around 207 °C was obtained, which is around 10-12 °C lower than the melting point of micron sized SnAgCu (217 ~ 219 °C) alloy particles. This is an obvious melting point depression. In the first cooling scan, the super cooling of the nanoparticles with a crystallization peak is at 113.3 °C was observed, much lower than that of micron sized SnAgCu alloy nanoparticles. Such a supercooling effect in the recrystallization of the melted Sn and SnAg alloy nanoparticles has already been observed [80], which can be explained by the critical-sized stable grain that has to form for solidification to take place [81]. Solidification of the melted nanoparticles can only occur once the temperature is low enough so that the critical-size solidification grain can be accommodated in the small volume.

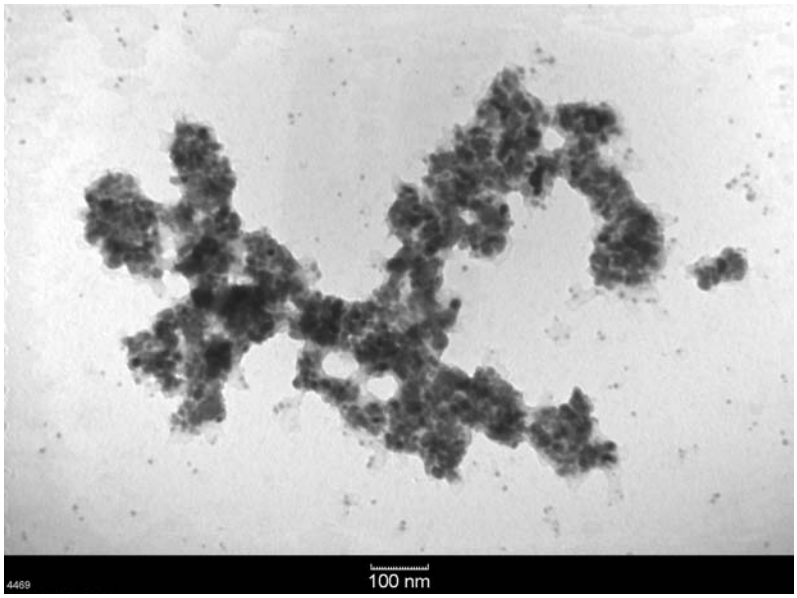

(a)

Figure 2.5.5. The TEM images of a different sized SnAgCu alloy nanoparticles (a) and its corresponding DSC curves (b).

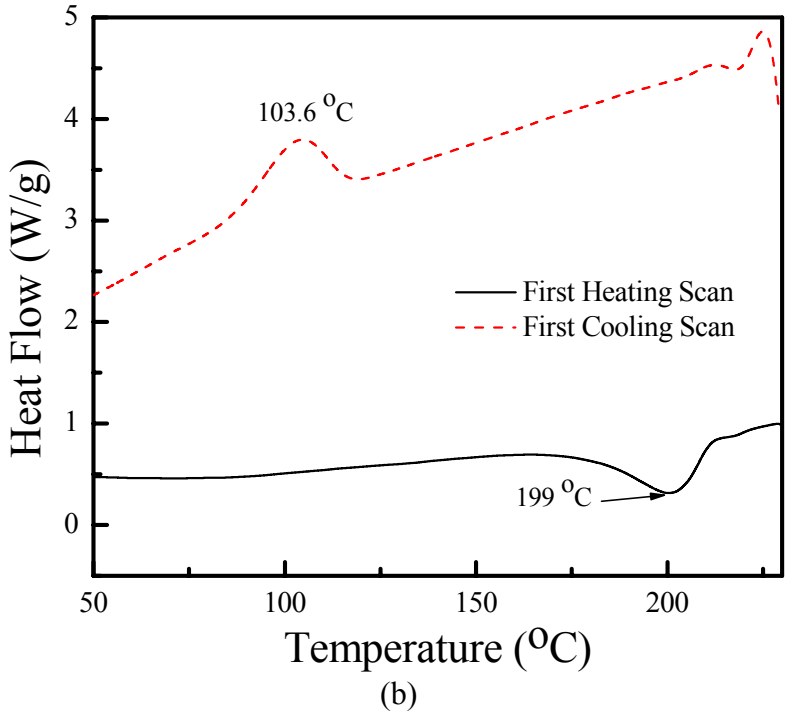

(b)

Figure 2.5.5 continued.

Figure 2.5.5 (a) shows the TEM image of a different sized SnAgCu alloy nanoparticles which were synthesized by chemical reduction method at a different reaction temperature. The average diameter of the particles is around 10-15 nm. From DSC studies (Figure 2.5.5 (b)), the peak melting temperature was 199 °C, which was around 20 °C lower than micron sized 96.5Sn3.0Ag0.5Cu particles. The onset peak temperature is 177 °C, a 37.5 °C lower than micron sized particles (214.5 °C). The melting transition of this sample took place over a temperature range of about 22 ºC. This phenomenon can be attributed to a broadening of the phase transition due to the finite size effect [82].

Table 2.5.1. the melting and recrysatllization points, heat of fusion of different sized SnAgCu alloy nanoparticles

Size	Melting point (°C)	ΔH (J/g)	Recrystallization (°C)
Micron	217	72.2	145
Nano1	210.4	42.7	112.3
~ 20 nm	207.3	31.0	109.9
Nano3	206.1	24.7	108.7
~ 10-15 nm	199	15.9	103.6

Table 2.5.1 shows the melting point, latent heat of fusion and recrystallization temperature of different sized SnAgCu alloy nanoparticles. Both the size dependent melting point depression and latent heat of fusion have been observed. These are due to the surface pre-melting of nanoparticles. It has already been found that surface melting of small particles occurs in a continuous manner over a broad temperature range, whereas the homogeneous melting of the solid core occurs abruptly at the critical temperature T_m [84]. For smaller size metal nanoparticles, the surface melting is strongly enhanced by curvature effects. Therefore, with the decreasing of particle size, both the melting point and latent heat of fusion will decrease too. Among all the synthesized particles in Table I, the 10-15 nm (average diameter) SnAgCu alloy nanoparticles have a low melting point at ~199 °C, which will be a good candidate for the lead-free solders as it can solve the issues from the high temperature reflow for the micron sized lead-free alloy particles.

SnAgCu alloy nanoparticles without any surfactants were also synthesized and their thermal properties were studied by DSC in nitrogen atmosphere too. In the first heating and cooling scan of DSC curves (Figure 2.5.6), no obvious melting and re-crystallization peaks were observed, which was due to the fully oxidation of the SnAgCu alloy nanoparticles. No surfactants were coated on the particle surfaces to prevent them from oxidation.

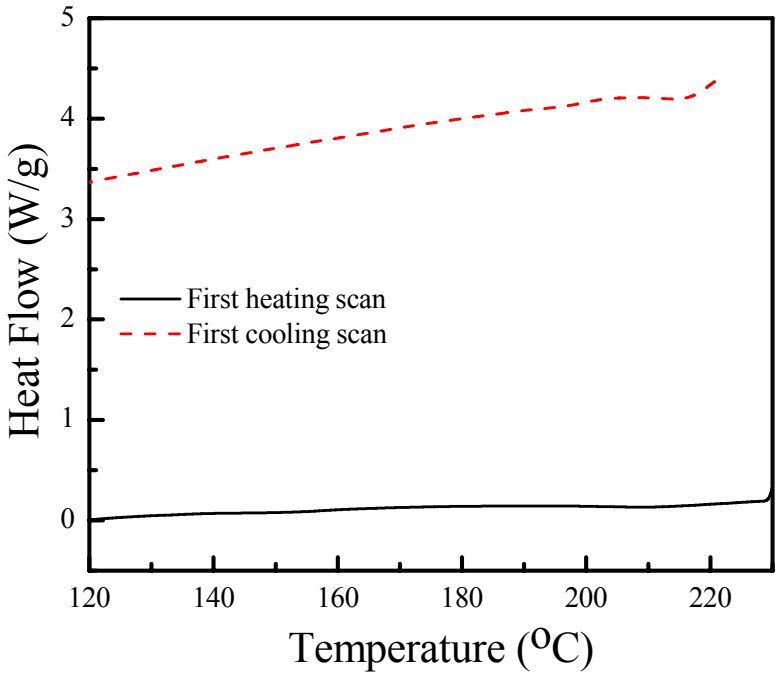

Figure 2.5.6. The DSC curves of SnAgCu alloy nanoparticles without surfactants.

2.5.4 Summary

SnAgCu alloy nanoparticles with various sizes were successfully synthesized for lead-free solder applications by the chemical reduction method. Surfactants were used to prevent the synthesized SnAgCu nanoparticles from aggregation and oxidation. Both the size dependent melting point and latent heat of fusion were observed from the DSC tests. This study also demonstrated the feasibility of the SnAgCu alloy nanoparticles as a candidate for the low melting point lead-free interconnect materials.

CHAPTER III

WETTING PROPERTIES OF NANO SOLDER PASTES

3.1 Solder Pastes

Solder paste is a viable interconnecting material, providing electrical, thermal and mechanical properties applicable to electronics assemblies. It is a homogeneous and kinetically stable mixture of solder alloy powder, flux and vehicle, which is capable of forming metallurgical bonds at a given soldering conditions (Figure 3.1.1).

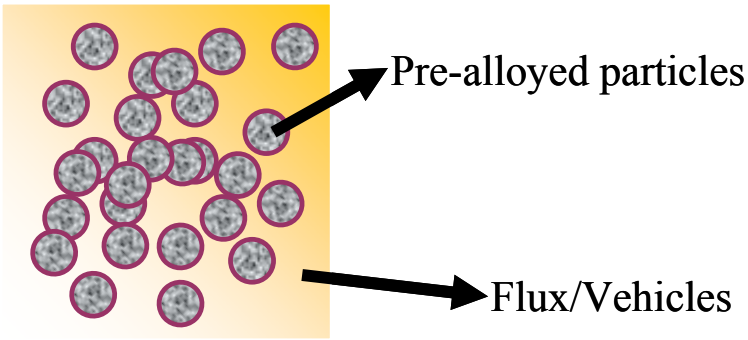

Figure 3.1.1 the composition of solder pastes.

Solder alloy powders are usually tin/lead (SnPb), lead-free solder materials, such as tin/silver (SnAg), tin/silver/copper (SnAgCu), tin/copper (SnCu) and so on. The flux can cause the alloy powders and the surfaces to be joined to maintain a clean and metallic state. The vehicle is carrier for the solder powder, provides a desirable rheology and protect the molten solder and the cleaned substrates from re-oxidation.

3.1.1 Solder alloy

The elements used in solder alloys are tin, lead, silver, copper, bismuth, indium, antimony and cadmium. Phase diagram can be used to determine the eutectic point and the corresponding compositions for the solid solution. Several methods can be used to make the solder alloy powders, such as chemical reduction, decomposition, mechanical

processing of solid metal, atomization of liquid metals and so on. Chemical reduction method and decomposition can be used to prepare fine solder alloy particles. Mechanical processing of solder metal can be used to prepare flake like particles, while powders to be used in solder paste are mostly produced by atomization because of desirable inherent morphology and shape of resulting particles.

Melting range, flow rate, particle morphologies are important parameters for solder powders. The melting range of solder powders are usually tested by differential scanning calorimeter (DSC). Table 1.2.1 shows the melting point of SnPb solders and lead-free solders. The particle size, size distribution and shapes are usually tested by scanning electron microscopy (SEM), light scattering and so on.

Some of the other physical properties, like viscosity, surface tension, thermal, electrical properties and thermal expansion coefficient are also very important for the solder materials. For the SnPb alloys, the surface tension, thermal and electrical conductivity decrease with increasing lead content, while viscosity and thermal expansion coefficient increase with increasing lead content.

3.1.2 Flux

The function of fluxes in solder paste is to chemically clean the surfaces to be joined, to clean the surface of solder powder, and to maintain the cleanliness of both substrate surface and solder powder surface during reflow so that a metallic continuity at the interface and a complete coalescence of the solder powder during reflow can be achieved (Figure 3.1.2).

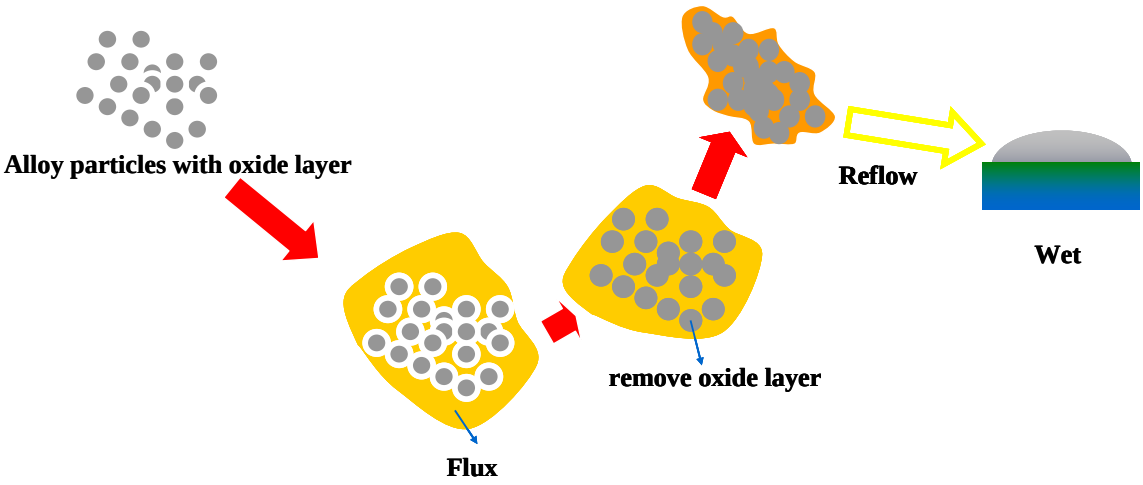

Figure 3.1.2 The function of flux.

There are several kinds of fluxes:

- Type R- rosin flux, the weakest, containing only rosin without the presence of activator.
- Type RMA (mildly activated rosin) is a system containing both rosin and activator.
- Type RA is a fully activated rosin and resin system, having a higher flux strength than the RMA type.
- Type OA is an organic acid flux and possessing high fluxing activity and is generally considered corrosive.
- Type SA (synthetic activator) is designed to improve fluxing activity on hard-to-solder surfaces. The SA flux displays better wetting ability than RA flux and is equivalent to OA flux.

The major components of unmodified rosin are abietic acid, isopimaric acid, neoabietic acid, pimaric acid, dihydroabietic acid and dehydroabietic acid. The chemical structures of these acids are shown in Figure 3.1.3.

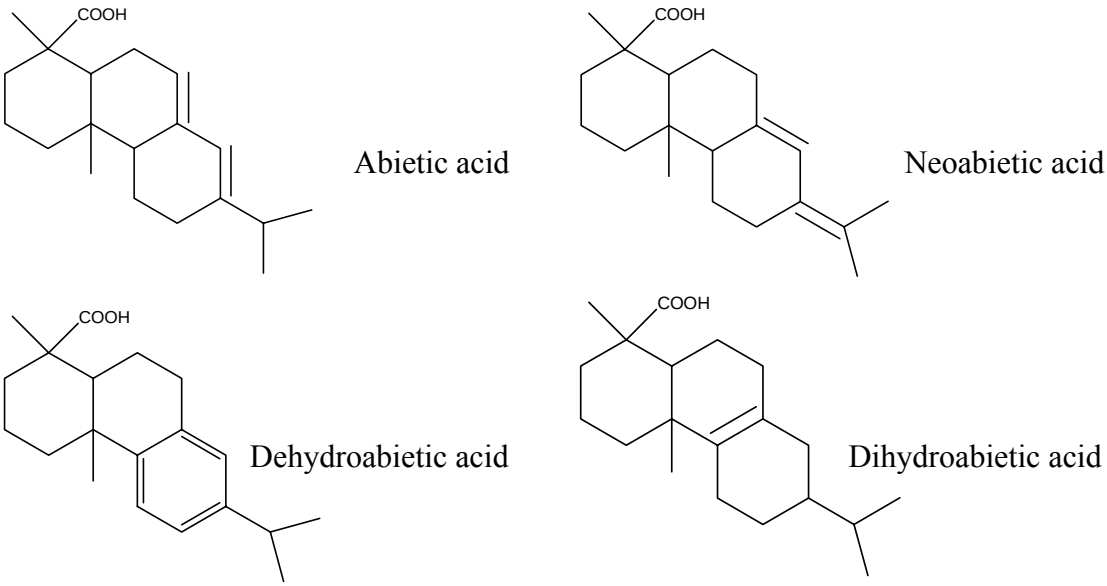

Figure 3.1.3 The chemical structures of the acids in rosin.

3.1.3 Vehicle

The main compositions of vehicles we used in this section are tackifier, solvent, anti-oxidation agent and surfactants.

The tackifier is typically a medium-to-high viscosity, high surface tension liquid serving to wet the printed circuit board and the component, and retain the component in position during handling and reflow soldering. The tackifier usually comprises one or more alcohols, aromatic hydrocarbon solvents, aliphatic hydrocarbon solvents or polymers.

A suitable solvent vehicle includes any solvent which is chemically inert with the other components in the flux. Three important parameters for solvents are boiling point, viscosity and polarity. Alcohols are usually used as solvents. The more hydroxyl groups the solvents have, the better activity the flux will have.

Antioxidation agents are used protect the Sn and its alloy nanoparticles from oxidation. Butylated hydroxytoluene (BHT) and hydroquinone (Figure 3.1.4) are the typically used

antioxidation agents. Oxygen reacts preferentially with BHT or hydroquinone rather than oxidizing Sn alloy, thereby protecting them from oxidation.

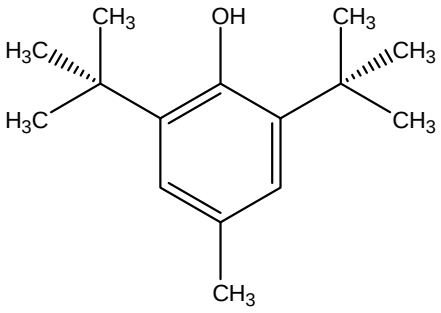

BHT

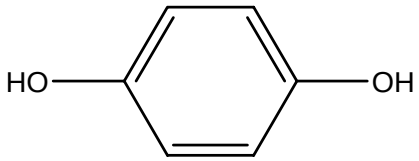

Hydroquinone

Figure 3.1.4 The chemical structures of BHT and hydroquinone.

The solder surfactant is a compound which improves the solder wetting rate of a surface and enables better and more uniform spreading of molten solder across the surface to be soldered. Suitable surfactants include polybasic acids, e.g., polycarboxylic acids such as dicarboxylic and tricarboxylic acids. The dibasic acids typically have 4 to 10 carbon atoms. Suitable tricarboxylic acids typically comprise acids having 6 to 7 carbon atoms. Other suitable surfactants include hydroxyl substituted polybasic acids, such as tartaric acid and citric acid. The selected surfactant is present in the flux mixture in an amount of at least one weight percent of the resultant flux mixture.

3.1.4 Solder pastes

The solderability, flow properties, wetting properties and solidification are important physical properties for the solder pastes. Solderability is the ability to achieve a clean, metallic surface on solder powder and on substrates during the dynamic heating process so that a complete coalescence of solder powder particles and good wetting of molten

solder on the surface of the substrates can be formed. Solderability depends on fluxing efficiency by the solder pastes and the quality of surface of substrates.

When heat is applied to the pastes through any means, the paste tends to spread or slump due to gravity and to thermal energy generated. The surface energies of the liquid and the solid substrates are key factors in determining the spreading and wetting properties. For a system with liquid to wet the solid substrate, the spreading occurs only if the surface energy of the substrate to be wetted is higher than that of the liquid to be spread.

The solidification of liquid metal occurs by nucleation and crystal growth. Dendritic growth during solidification is a common phenomenon in pure metals and alloys. The heat flow during the solidification and the crystal structure of the alloy are crucial factors to the properties and structure of the solidified alloy.

Application techniques for the solder pastes usually include printing and paste dispensing. Printing is a viable method to economically produce accurate and reproducible transfer of paste onto the designed pattern, but only suitable for flat surface. However, paste dispensing can be used for irregular surface or hard-to-reach area.

Conduction reflow is most suitable for the assemblies with flat surfaces, composed of thermal conductive materials as the substrates and with single-side component/device populations (fast heating rate and operational simplicity). Infrared reflow is a dynamic process. The precise temperature profile depends on solder alloy composition, properties of the pastes and assembly involved. Some other reflow methods, such as vapor phase reflow, convection reflow, hot gas reflow, resistance reflow, laser reflow, induction reflow are also being used.

Residue is composed of polar organics, nonpolar organics, ionic salts and metal salts of organics. The cleaning solvents include trichlorotrifluoroehtane, 1,1,1-trichloroethane, actone, methylene chloride, low carbon-chain alcohols, water and so on. Basic techniques: vapor degreasing, liquid spray, liquid immersion, high pressure spray and liquid immersion with ultrasonic acid.

Table 3.1.2 The composition of flux and vehicle made by our group.

Fluxing agent	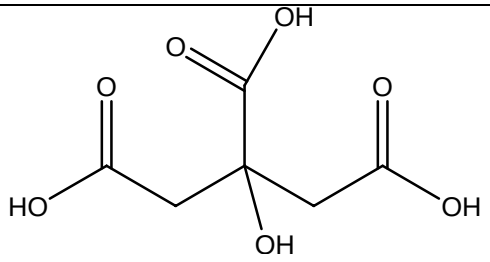
Tackifier	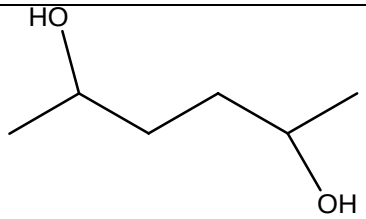
Surfactant	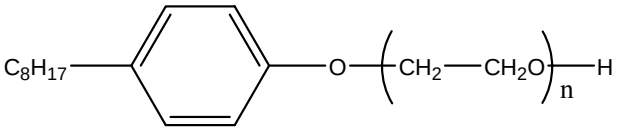
Solvent	CH_3CH_2OH 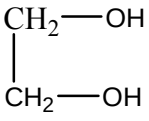 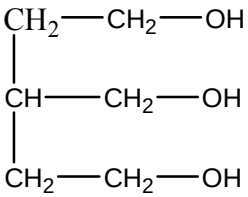
Antioxidation	BHT

A certain amount of fluxing agent, solvent, anti-oxidation agent, surfactants and tackifier were mixed together to prepare the flux and vehicle for the SnAg or SnAgCu alloy nanoparticles. Table 3.1.2 shows the composition of the flux and vehicle we made and their corresponding chemical structures.

3.2 Wetting Properties of the Nano Solder Pastes

3.2.1 Preliminary wetting studies of SnAg alloy nanoparticles pastes

The SnAg alloy nanoparticles (sample 1 in Table 2.4.1) were mixed with an acidic type flux to form the nano solder pastes at room temperature. A copper foil was cleaned by hydrochloric acid to get rid of the oxide layer and then rinsed with DI water for 4 times. Thereafter, the nano solder pastes placed on top of the copper foil were put into a 230 °C oven in an air atmosphere for 5 mins. The cross-section of the sample after reflow was shown in Figure 3.2.1. It was observed that the SnAg alloy nanoparticles completely melted and wetted on the cleaned copper foil surface. The energy dispersive spectroscopy (EDS) results revealed the formation of the intermetallic compound (IMC) of Cu_6Sn_5, which showed scallop-like morphologies in Figure 3.2.1. The thickness of the IMC was approximately 4.0 μm. Further studies on the wetting properties of different sized SnAg alloy nanoparticles at different reflow temperatures are still on going.

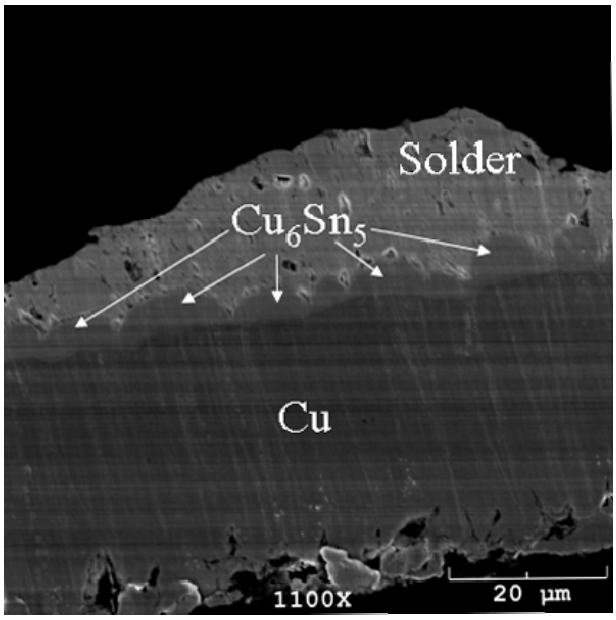

Figure 3.2.1. SEM image of the cross-section of the wetted SnAg alloy nanoparticles (sample 1 in table 2.4.1) on the cleaned copper foil.

3.2.2 Preliminary wetting studies of SnAgCu alloy nanoparticles pastes

Nano lead-free solder pastes were formed by dispersing the synthesized SnAgCu alloy nanoparticles into the flux and vehicle system. A carboxylic acid was used as the fluxing agent. The vehicle system mainly consists of a tackifier, a surfactant, solvents, anti-oxidation agents, etc. The tackifier is typically a medium-to-high viscosity, high surface tension liquid serving to wet the printed circuit board and the component, and retain the component in position during handling and reflowing process. The surfactant is a compound which enables better and more uniform spreading of molten solder across the surface to be soldered. The anti-oxidation agents were used to protect the molten solder and substrates from oxidation.

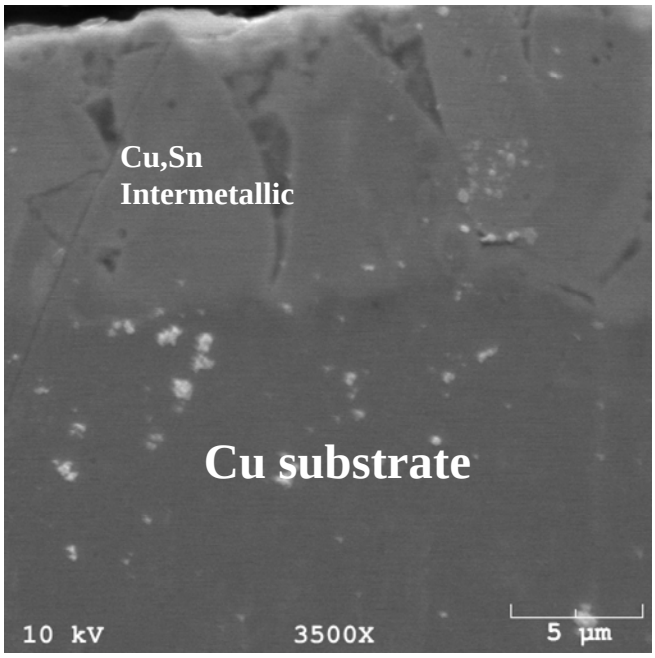

Figure 3.2.2. SEM image of the cross-section of the wetted 50 nm SnAgCu alloy nanoparticles on copper foil.

A copper foil was cleaned by hydrochloric acid to get rid of the oxide layer and then rinsed with DI water for 4 times. Thereafter, the ~50 nm (average diameter) SnAgCu alloy nanoparticle pastes placed on top of the copper foil were put into a 220 °C oven in an air atmosphere for 5 mins. The cross-section of the sample after reflow was shown in Figure 3.2.2. It was observed that the SnAgCu alloy nanoparticles completely melted and wetted on the cleaned copper foil surface. The energy dispersive spectroscopy (EDS) results revealed the formation of the intermetallic compounds (Cu_6Sn_5), which showed scallop-like morphologies in Figure 3.2.2. The thickness of intermetallic compounds was approximately 10.0 μm. Further studies on the wetting properties of different sized SnAgCu alloy nanoparticles at different reflow temperatures are still on going.

CHAPTER IV

ELECTRICALLY CONDUCTIVE ADHESIVES PREPARATION AND CHARACTERIZATIONS

4.1 Isotropic Conductive Adhesives Filled With Nano Sized Fillers

4.1.1 Introduction

Tin/lead (Sn/Pb) solders have been used as electrical interconnect in most areas of electronic packaging. Lead, one of the components in solder, has long been recognized as health threat to human beings [87]. In addition, worldwide regulations against the use of lead in the electronics has been severe. In particular, Japan has started to ban imports and exports for the lead-containing electronics since January 2005. The European Union (E.U.) plans to start the regulation from 2006. Therefore, the elimination of lead from the interconnect materials [88] has been an urgent research project in the electronics industry. Nowadays, two groups of materials are being pursued as possible alternatives for lead-containing solders: lead-free metal solders such as Sn/Ag, Sn/Ag/Cu [89,90] and polymer based electrically conductive adhesives (ECAs) [91-94].

ECAs, one of the proposed lead-free candidate materials, are composed of polymer resins and conductive fillers. Metal particles such as silver, nickel, and copper have been employed as conductive fillers. Silver has the lowest electrical resistivity among single metals, and its oxide form is also conductive, unlike other metals. Due to these reasons, silver has been primarily used as conductive fillers in conductive adhesive materials.

For the next generation of the fine pitch interconnect technology (< 100 nm), finer particles incorporated conductive materials are required. Thus, nano scale conductive

fillers incorporated adhesives are expected to play an important role for fine pitch applications.

The previous researches have reported that the nano Ag filled adhesives showed higher bulk resistivity than the micron meter sized Ag flake filled ones. The resistivities of 10^{-2} Ω·cm and 10^{-4} Ω·cm from 60 wt.% nano Ag and 70 wt.% Ag flakes loadings, repespectively [95]. In some cases, nano Ag filled adhesives showed unmeasurable resistivity and non conductive behavior [96]. These increased bulk resisitivity of nano Ag filled polymer composites is due to the increased surface contact area.

In fact, even if the nanocomposite takes advantage for the fine pitch application, the increased contact resistance between the nanoparticles may reduce the electrical performance of the nanocomposites. The number of contacts between the small particles is larger than that between the large particles as shown in Figures 1.5.2 (a) and (b). The overall resistance of the ICA formulation is the sum of the resistance of fillers, the resistance between fillers and the resistance between filler and pads (equation 1.5.1). In order to decrease the overall contact resistance, the reduction of the number of contact points between the particles may be obviously effective.

If nanoparticles are sintered together, the contact between fillers will be fewer. This will lead to smaller contact resistance (Figure 1.5.2 (c)). In order to improve the electrical properties of the nanocomposite, sintering nanoparticles in the polymer have been proposed and the sintering behavior of the nanoparticles was reported [97,98].

There are still challenges to fabricate the nanocomposites, one of which is the dispersion of the fillers in the polymer matrix. This is due to their large surface area that increases the viscosity of the formulation dramatically. For this reason, fabricating the high filler

loading nanocomposite is difficult. Therefore, enhancement of dispersion capability of nanoparticles is of great importance.

In this section, effects of various surfactants with different functional groups and carbon chain lengths on the sintering behavior of nano Ag filled adhesives were investigated. Their bonding and thermal debonding behaviors were also studied by using DSC and TGA.

In addition, the surface treated nanoparticles were incorporated into the polymer matrix and their electrical properties were evaluated. The morphology of the cured samples was investigated by Scanning Electron Microscopy (SEM). The interfacial properties between the surfactants and nanoparticles, and the electrical properties of the nanocomposites are discussed.

4.1.2 Experimental

4.1.2.1 Materials

A bisphenol-A type epoxy resin (Shell Chemical Co.) was selected as polymer matrix in the ICA formulations. The hardener was methylhexa-hydrophtha; ic anhydride (MHHPA) (Lindau Chemicals, Inc.). 1-cyanoethyl-2-ethyl-4-methylimidazole (2E4MZCN) (Shikoku Chemical Corporation) was employed as catalyst. The Ag nanoparticles synthesized by the combustion chemical vapor condensation (CCVC) were used as fillers [99]. Five different types of surfactants: S1, S2, S3, S4, and S5 were employed. Tetrahydrofuran (THF) (Fisher Scientific Inc.) was used as solvent.

4.1.2.2 Ag nanoparticles treated by surfactants

The molar ratio of Ag nanoparticles and surfactants was all set to 1:1. The solution of the nanoparticles, surfactant and solvent was sonicated for 2 hours. The solution was

centrifuged to remove the solvent and unreacted surfactant molecules. These particles were rinsed for three times by solvent. Finally the particles were placed in a vacuum for 24 hrs at room temperature to completely remove the solvent.

4.1.2.3 Characterization Methods

Thermogravimetric Analysis (TGA, 2050 from Thermal Advantages Inc.) was used to investigate the weight loss of the surfactants treated nanoparticles. The debonding temperature between surfactants and Ag nanoparticles was determined by a standard differential scanning calorimeter (DSC, TA Instruments, model 2970). A sample of about 10 mg was placed into a hermetically sealed DSC sample pan and placed in the DSC cell under a 40 ml/min nitrogen purge. Non-isothermal scans were made on the samples at a heating rate of 5 ^{o}C/min, usually from room temperature to 300 ^{o}C. After the non-isothermal scan, the sample was cooled to room temperature and then re-scanned under the same heating rate from 20 ^{o}C to 300 ^{o}C. For morphology study, Field Emission Scanning Electron Microscopy (FE-SEM, JEOL 1530) was used.

4.1.2.4 Measurement of Resistivity of Coductive adhesives

Resistivity of the conductive adhesive formulation was calculated from the bulk resistance of the specimen with specific dimensions. Two strips of an adhesive tape were applied onto a pre-cleaned glass slide with a gap of 8.17 mm. The conductive adhesive paste was doctor-bladed within space, and cured at 150 ^{o}C for 90 min, the tapes were then removed. The bulk resistance (R) of this ECA strip was measured as well as the size of the specimen. The bulk resistivity (ρ) was calculated by using the following equation

$$\rho = \frac{t \times w}{l} \times R$$

Where, *l*, *w* and *t* are the length, width and thickness of the sample, respectively.

4.1.3 Results and discussions

4.1.3.1 Thermal Behavior of nanoparticles coated with surfactants

The surfactants coating on the particles and thermal debonding behavior between surfactants and Ag nanoparticles were studied through DSC and the amount of surfactant materials coated on the nanoparticles was investigated by measuring the weight loss in TGA.

Figure 4.1.1 shows the DSC and TGA curves of Ag nanoparticles treated by S1. Three endothermic peaks appeared in the first heating profile in the DSC curves. The first endothermic peak is the melting point of S1 molecules. Other two peaks (121.5 and 145.6 ^{o}C) correspond to the debonding temperature between the S1 and Ag nanoparticles. The crystallization peak of S1 can be seen from the first cooling scan. In the second heating profile, there is still the melting temperature of S1, but the two peaks at 121.5 and 145.6 ^{o}C have disappeared, which indicates that there were bonds formed between S1 and Ag nanoparticles. Weight loss results show that the amount of S1 was around 4.8wt%.

Figure 4.1.2 shows the DSC and TGA curves of Ag nanoparticles treated with S2. In the first heating scan of DSC curves, an endothermic peak at 90 ^{o}C was found which is believed to be the debonding temperature of S2 from Ag nanoparticles. In the second heating scan, this peak has disappeared. From TGA curves, the amount of S2 bonded to Ag nanoparticles is found to be about 2.1 wt%.

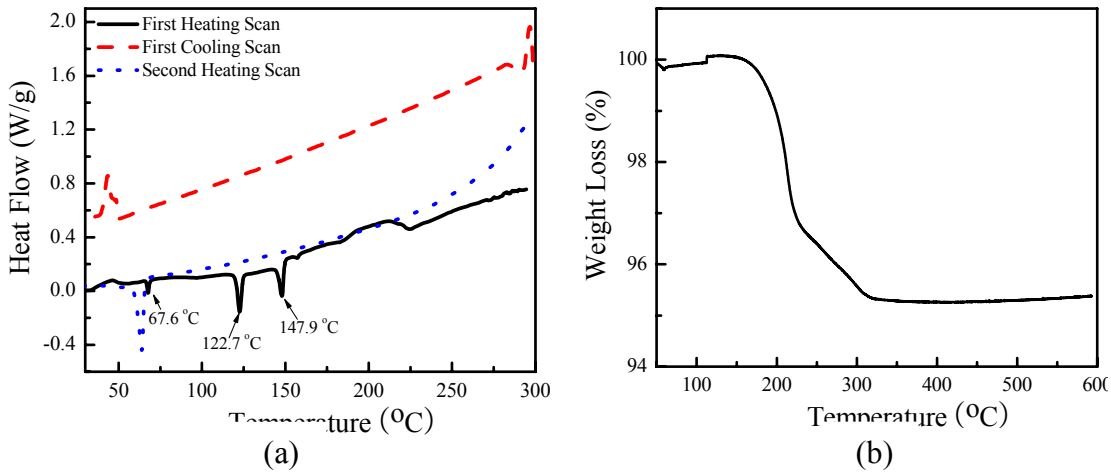

Figure 4.1.1. DSC (a) and TGA (b) curves of Ag nanoparticles treated by S1.

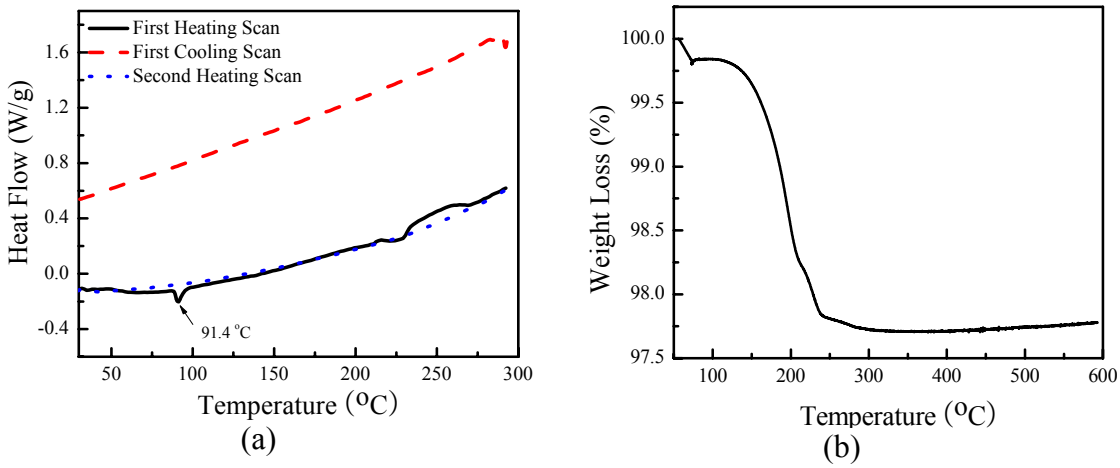

Figure 4.1.2. DSC (a) and TGA (b) curves of Ag nanoparticles treated by S2.

The DSC and TGA curves of Ag nanoparticles treated by S3 are shown in Figure 4.1.3. From the first heating scan of the DSC curves, it can be seen that the debonding temperature was around 132 °C. The amount of S3 bonded to Ag nanoparticles is around 1.1 wt%.

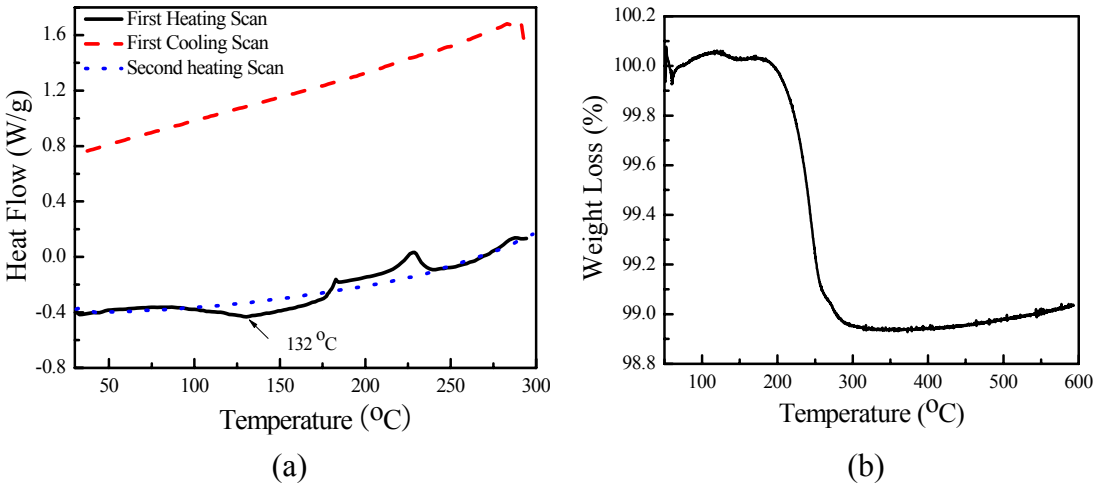

Figure 4.1.3. DSC (a) and TGA (b) curves of Ag nanoparticles treated by S3.

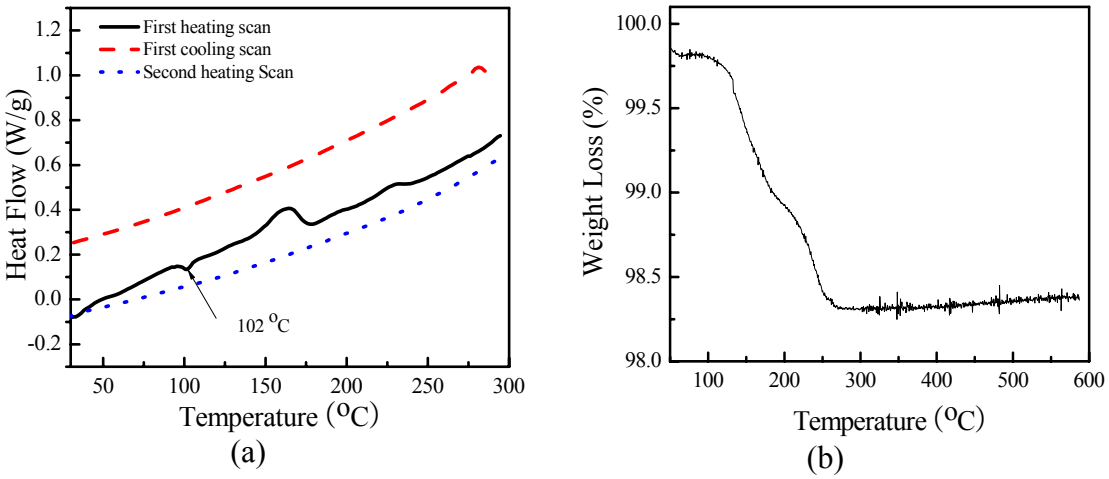

Figure 4.1.4. DSC (a) and TGA (b) curves of Ag nanoparticles treated by S4.

Figure 4.1.4 shows the DSC and TGA curves of Ag nanoparticles treated by S4. The peak at 102 °C is the debonding temperature of S4 and Ag nanoparticles, which can not be seen from the second heating scan. The amount of S4 bonded to Ag nanoparticles is around 1.5 wt%.

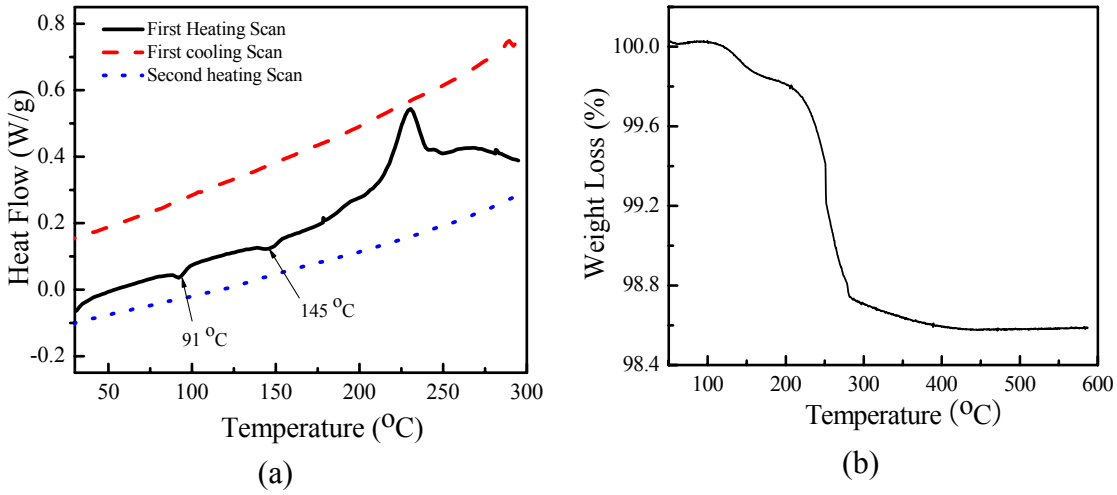

(a) (b)

Figure 4.1.5. DSC (a) and TGA (b) curves of Ag nanoparticles treated by S5.

The DSC and TGA curves of Ag nanoparticles treated by S5 are shown in Figure 4.1.5. The peak at 91 °C is the debonding temperature of S5 and Ag nanoparticles, which disappear from the second heating scan. The peak at 145 °C is the melting point of S5. The TGA results show that the amount of S5 bonded to Ag nanoparticles is around 1.2wt%.

Table 4.1.1. Thermal debonding behavior of different surfactants and Ag nanoparticles.

Acid	S1	S2	S3	S4	S5
Melting Point (°C)	~70	Liquid at R.T.	~150	<150	<100
Debonding temperature (°C)	122.41 144.30	89.77	107.92	102	145.72
Debonding Energy (J/g)	26.7 29.6	26.7	64.5	40.0	33.7
Debonding Energy (kJ/mole)	7.6 8.4	3.5	9.4	4.2	4.4

Table 4.1.1 shows the thermal debonding behavior of Ag nanoparticles treated with different surfactants. The debonding temperature and debonding energy of each surfactant was calculated from the DSC.

4.1.3.2 Morphology of the annealing nanoparticles

Figure 4.1.6 shows the morphologies of Ag nanoparticles treated by surfactants after annealing at 150 ^{o}C for 30 min respectively. From these pictures, it can be clearly seen that after annealing at 150 ^{o}C for 30 mins, the untreated Ag nanoparticles, Ag nanoparticles treated with S3, S4, and S5 show sintering behavior, while no clearly sintering behavior is observed from S1 and S2 treated Ag nanoparticles. The chain length of S1 and S2 is much longer than that of S3, S4 and S5. After debonding, the longer chain of S1 and S2 may cover on the surface of Ag nanoparticles, hinder contact between nanoparticles and prevent sintering behavior.

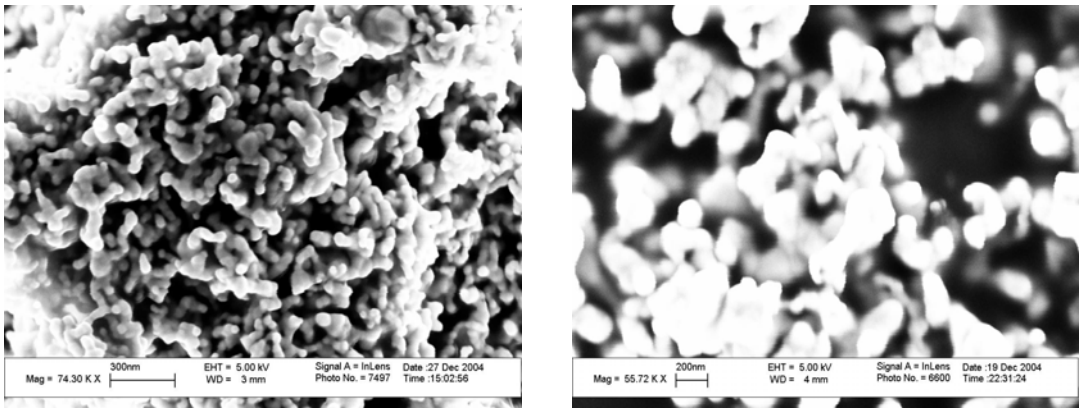

No annealing Annealing at 150 ℃ for 30 mins

a.) Untreated Ag nanoparticles

Figure 4.1.6. Comparison of the morphologies of Ag nanoparticles treated by different surfactants before and after annealing at 150 ^{o}C for 30 mins.

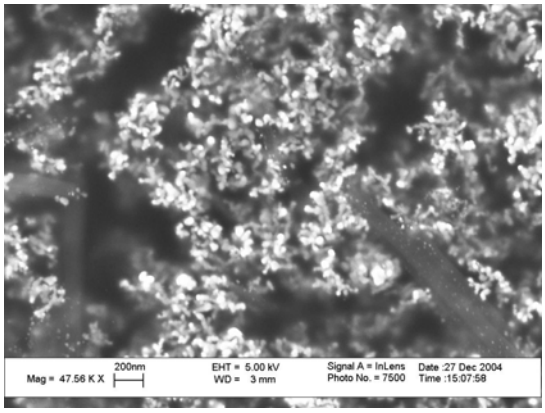

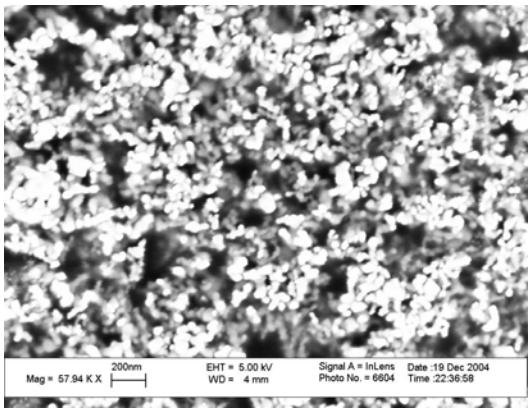

No annealing Annealing at 150 ℃ for 30 mins

b.) Ag nanoparticles treated by S1

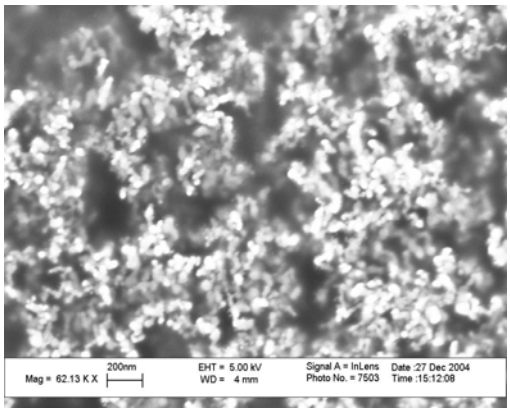

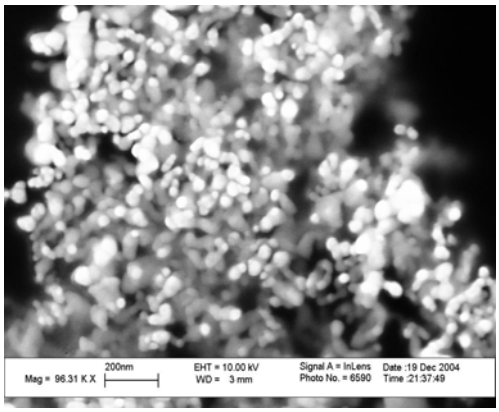

No annealing Annealing at 150 ℃ for 30 mins

c.) Ag nanoparticles treated by S2

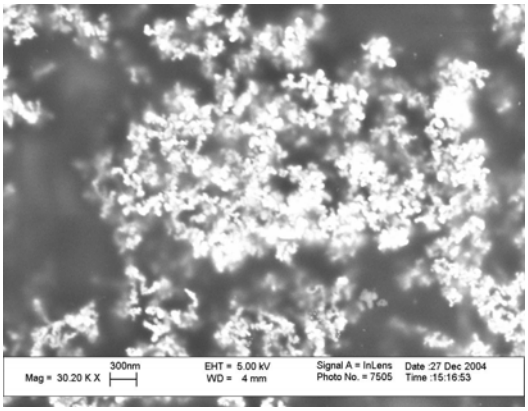

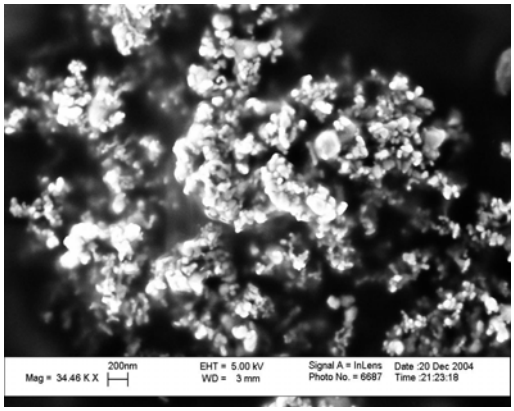

No annealing Annealing at 150 ℃ for 30 mins

d.) Ag nanoparticles treated by S3

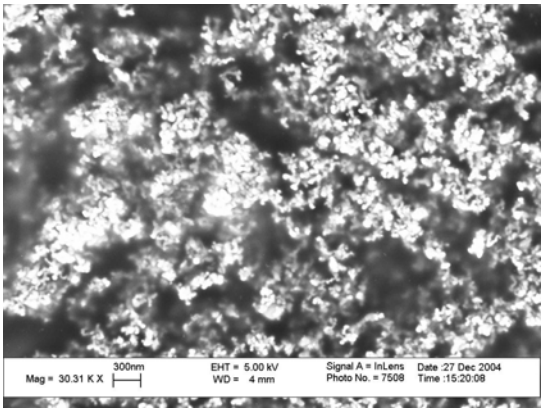

No annealing

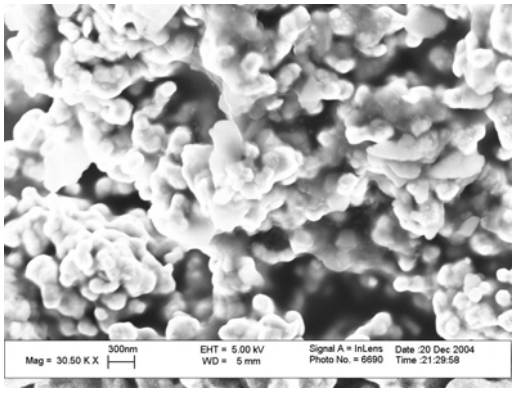

Annealing at 150 ℃ for 30 mins

e.) Ag nanoparticles treated by S4

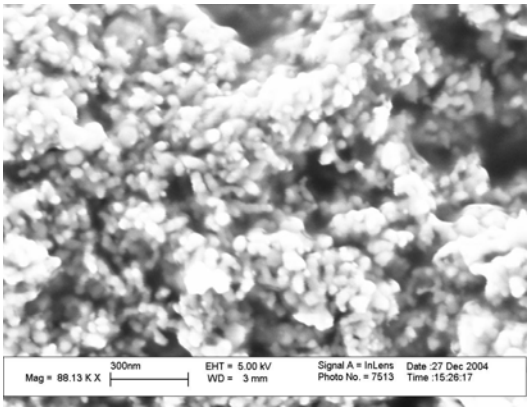

No annealing

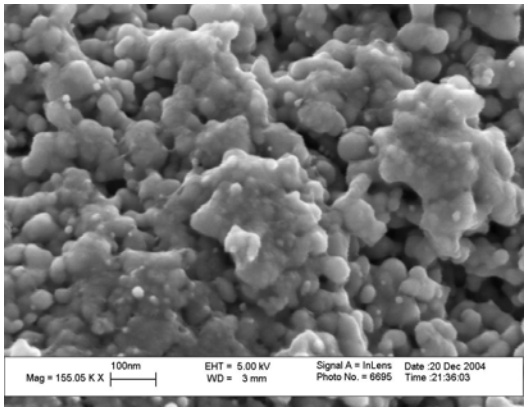

Annealing at 150 ℃ for 30 mins

f.) Ag nanoparticles treated by S5

Figure 4.1.6. continued.

4.1.3.3 Electrical properties of the conductive adhesives.

The Ag nanoparticles treated by the five different surfactants were incorporated into the epoxy resin and the electrical resistivity was measured. The surface treatment enabled to increase the filler loading up to 70wt%, while only 60 wt% of untreated Ag nanoparticles was incorporated into the epoxy resin, because the untreated particles were unable to be loaded by 70wt% due to the high viscosity of the mixture and the resistivity was 5.4×10^{-2} Ω.cm.

Table 4.1.2. The resistivity of the ICAs with different surfactants treated Ag nanoparticles as conductive fillers.

Samples	fillers	Weight percent of fillers	Resistivity (Ω.cm)
1[a]	Pure Ag nanoparticles	60 %	5.4×10^{-2}
2	S1 treated Ag nanoparticles	70 %	5.4×10^{4}
3	S2 treated Ag nanoparticles	70 %	2.4×10^{5}
4	S3 treated Ag nanoparticles	70 %	2.4×10^{-4}
5	S4 treated Ag nanoparticles	70 %	6.3×10^{-4}
6	S5 treated Ag nanoparticles	70 %	4.3×10^{-4}

[a] The filler loading is 60 wt%. The others are all 70 wt%

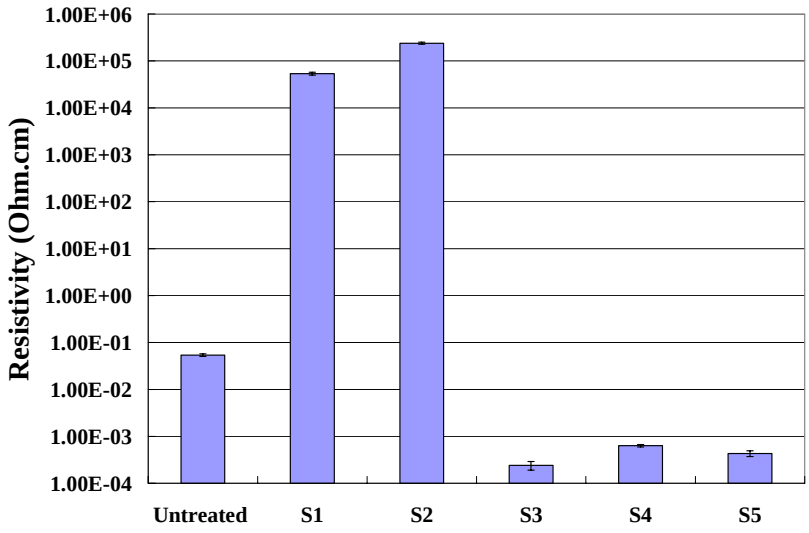

Figure 4.1.7. The resistivity of the ICA formulations with different surfactants treated Ag nanoparticles as conductive fillers.

Table 4.1.2 and Figure 4.1.7 show the resistivity of conductive adhesives filled with the surfactants treated nanoparticles. The S3, S4 and S5 incorporated ICA shows lower resistivity than the untreated, S1 and S2 treated particles incorporated one. Other than S3, S4 and S5, the resistivity of the nanocomposite treated with S1 and S2 molecules was not

acceptable. These two surfactant molecules may hinder contact between the particles and obstacle the sintering behavior in the epoxy matrix.

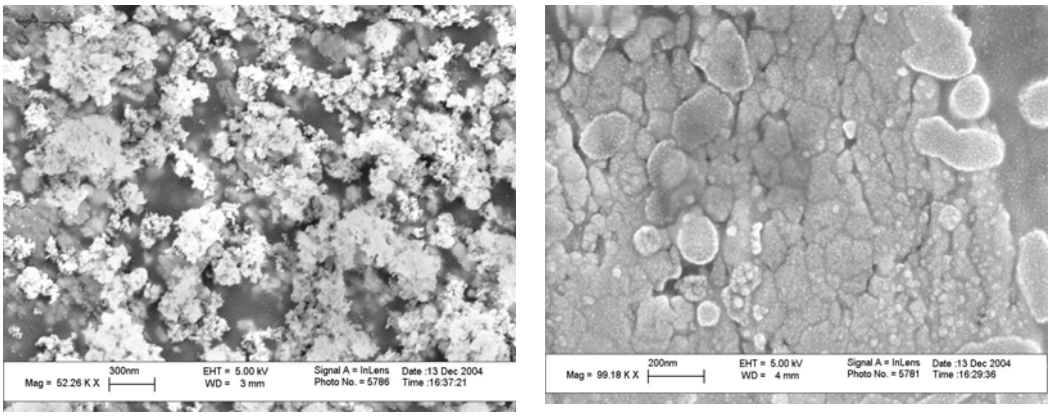

(a) (b)

Figure 4.1.8. Morphologies of nanocomposites with Ag nanoparticles treated by S2 (a) and S3 (b) as conductive filler respectively.

Figure 4.1.8 (a) shows the morphology of the conductive adhesives filled with Ag nanoparticles treated with S2 as conductive fillers. It can be seen some of the particles were agglomerated but not connected with each other. The resistivity of this formulation was much higher as in Table 2 (~2.4×10^{5} Ω.cm). Figure 4.1.8 (b) is the morphology of the conductive adhesives with Ag nanoparticles treated with S3 as conductive fillers, where the nanoparticles are sintered and form a significantly condensed structure. This sintered structure may result in reducing the resistivity to ~2.4×10^{-4} Ω.cm. To induce the nanoparticles sintered in the epoxy resin during curing or before curing, the chain length of the surfactants, the debonding temperature and the molecular behavior of the chemicals after debonding may be important parameters. Further study is in progress.

The curing profiles of these two formulated ICAs without fillers and with S3 treated Ag nanoparticles as conductive fillers are shown in Figure 4.1.9. The curing temperatures for

the two formulations were 137 and 142 ^{o}C respectively. The total heat of reaction of the unfilled epoxy formulation was 316 J/g, and the total heat of reaction of the S3 treated Ag nanoparticles incorporated ICAs was 326 J/g which was normalized with respect to the epoxy amount in the composites. It can be seen that surfactants treated Ag nanoparticles don't affect the curing behavior of epoxy resin.

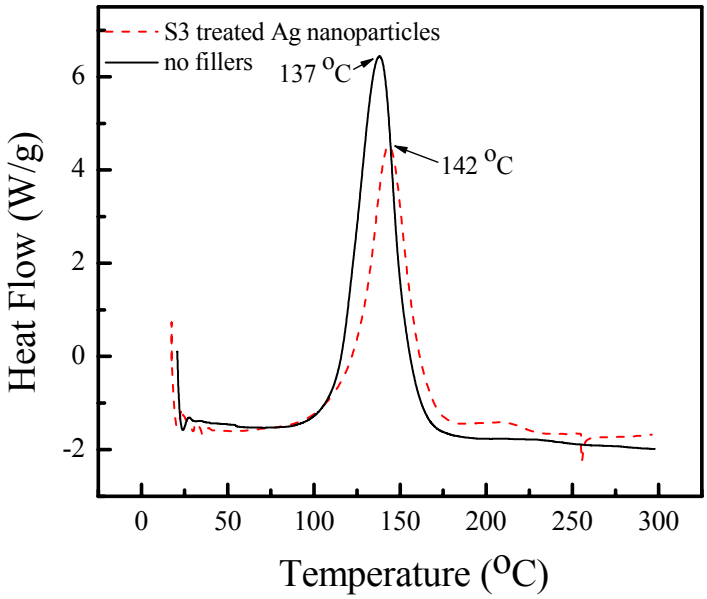

Figure 4.1.9. Curing behavior of ICAs without fillers and with S3 treated Ag nanoparticles as fillers.

4.1.4 Summary

Ag nanoparticles were treated by five different types of surfactants. These surfactants treated Ag nanoparticles showed different debonding temperatures during the first heating scan of the DSC test, which means the surfactants can be debonded from Ag nanoparticles at a certain temperature. Untreated, S3, S4 and S5 treated Ag nanoparticles showed sintering behavior after annealing at 150 ^{o}C for 30 mins. From the electrical measurements of the conductive adhesives incorporated with the Ag nanoparticles treated

with the five surfactants, S3, S4 and S5 show excellent electrical resistivity. The morphology study showed that sintering of nanoparticles resulted in the low resistivity.

4.2 Isotropic Conductive Adhesives Filled with Micron and Nano Sized Fillers

4.2.1 Introduction

Polymer nano composites have been paid much attention due to their unique electrical, thermal, mechanical and optical properties [100]. However, the dispersion of nanoparticles into a polymer matrix has been a bottle neck for nano composite fabrication. One of the best ways to uniformly disperse nanoparticles in a polymer matrix is to functionalize the particle surface with organic surfactants. The polymer matrix and inorganic particles often possess different polarity. Simple blending of particles with polymer will result in the aggregates of particles [101]. If the particles are surface functionalized with organic surfactants, they will become more compatible with the polymer matrix, resulting in a homogeneous dispersion of nanoparticles [102]. In the current research, the silver nanoparticles were synthesized and then surface functionalized for the nano composite applications.

Many types of organic compounds were used as surfactants to functionalize silver nanoparticle surface, such as thiol [103], pyridine [104], carboxylic acids [105], etc. Moskovits et. al. has characterized dicarboxylic acids adsorbed on silver particle surfaces by Surface-enhanced Raman Spectroscopy (SERS) [105]. It was found that the dicarboxylate group was responsible for the surface bond, probably chelating to silver surface sites. The molecule gains sufficient stability by bonding two carboxylate groups to the surface, and the molecule is able to adopt less favorable chain conformation. The

polymethylene groups can, therefore, be arranged in a way best to accomplish both carboxylate groups chelating.

Polymer composite materials have versatile applications in electronic packaging because of their low temperature processability and various functionalities endowed by other ingredients in the composites. Since silver filled polymer composites were first patented as conductive adhesives (ECAs) in 1956 [106], the conductive adhesives have been proposed as one of the alternatives of tin/lead (Sn/Pb) solders [107-111]. Lead, one of components in the commonly used eutectic solder, has long been known as a hazard to human beings. Thus, worldwide regulations against the use of lead in electronics have become more apparent. Therefore, the elimination of lead from interconnect materials [112] has been an urgent research project in electronics industry.

Comparing to the eutectic Sn/Pb solders, one of the main disadvantages of polymer composites is the lower conductivity resulting in poor current carrying capability. The overall electrical resistance of polymer composites is the sum of the resistance of fillers, the contact resistance between fillers and the contact resistance between filler and pads. In order to decrease the overall contact resistance, reducing the number of contact points between fillers could be effective.

In the composites with both silver flakes and nanoparticles as conductive fillers, if the finer particles are fused or sintered together, the number of contact points between fillers will be reduced (Figure 4.2.1 (c)). This will lead to lower contact resistance. In order to improve the electrical properties of the polymer composites, low temperature sintering of nanoparticles in the polymer matrix has been reported [98].

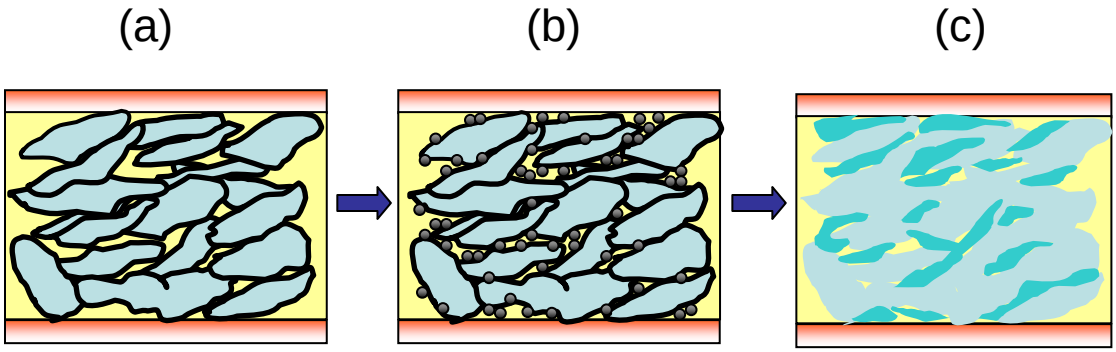

Figure 4.2.1. Schematic of particles and flakes between the metal pads: (a) is polymer composite with silver flakes as fillers; (b) is polymer composite with both flakes and nanoparticles as fillers; (c) is polymer composite with sintered particles among flakes as fillers.

Previous researchers have reported that the nano silver filled composites showed higher bulk resistivity than the micron sized silver flakes filled ones, the resistivities of 10^{-2} Ω·cm and 10^{-4} Ω·cm from 60 wt% nano silver and 70 wt% silver flakes loadings, respectively [95]. In some cases, nano silver filled composites showed unmeasurable resistivity and non conductive behavior [96]. This increased bulk resisitivity of nano silver filled polymer composites is due to the increased number of contact points between nanoparticles comparing to the same weight percent of sliver flakes.

In this section, both silver flakes and surface functionalized silver nanoparticles were incorporated into the polymer matrix and their electrical properties were studied. The interfacial properties between the surfactants, flakes and nanoparticles, and the electrical properties of the composites as well as their morphologies are discussed.

4.2.2 Experimental

4.2.2.1 Materials

The epoxy resin and hardener used were diglycidyl ether of bisphenol A (Epon 828, Resolution Performance Products) and hexahydro-4-methylphthalic anhydride (HMPA, Lindau Chemicals), respectively. The weight ratio of epoxy to hardener was 1:0.75. The

catalyst was 1-cyano-ethyl-2-ethyl-4-methylimidazole (2E4MZ-CN, Shikoku Chemicals Crop.) Silver nanoparticles were synthesized by the combustion chemical vapor condensation (CCVC) [99] method. A diacid [113] was used as surfactants to treat silver nanoparticle surface. All the chemicals were used as received.

4.2.2.2 Silver nanoparticles treated by surfactants

The molar ratio of silver nanoparticles to surfactants was set to 1:1. The solution of the nanoparticles, surfactants and ethanol was sonicated for 2 hours. From the TEM studies, there are no changes for the average size and size distribution of silver nanoparticles after sonication for two hours due to the existence of surfactants. The surfactants coated on the particle surface can prevent the nanoparticles from growing. The solution was centrifuged to remove the solvent and unreacted surfactant molecules. These particles were rinsed three times by solvent. Finally the particles were dried in a vacuum chamber for 24 hrs at room temperature.

4.2.2.3 Polymer composites

Different molar ratios of surface functionalized silver nanoparticles and silver flakes were incorporated into the mixture of bisphenol A and hexahydro-4-methylphthalic anhydride. The polymer composite was soniacted for one hour. Then the catalyst was incorporated and the mixture was sonicated again for 5 mins.

4.2.2.4 Characterization Methods

Thermogravimetric Analysis (TGA, 2050 from Thermal Advantages Inc.) was used to investigate the weight loss of the surfactant functionalized silver nanoparticles. The debonding temperature between the surfactant and silver nanoparticles was determined by a standard differential scanning calorimeter (DSC, TA Instruments, model 2970). A

sample of about 10 mg was placed into a hermetically sealed DSC sample pan and placed in the DSC cell under a 40 ml/min nitrogen purge. Non-isothermal scans were made at a heating rate of 5 ºC /min. After the non-isothermal scan, the sample was cooled to room temperature and then re-scanned under the same condition. For morphology studies, field emission scanning electron microscopy (FE-SEM, JEOL 1530) was used.

4.2.2.5 Measurement of the Resistivity of Polymer Composites

Resistivity of the polymer composites was determined from the bulk resistance of the specimen with the specific dimensions. Two strips of a Kapton tape (Dupont) were applied onto a pre-cleaned glass slide. The formulated pastes were doctor-bladed in-between the two strips, and cured at 150 ºC for 90 mins. The Kapton tapes were then removed. The thickness of the cured film was determined by Heidenhain (thickness measuring equipment, ND 281 B, Germany).

4.2.3 Results and Discussion

4.2.3.1 Synthesis and Surface Functionalization of Silver nanoparticles

Figure 4.2.2 shows the XRD patterns of the silver nanoparticles used. The average size of the synthesized silver nanoparticles calculated from XRD patterns by the Scherrer equation is around 16 nm [114].

The synthesized silver nanoparticles and silver flakes were both incorporated into epoxy resin as conductive fillers. There are still challenges to fabricate the nanocomposites, one of which is the dispersion of the nano fillers in the polymer matrix. This is due to their large surface area that increases the viscosity of the formulation dramatically. For this reason, it is relatively challenging to formulate highly filled nanocomposites. Thus, to

enhance the dispersion and to increase nano filler loadings in the epoxy resin, organic surfactants were used to functionalize silver nanoparticles.

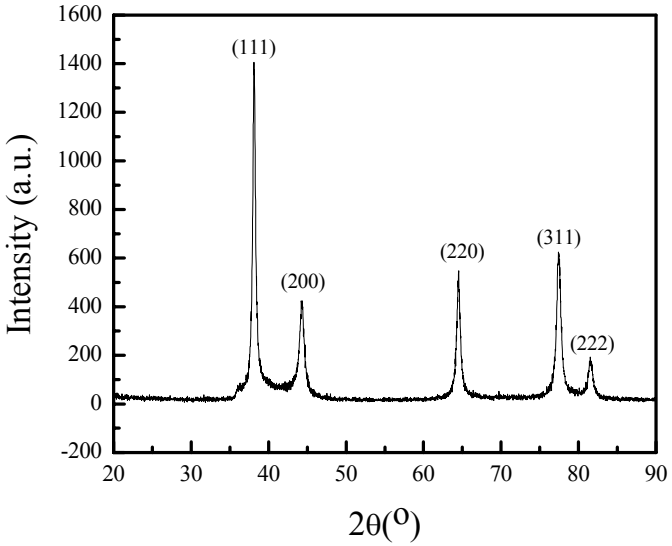

Figure 4.2.2. XRD patterns of the synthesized silver nanoparticles.

According to Moskovits's work [105], one of the diacids was selected to functionalize the silver nanoparticle surfaces. The DSC and TGA curves of the silver nanoparticles treated by diacids are shown in Figure 4.2.3. In the first heating scan of DSC, there was an endothermic peak at 91 ºC which corresponded to the melting point of the diacids. Another endothermic peak at 145 ºC was the possible temperature at which diacids were debonded from silver nanoparticles. This peak disappeared from the second heating scan. The TGA showed that the amount of diacids bonded to silver nanoparticles was around 1.2 wt%. For the pure diacid, more than 95wt% decomposition happened between 110 ºC and 210 ºC. For the functionalized silver nanoparticles, the decomposition between 110 ºC and 210 ºC may come from the contaminants on the silver particle surface and some pure diaicds, while the rest (with chelating bonds between silver and acid groups) gradually decomposed from 210 ºC to 420 ºC. Lee et. al. also found this kind of decomposition behavior from their mercaptosuccinic acid (MSA) coated silver

nanoparticles [115]. Both the DSC and TGA results confirmed the existence of diacids bonded to silver nanoparticles.

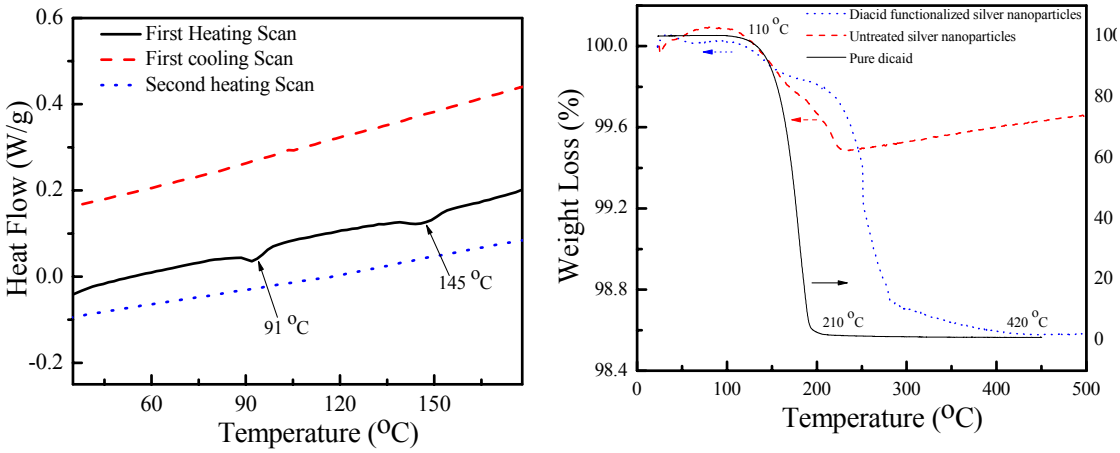

(a) (b)

Figure 4.2.3 DSC (a) and TGA (b) curves of silver nanoparticles treated by diacids.

In order to further prove the debonding behaviors between surfactants and nanoparticles, the morphologies of silver nanoparticles functionalized by diacids in the powder form after annealing at 100 ºC and 150 ºC for 30 mins were studied respectively. Compared with the images of Figure 4.2.4 (a) and (b), it can be seen that after annealing at 150 ºC for 30 mins, the silver nanoparticles functionalized by diacids showed sintered morphologies. During the annealing process, the surfactants will be debonded from the particles according to the DSC results and then sintered together at 150 ºC. At the same time, the diacids functionalized and untreated silver nanoparticles in the powder form were annealed at 100 ºC for 30 mins, respectively. Morphology studies (Figure 4.2.4 (c) and (d)) showed that the untreated silver nanoparticles were obviously sintered and the color of the powder changed to white, while the functionalized silver nanoparticles were almost not sintered and the color of the powder was still black. This is because at 100 ºC

the surfactants were still bonded to the nanoparticle surfaces, which prohibited the nanoparticle sintering.

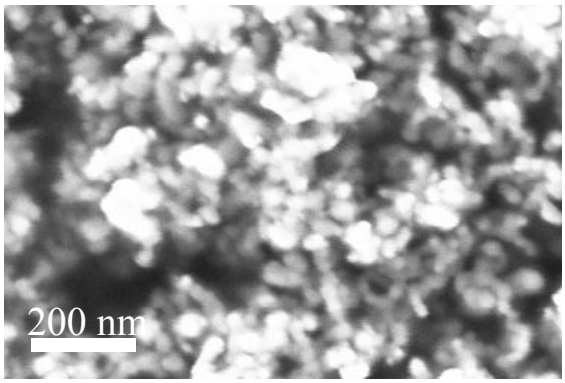

(a) Non-annealed surface functionalized silver nanoparticles

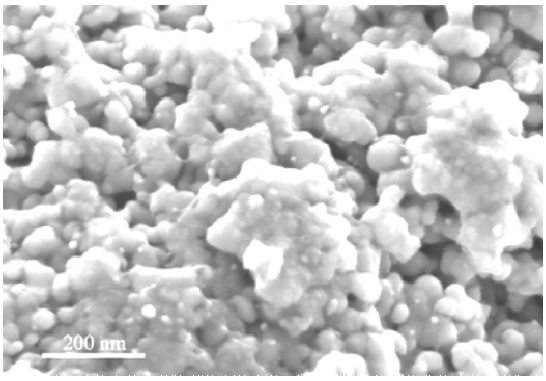

(b) Surface functionalized silver nanoparticles annealed at 150 ºC for 30 mins

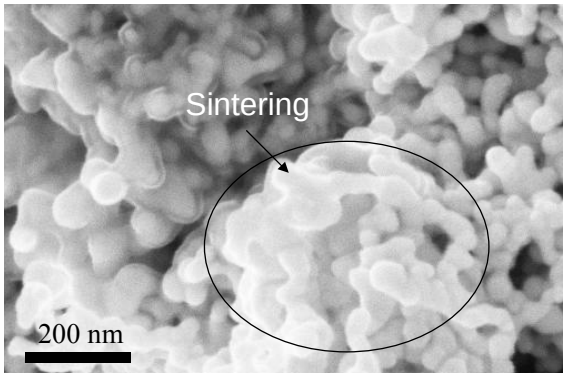

(c) Untreated silver nanoparticles annealed at 100 ºC for 30 mins

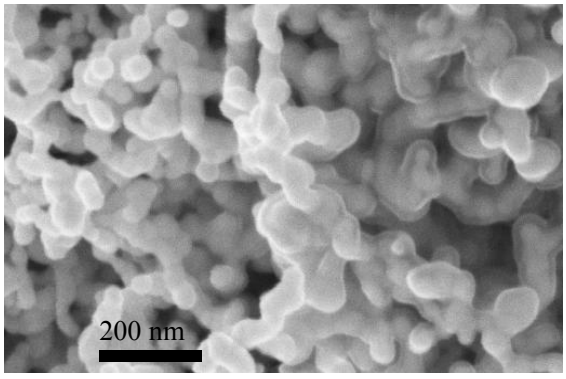

(d) Surface functionalized silver nanoparticles annealed at 100 ºC for 30 mins

Figure 4.2.4. Comparison of the morphologies of surface functionalized silver nanoparticle powders before and after annealing at 100ºC and 150ºC for 30 mins.

4.2.3.2 Electrical Properties of Polymer Composites

The silver flakes and surface functionalized silver nanoparticles were incorporated into the epoxy resin and the electrical resistivity of the composites was measured. The surface treatments enabled to increase the filler loading up to 80wt%.

Figure 4.2.5 shows the bulk resistivity of the polymer composites with various ratios of micron sized silver flakes to surface functionalized silver nanoparticles. The resistivity could be achieved as low as 5×10^{-6} Ω.cm, which is close to that of bulk silver (2×10^{-6} Ω.cm) and lower than that of eutectic Sn/Pb solder (1.7×10^{-5} Ω.cm). The small standard deviations of each formulation in Figure 5 show the good reproducibility of this process. However, when the same amount of untreated silver nanoparticles and silver flakes were used as conductive fillers, the resistivity would be 2×10^{6} Ω.cm, twelve orders of magnitude higher than that of surface functionalized silver nanoparticles and silver flakes incorporated one.

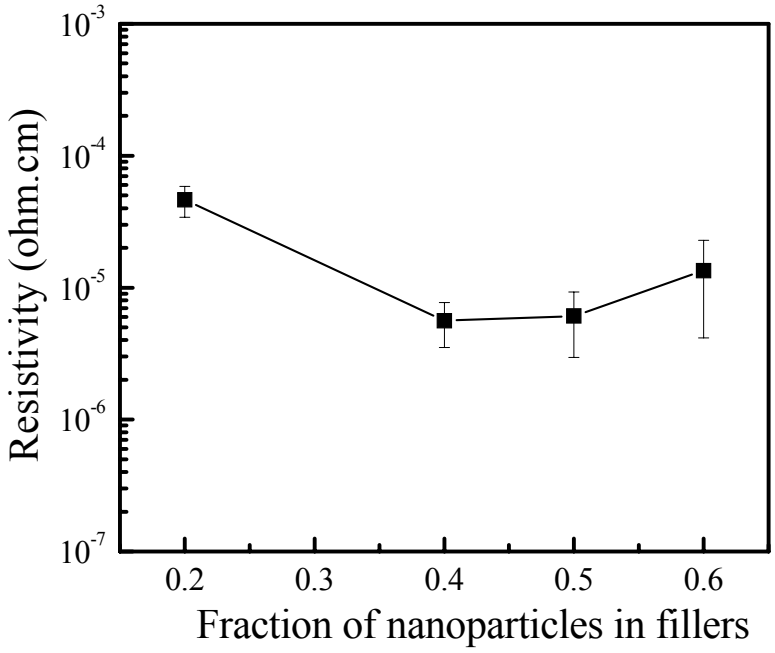

Figure 4.2.5. The bulk resistivity of the polymer composites with silver flakes and surface functionalized silver nanoparticles as conductive fillers.

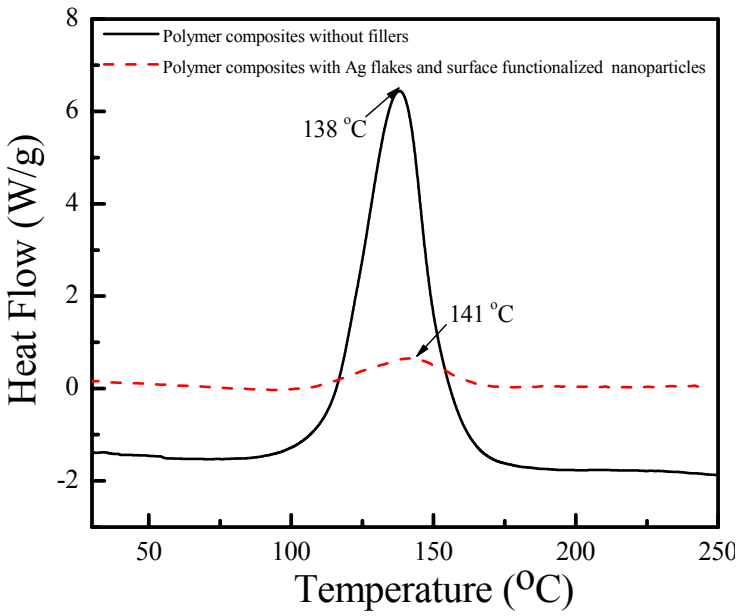

Figure 4.2.6. Curing behavior of polymer composites without fillers and with silver flakes and surface functionalized silver nanoparticles (6:4) as fillers.

The curing profiles of the polymer composites without fillers and with silver flakes and surface functionalized silver nanoparticles as conductive fillers are shown in Figure 4.2.6. The peak temperatures in the curing profiles for the two formulations were 138 and 141 ºC respectively. The total heat of reaction of the unfilled epoxy formulation was 316 J/g, while that of the silver flakes and surface functionalized silver nanoparticles incorporated polymer composites was 162 J/g which was normalized with respect to the epoxy weight in the formulations. It can be seen that the formulation with silver flakes and surface functionalized silver nanoparticles has a lower heat of fusion during curing. This is due to the lower crosslinking density of the epoxy resin. The mechanism of the epoxy resin curing is that the active imidazole group of the catalyst used reacts with epoxy molecules at the 1-N position to form an adduct which contains a highly reactive alkoxide ion. This alkoxide ion will continue to initiate the rapid anionic polymerization of the epoxy resin and form a crosslinked structure. But due to the existence of diacids, it will react with an

imidazole group to create a salt form, which may result in the loss of the catalyzing ability of the imidazole group. In addition, the carboxylic acid can also initiate the epoxy curing reaction, but its catalyzing ability is much weaker, which may lead to the lower crosslinking density of epoxy resins. In order to verify the influence of the diacid on the curing behavior of the epoxy resin, the diacid was incorporated into the unfilled epoxy formulation. It was found that the total heat of reaction of this formulation was 179.8 J/g. This is very close to that of the formulation with surface functionalized silver nanoparticle and silver flakes.

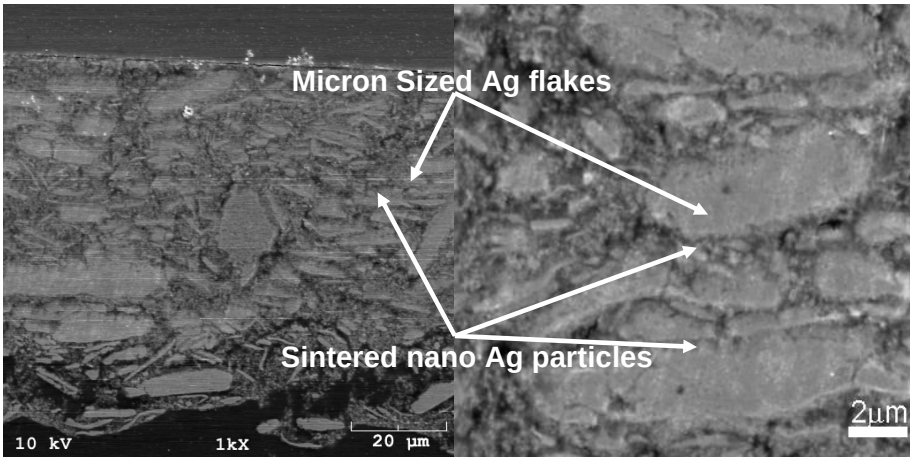

(a)

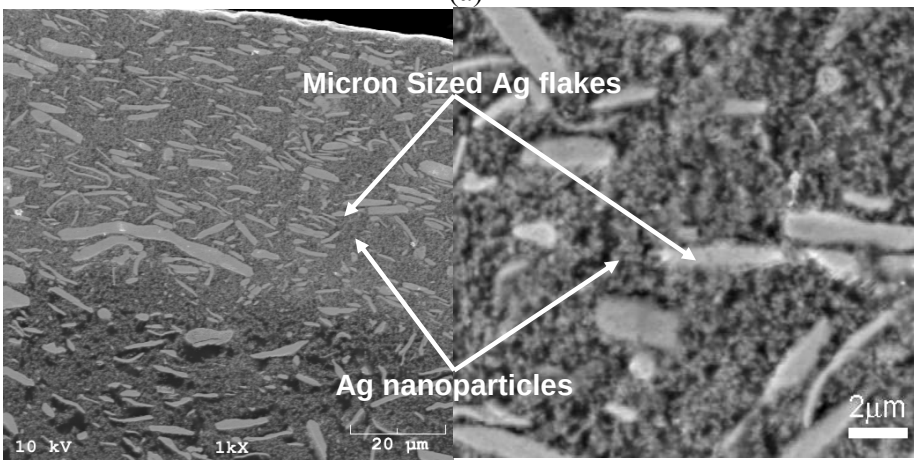

(b)

Figure 4.2.7. SEM images of polymer composites with (a) silver flakes and surface functionalized silver nanoparticles (6:4); (b) silver flakes and untreated silver nanoparticles (6:4) as fillers, respectively.

Figure 4.2.7 (a) shows the morphologies of the polymer composites filled with silver flakes and surface functionalized silver nanoparticles (6:4). It can be seen that the silver nanoparticles obviously sintered in-between the silver flakes and formed a significantly condensed structure. This sintered structure results in reducing the number of the interfaces between fillers and lowering the electrical resistivity. The mechanism for silver nanoparticles sintering by aids from diacids could be that the diacid is first adsorbed onto silver nanoparticle surfaces. This will help the dispersion of the nanoparticles in the epoxy resin which enables a higher filler loaded formulation. During the curing process, the diacid is debonded from the silver nanoparticles at a certain temperature. The debonded diacid may act as a flux to reduce the silver oxide layer covered on the silver nanoparticles due to the reaction between the carboxylic acid and silver oxide. This fluxing process aids the sintering process of silver nanoparticles, which decreases the number of contact points between the particles resulting in lower electrical resistivity. Figures 4.2.7 (b) are the morphologies of the polymer composites with silver flakes and untreated silver nanoparticles as conductive fillers, where the nanoparticles are not sintered very well. Significant amounts of non-sintered silver nanoparticles and the separation between silver flakes and silver nanoparticles are observed, which attributes to the high electrical resistivity.

Figure 4.2.8 (a) shows the contact resistance of polymer composites with different kinds of fillers on Ni/Au surfaces during 85ºC/85%RH aging. The Ni/Au surface is relatively inert and non-corrosive under high humidity. The contact resistance of the polymer composites with silver flakes and surface functionalized silver nanoparticles is much lower than that with silver flakes and untreated silver nanoparticles. Figure 4.2.8 (b)

shows the percentage of contact resistance shift with the increase of aging time. In the first several hours, the contact resistance increased because of moisture from 85ºC/85%RH, while the contact resistance decreased with increasing aging time. This may be due to that the nanoparticles sintering proceeded further and polar water molecules were absorbed into the composite materials. The sintering process is dependent upon various parameters such as temperature, pressure, time, the surface status of the powder and the powder size. Further studies on effects of these parameters on the sintering behavior of silver nanoparticles in the polymer resins are needed.

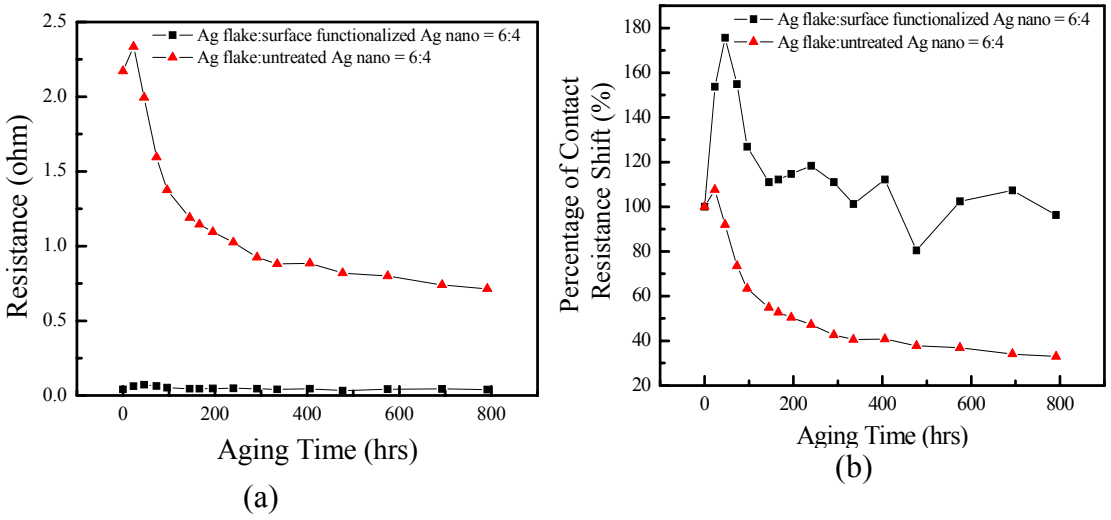

Figure 4.2.8 Contact resistances (a) and contact resistance shift (b) of polymer composites with different kinds of fillers.

4.2.4 Summary

Polymer composites with ultra-low electrical resistivity (~5×10^{-6} Ω.cm) were successfully created by using the combination of micron sized silver flakes and surface functionalized silver nanoparticles. The morphology studies revealed that this low resistivity was accomplished by dramatic reduction of the number of interfaces between

conductive fillers due to low temperature sintering of silver nanoparticles. In addition, the thermal analysis showed that the surfactant aided the sintering process by means of maintaining nanoparticle surfaces clean in the polymer resin and debonding before the gelation of the epoxy resin. The contact resistance of the formulation on Ni/Au surfaces decreased with aging time under 85ºC/85%RH. This may be because of further sintering of the nanoparticles under the elevated temperature and humidity.

4.3 High Performance Nonconductive Adhesives/Films Interconnects

4.3.1 Introduction

Among all the conductive adhesives, NCAs/NCFs are considered most popular for flip-chip assemblies due to their low cost. Conductive joints with NCAs/NCFs provide a number of advantages compared to other adhesive bonding techniques. The size reduction of electronic devices can be realized by the shrinkage of the package and the chip. Further advantages include ease of processing, good compatibility with a wide range of contact materials, low temperature cure and so on.

In spite of the advantages of NCAs/NCFs joints, there are still some challenging properties of NCAs/NCFs. The thermo-mechanical reliability of the NCAs/NCFs joints is poor due to high thermal stress caused by the coefficient of thermal expansion (CTE) mismatch between the epoxy materials, chips and substrates. At the same time, the thermal conductivities of the NCAs/NCFs materials are poor too because of the absences of conductive fillers. The generated heat at NCA/NCF joints under high current density can not be dissipated out efficiently. Therefore, the implementations of NCAs/NCFs as

interconnect materials for high performance device applications, such as microprocessor and application specific integrated circuit (ASIC) are limited.

In this section, a novel NCAs/NCFs material with the carbon nanotubes (CNTs) for high performance interconnects was developed. CNTs offer many promising characteristics for future electronic and device applications due to their extremely high thermal conductivities [9], outstanding mechanical properties [10], very high electrical conductivities by the ballistic effect [11] and a lower CTE value (negative at room temperature) [116]. A small amount of CNTs (0.03 wt%) was dispersed into the NCAs/NCFs materials to increase the thermal conductivities and at the same time to decrease the CTE of the NCAs/NCFs joints without degrading the electrically anisotropic conductivity of NCAs/NCFs joints. The high thermal conductivity of NCAs/NCFs will enable a higher current carrying capability and the lower CTE will enhance the thermo-mechanical reliability of the device. The thermal mechanical analyzer was used to study the CTE values of the CNTs filled NCAs/NCFs. The electrical properties and current carrying capabilities were studied for both the CNTs filled NCAs/NCFs and unfilled NCAs/NCFs. The other material properties of NCAs/NCFs joints, such as the curing profile and thermal stability were reported as well.

4.3.2 Experimental

4.3.2.1 NCAs/NCFs materials

The CNTs were synthesized by the chemical vapor deposition (CVD) method. The detailed experimental procedures used to fabricate CNTs were described previously [117]. A small amounts of CNTs (0.03 wt%) were dispersed into the epoxy resin by a blender. After the uniform dispersion of CNTs in the epoxy resin, the curing agent (30

wt%) was added. The mixture was then stirred again for 1 hour to achieve the well dispersed NCAs/NCFs materials. Finally, the mixtures were degassed under a vacuum for 3 hours to eliminate the air induced during stirring.

4.3.2.2 Characterization

Scanning electron microscopy (SEM) was used to characterize the morphologies of the as-synthesized CNT films. The SEM is JEOL 1530 equipped with a thermally assisted filed emission gun operating at 10 KeV. High resolution transmission electron microscopy (HRTEM, Hitachi 2000K TEM) were used to study the morphology of CNTs. TEM specimens were prepared by dispersing a few drops of the CNT solutions onto a carbon film supported by copper grids. A thermogravimetric analyzer (TGA, 2050 from Thermal Advantages Inc.) was used to investigate the thermal stability of NCAs/NCFs joints. The curing behavior of the NCAs/NCFs materials was studied by a differential scanning calorimeter (DSC, TA Instruments, model 2970). Thermal mechanical analyzer (TMA, TA Instruments, model 2940) was used to study the CTE of the NCAs/NCFs materials. The electrical resistance and current carrying capability of the NCF joints (contact area: $100 \times 100\ \mu m^2$) on Au-finished test vehicle was measured by a four-point probe method. The applied currents were varied from 0.5 to 4.2 A by a power supply (HP model 6553A, HP Hewlett Packard, Palo Alto, CA) and the voltage of the interconnect joints were measured by a Keithley 2000 multimeter (Cleveland, OH). The breakdown voltage of the NCAs/NCFs joints was studied by the curve tracer (type 576).

The thermal conductivity of the NCAs/NCFs was measured by LFA which is a sensitive, contact-free laser flash method (LFA 447). In this method, the flash lamp, samples and the infrared detector are vertically arranged. Both the released energy of flash lamp and

the length of the heating pulse can be adjusted via the 32-bit MS windows software named as Nanoflash. The furnace (room temperature to 300 ^{o}C) is directly integrated into the sample holder, creating a small thermal mass and therefore fast heating and cooling are possible. The thermocouple is positioned in the sample carrier for accurately measuring temperatures. Liquid nitrogen cooled Sb infrared detector is used to measure the temperature rise after the light pulse. All the data gathered from the measurements taken using the Nanoflash software is loaded into another software called LFA analysis. This software can do the calculation of thermal properties and make plot for all the measured values.

4.3.3 Results and Discussion

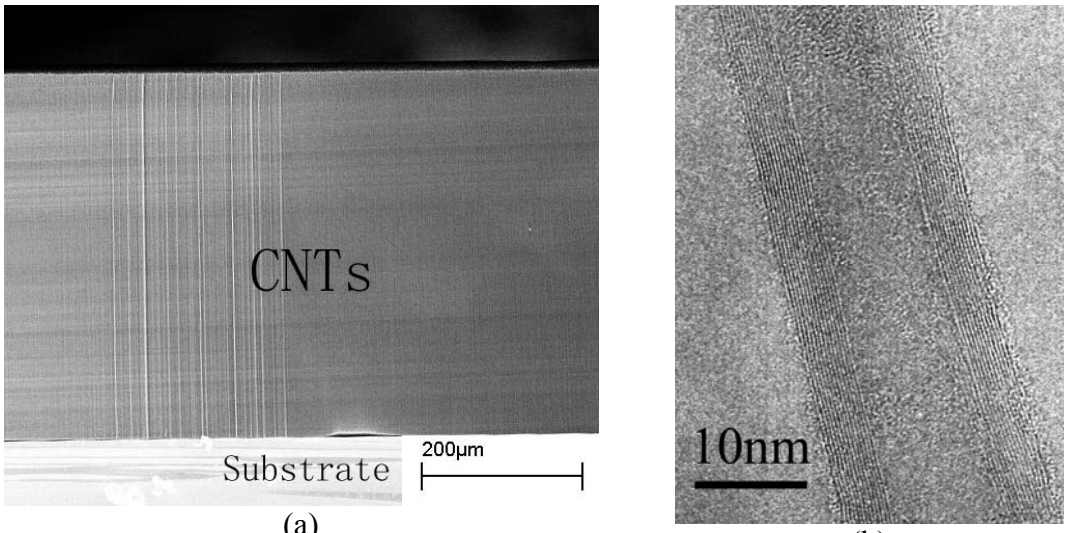

(a) (b)

Figure 4.3.1. The CNTs synthesized by chemical vapor deposition method: (a) SEM image of CNT films; (b) HRTEM image of a CNT.

Figure 4.3.1 (a) showed the SEM image of the as-synthesized aligned CNT films. Due to the high density of the catalyst layer, the CNTs formed a dense film with good alignment due to the strong Van de Waals force among tubes. Figure 4.3.1 (b) showed that the CNTs had multi wall structure and the diameter of each tube was approximately 20 nm.

A small amount of synthesized CNTs (0.03 wt%) were uniformly dispersed into epoxy resin to form the NCAs/NCFs materials. The curing behavior the NCAs/NCFs were first studied by differential scanning calorimeter. The DSC curves in Figure 4.3.2 show the effect of filler contents on the curing profiles of NCA composite materials. From the dynamic scan results, similar curing behaviors of different NCA composite materials were observed. This means that such a small amounts of CNTs will not affect the curing behavior of the epoxy resin.

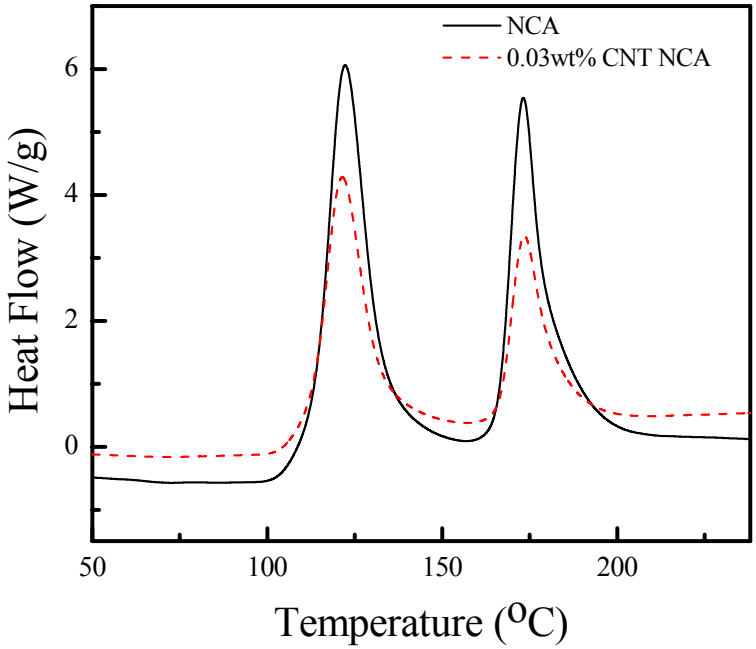

Figure 4.3.2. DSC curves of the curing profiles of 0.03 wt% CNT filled NCAs/NCFs and pure NCAs/NCFs.

The thermogravitational analysis was performed to evaluate the thermal stability of NCA/NCF materials with different content of fillers in Figure 4.3.3. The decomposition temperatures of two NCA/NCF composites were almost that same at 400 ^{o}C due to same epoxy resin used. The small amount of CNTs in the NCA/NCF composites doesn't influence the decomposition temperature.

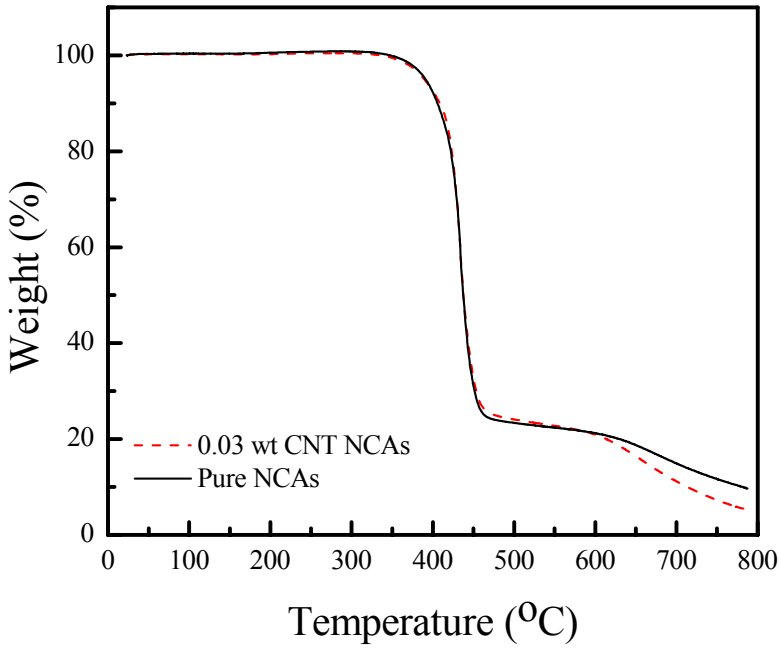

Figure 4.3.3. The TGA curves of NCAs/NCFs with and without CNTs.

CTEs of NCAs/NCFs materials with/without CNTs were measured using TMA. A typical TMA curve of the NCAs/NCFs is shown in Figure 4.3.4. The inflection point of thermal expansion curve is defined as TMA T_g. α_1 and α_2 are the CTE values of NCAs/NCFs before and after T_g, respectively. Test results are summarized in Table 4.3.1. With the increase of the CNT filler loadings, the CTEs of the NCAs/NCFs became smaller due to the lower CTE values of CNT itself [116]. By using 0.03 wt% CNTs, the CTE of the NCAs/NCFs was decreased with a value of 11 ppm/^{o}C. This significant CTE reduction will result in a better thermo-mechanical reliability of the device.

Table 4.3.1. The CTE values of NCAs/NCFs with different content of fillers

NCAs/NCFs	CTE ppm/^{o}C (α_1)	CTE ppm/^{o}C (α_2)
No CNTs	71.55	197.2
0.02 wt% CNTs	62.3	179.8
0.03 wt% CNTs	60.9	177.8

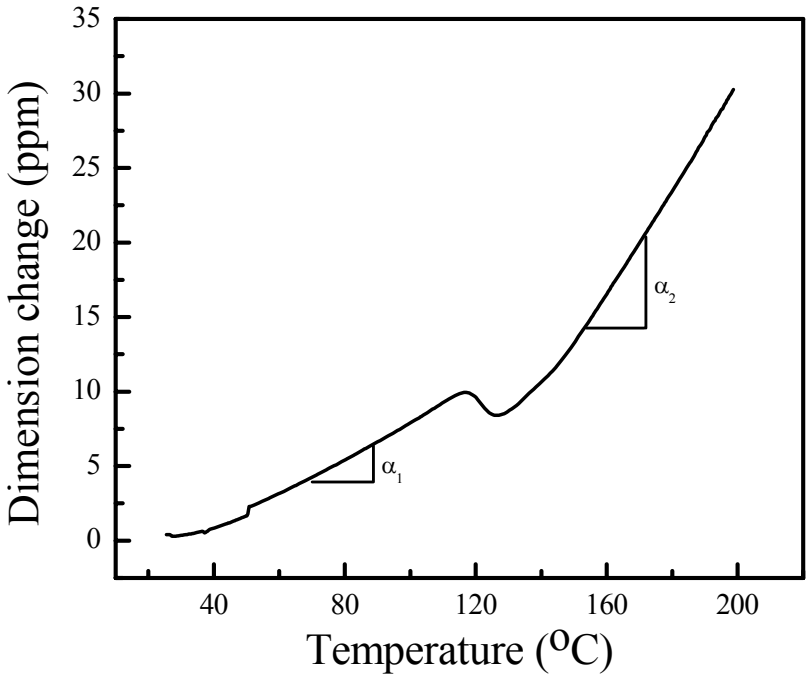

Figure 4.3.4. TMA curve of cured NCAs/NCFs materials, showing the definition of α_1 and α_2.

The electrical performance of the NCAs/NCFs with/without CNTs was studied. The current-voltage (I-V) relationship and correspondingly current-resistance (I-R) relationship of the NCAs/NCFs joints are shown in Figure 4.3.5 and 4.3.6, respectively. The current carrying capability (maximum current below which the I-V relationship remains linear) of the NCAs/NCFs without CNTs was 3.7 A, while that of the 0.03 wt% CNTs filled NCAs/NCFs was 4.2 A (Figure 4.3.5). The contact resistance for NCAs/NCFs joints without and with 0.03 wt% CNTs was around 5.6×10^{-4} and 4.6×10^{-4} ohm, respectively (Figure 4.3.6). The current carrying capability of the 0.03 wt% CNTs filled NCAs/NCFs was improved by ~14 % and the contact resistance was decreased by ~ 20%. The significantly improved electrical properties of the 0.03 wt% CNT filled NCAs/NCFs could be attributed to the more efficient dissipation of generated heat by the

small amount of CNTs and therefore enable higher current carrying capabilities of the joints

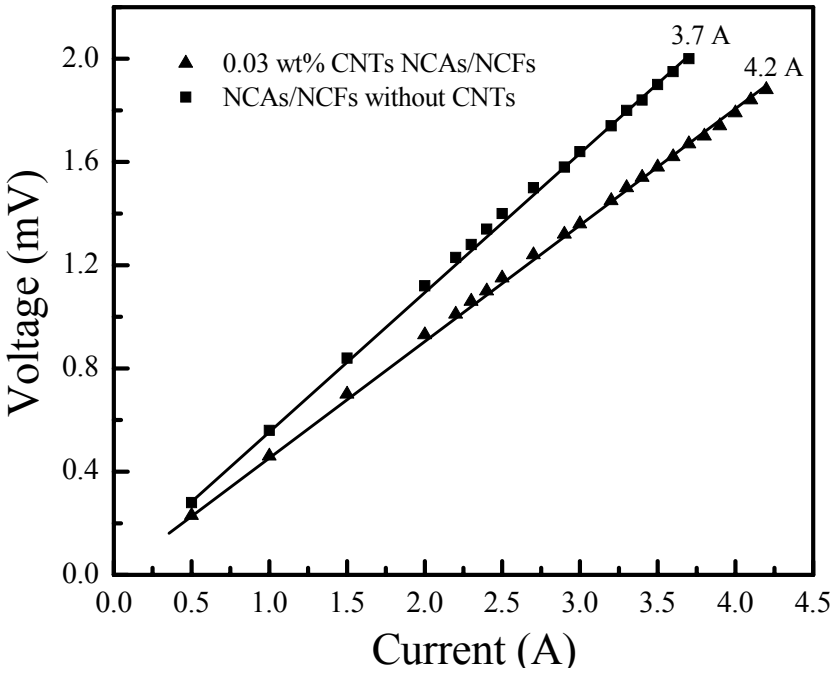

Figure 4.3.5. The I-V curves of NCAs/NCFs with and without CNTs.

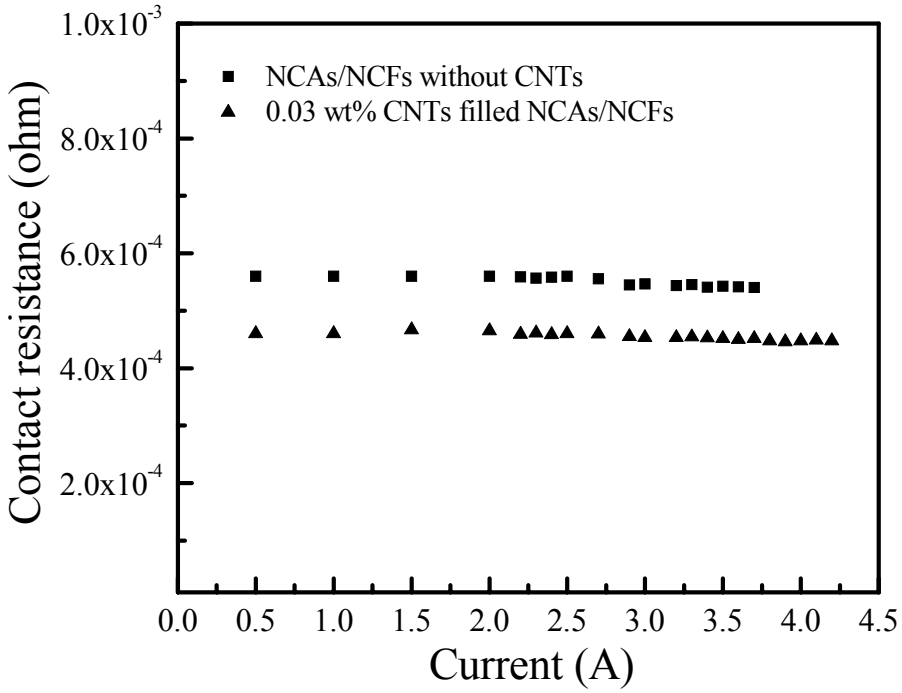

Figure 4.3.6. The contact resistance of NCAs/NCFs with/without CNTs.

Thermal conductivities of CNT/epoxy composites have been widely studied and the enhancement of thermal conductivity with the increase of filler content was already observed [118-120]. In this section, LFA was used to study the thermal conductivities of NCAs/NCFs without/with 0.03 wt% CNTs at different temperatures (Figure 4.3.7). It was observed that the 0.03 wt% CNTs resulted in an enhancement of the thermal conductivity of the NCAs/NCFs. For instance, at 25 ^{o}C, the thermal conductivity of the 0.03 wt% CNTs filled NCAs/NCFs was around 0.128 W/mK, compared to the unfilled NCAs/NCFs with 0.109 W/mK, an enhancement of 17%. And an enhancement of 11%, 19%, 23% was obtained at 50 ^{o}C, 75 ^{o}C and 100 ^{o}C, respectively. These small amounts of CNTs could help dissipate the heat out more efficiently and therefore enable higher current carrying capabilities of the NCAs/NCFs joints.

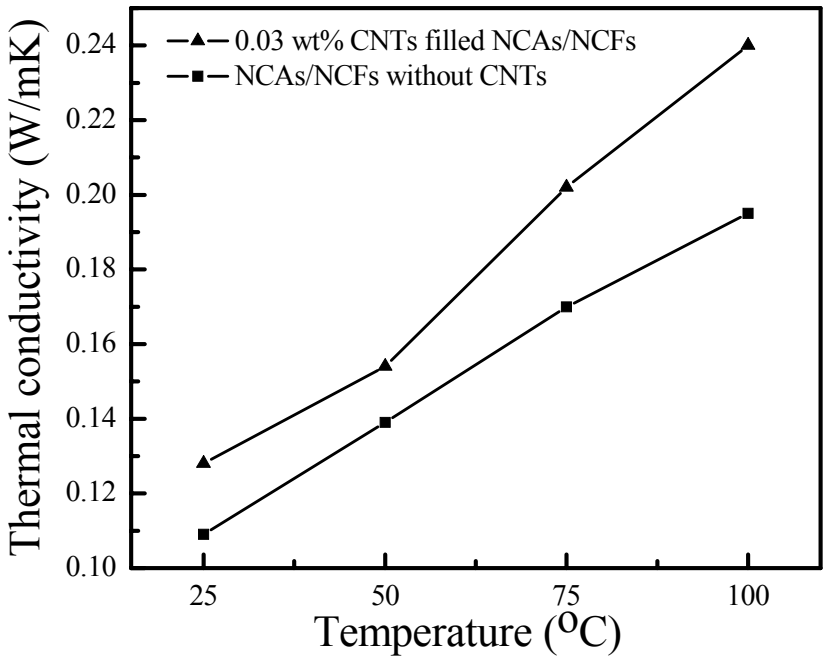

Figure 4.3.7. The thermal conductivities of NCAs/NCFs with and without CNTs.

The breakdown voltage of the NCAs/NCFs was studied by a curve tracer. The results showed that the breakdown voltage for both the unfilled NCAs/NCFs and 0.03 wt% CNTs filled NCAs/NCFs was larger than 1700 V with a film thickness of around 70 μm. The breakdown voltage characterizations confirmed that the 0.03 wt% CNTs in NCAs/NCFs didn't degrade the electrically anisotropic conductivity of NCAs/NCFs joints

4.3.4 Summary

A novel NCAs/NCFs materials have been successfully prepared for high performance interconnect applications. By using a small amount of CNTs (0.03 wt%), the CTE of the NCAs/NCFs was decreased with a value of 11 ppm/^{o}C and this significant CTE reduction will result in a high thermo-mechanical reliability of the NCAs/NCFs joints. At the same time, the current carrying capability of the 0.03 wt% CNTs filled NCAs/NCFs was increased by 14% comparing to the unfilled NCAs/NCFs, which is due to the high thermal conductivity of the CNTs and the generated heat can be dissipated out more efficiently.

CHAPTER V

CARBON NANOTUBES FOR LEAD-FREE INTERCONNECT APPLICATIONS

5.1 In-situ Surface Functionalized Carbon Nanotubes

5.1.1 Introduction

Nanoparticles have attracted considerable attention due to their unique chemical, physical, electronic and optical properties compared to their corresponding bulk materials [121,122]. Nevertheless, with the extremely high surface area to volume ratios and surface energies, the stabilization of synthesized nanoparticles becomes one of the primary challenges for some of their applications. To date, several stabilization agents or substrates have been used for metal nanoparticle synthesis, such as poly(N-vinylpyrrolidone) (PVP) [34,35,123], carboxylic acid [124,125], crown ether [126], sodium citrate [36], carbon nanotubes (CNTs) [127-133], etc. Among them, CNT-stabilized nanoparticles are important due to their potential applications as broad-band optical emitters [127], electrodes [128] and catalysts [129]. During the past decades, various methods have been developed to prepare different kinds of CNT stabilized metal nanoparticles, such as sonochemical [134,135], wet-chemical [128], vaporizing depositing [127], γ-irradiation [136] methods. But in these studies, the CNTs were all post treated to functionalize the surfaces with acid sites, such as refluxed with nitric acid or treated by γ-irradiation [137]. These acid sites are composed of carboxylic groups or hydroxyl groups, which can act as nucleation centers for metal ions during the reduction. However, the intrinsic electrical and mechanical properties of the CNTs would be affected by these harsh treatments due to the many damages on the CNT walls [138]. At

the same time, the aligned structure of the CNT films will be destroyed by these post treatment methods.

The synthesis of well aligned open-ended CNT stacks has been reported by our group [12]. In that study, H_2O was used to assist the selective etching of carbon atoms at the CNT caps as well as at the interface between CNTs and metal catalyst particles. In this section, aqueous H_2O_2 solution (30%) was used as an oxidant instead of H_2O. It was found that CNT stacks were also formed. Simultaneously, the aligned CNTs were in-situ modified with oxygen elements without any structure collapse. These as-grown m-CNTs were used as stabilizing substrates for silver and gold nanoparticle synthesis. The stabilizing effects of m-CNTs were compared with p-CNTs and PVP, one of the typical stabilizing agents for silver and gold nanoparticle synthesis.

5.1.2 Experimental

5.1.2.1 CNT synthesis

The detailed experimental procedures used to fabricate CNT stacks were described previously [12]. Chemical vapor deposition (CVD) was performed in a horizontal alumina tube (3.8 cm diameter; 92 cm long) housed in a Lindberg Blue furnace. The substrates were (001) silicon wafers coated with SiO_2 (500 nm) formed by thermal oxidation. The catalyst layers of Al_2O_3 (15 nm)/Fe (1 or 3 nm) were deposited onto the silicon wafer by sequential e-beam evaporation. CVD growth of CNTs was carried out with ethylene (150 sccm) as the carbon source, and hydrogen (200 sccm) and argon (350 sccm) as carrier gases. Instead of only bubbling water, in our current process, a trace amount of oxygen was introduced into the CVD chamber which was controlled by

bubbling a small amount of argon through aqueous H_2O_2 (30%). In all experiments, the water concentration in the furnace tube was maintained at 1000 ppm until the CVD process was terminated. The layered CNT films were obtained by the following method. Ethylene was first flowed into the CVD reactor for a preset time. After 5 mins aqueous H_2O_2, argon and hydrogen flow, ethylene was again introduced for a specific time. During the fixed 5 mins interval between CNT growth steps, water vapor (including trace amount of O_2) was used to selectively etch weakly bonded or amorphous carbon atoms existing at the interface between the nanotubes and catalyst particles. The CNTs synthesized by this process were referred as m-CNTs. Correspondingly, the CNTs without introduction of aqueous H_2O_2 were referred as p-CNTs.

5.1.2.2 Nanoparticle synthesis

In this section, nanoparticles were synthesized by two different methods. In the first method, silver nanoparticles were synthesized using 0.01 g silver nitrate as the precursor and 0.02 g resorcinol as the reducing agent in 15 ml ethanol in a small vial. 1.0 mg m-CNTs were added into the solution as the stabilizing substrates for the synthesized nanoparticles. Then, this mixture was sonicated for 2 hours in order to disperse the CNTs, as well as to stabilize silver nanoparticles after the precursors were reduced. In a control sample, the p-CNTs were added as the stabilizing substrates. The gold nanoparticles were synthesized from $HAuCl_4$ with a similar way as silver nanoparticles. The second method is polyol process. Silver nitrate (0.01 g) and m-CNTs (1.0 mg) were put into 15 ml ethylene glycol. The solution was sonicated for 2 hours. Ethylene glycol was used as both reducing agent and solvent. To compare the stabilization effects between m-CNTs and

PVP, 1.0 mg m-CNTs, 0.1 g PVP and 0.01 g silver nitrate were put into 15 ml ethylene glycol in a small vial. The solution was sonicated for 2 hours as well.

5.1.2.3 Characterization

Scanning electron microscopy (SEM) was used to characterize the morphologies of the as-synthesized CNTs. The SEM is JEOL 1530 equipped with a thermally assisted filed emission gun operating at 10 KeV. X-ray Photoelectron Spectroscopy (XPS) was performed using a Physical Electronics (PHI) Model 1600 XPS system equipped with a monochromator. The system used an Al Kα source (hν = 1486.8 eV). To study the modifications of CNTs, a fourier-transform infrared (FTIR) spectroscope was used (Nicolet, Magna IR 560). The m-CNTs were mixed with dried KBr and pressed to form the semi-transparent pellets. The FTIR spectrums were collected in the wavelength range from 400 to 4000 cm^{-1}. The morphologies of nanoparticles stabilized by CNTs were observed by the transmission electron microscopy (TEM, JEOL 100C). To prepare the samples, a few drops of the solutions after nanoparticles formation were placed onto the carbon coated TEM copper grid. The TEM analysis was performed at 400 KeV.

5.1.3 Results and Discussion

5.1.3.1 CNT synthesis and characterization

Figure 5.1.1 shows the SEM images of the as-synthesized m-CNT stacks. Seven-layered CNT stacks can be obtained by repeating the growth-etching cycle seven times, as shown in Figure 5.1.1 (a). Due to the high density of catalysts and Van der Waals force, the CNTs form a dense film with good alignment. No residue particles are observed on the CNT walls, as shown in the high magnification SEM image of m-CNTs (Figure 5.1.1

(b)). The surfaces of the CNTs are smooth, and the diameter of each tube is approximately 10nm.

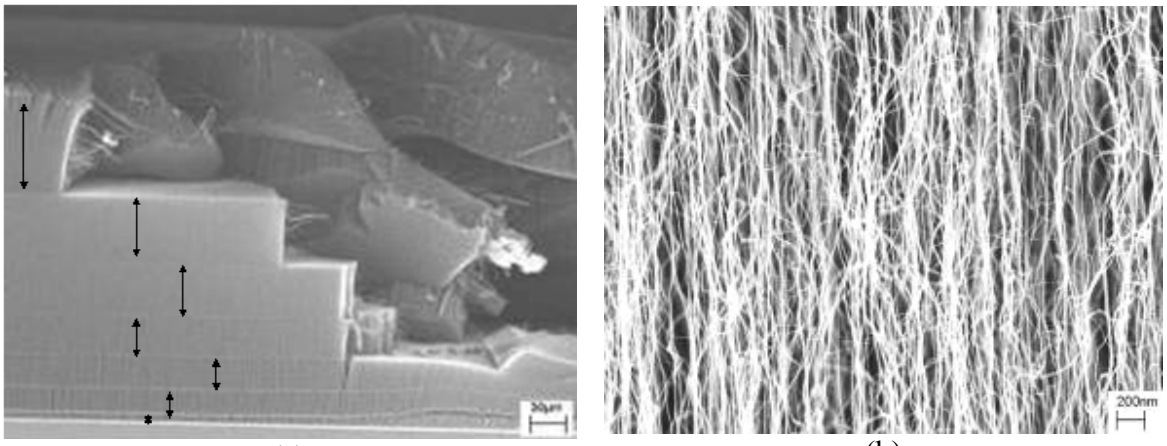

(a) (b)

Figure 5.1.1. (a) Scratched CNT film stacks to show the layered structures of CNT films; (b) high-magnification SEM image of CNTs film grown at 775 ºC.

XPS survey scans were carried out on the aligned m-CNT films, as shown in Figure 5.1.2, which clearly indicates the existence of the oxygen peak in addition to the detection of carbon. The binding energy of the O1s peak from the m-CNTs treated by H_2O_2 is around 529.6 eV, which means that the oxygen doesn't come from the dissociated H_2O, since the binding energy of O1s of H_2O is about 533 eV. The asymmetric C1s peak can be decomposed into six peaks. The main peak which can be assigned to the graphite signal is centered at 284.4 ± 0.2 eV. Another four peaks are centered at 285.2 ± 0.2, 286.3 ± 0.2, 287.3 ± 0.2, and 290.0 ± 0.2 eV, which correspond to sp^3 carbon atoms, hydroxyl, ether, carboxylic acid on the aromatic ring, respectively [139]. The last peak at 282.8 ± 0.2 eV might come from the C1s of SiC which was produced by the reaction of C_2H_4 and Si during the synthesis of CNTs [140]. The XPS results clearly show that the as-synthesized m-CNT walls were in-situ modified with oxygen functional groups. These oxygen sites on the walls can be used as nucleation centers for metal nanoparticle synthesis. On the contrary, no oxygen peaks can be found

from the XPS scan of p-CNTs (Figure 5.1.3). The C1s spectrum of the p-CNTs shows a symmetric peak at 284.5 ± 0.1 eV which corresponds to the graphite signal.

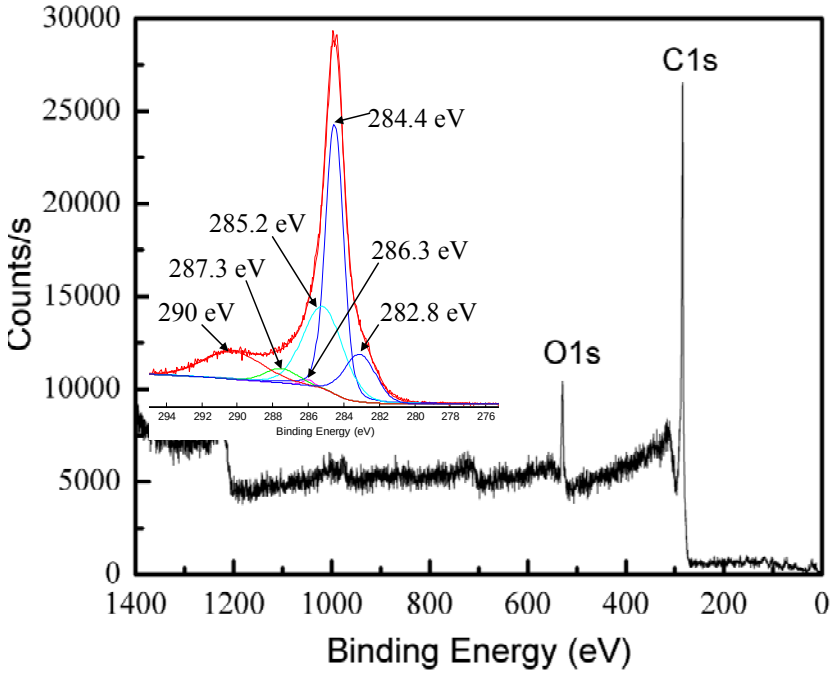

Figure 5.1.2. XPS survey scan of the m-CNTs. Inserted is the C1s spectrum of the m-CNTs which was decomposed into six peaks.

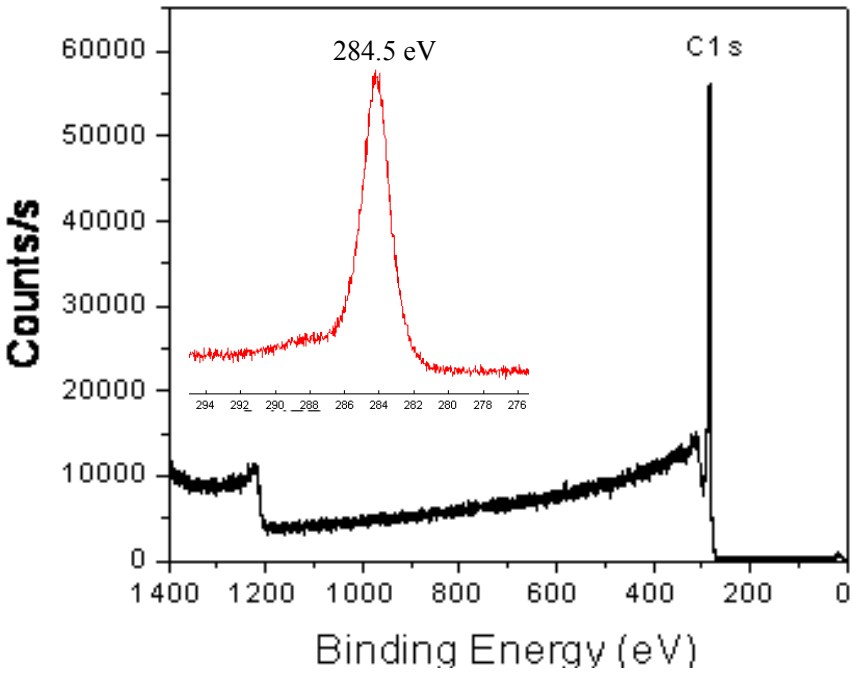

Figure 5.1.3. XPS survey scan of the p-CNTs. Inserted is the C1s spectrum of the p-CNTs.

The significance of the in-situ modification method is not only to simplify the modification process of CNTs, which is usually quite complicated and tedious for the post treatments, but also to maintain the original alignment of CNT arrays.

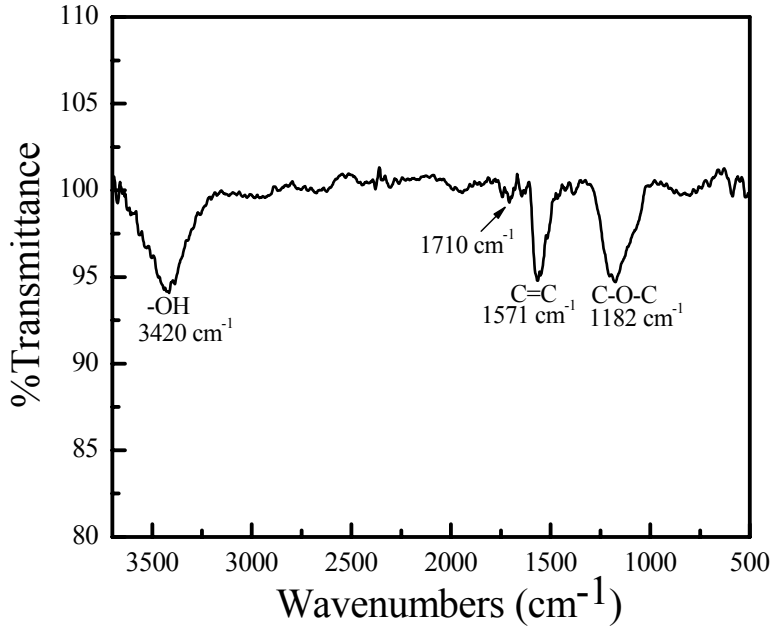

Figure 5.1.4. FTIR spectrum of the m-CNTs.

Figure 5.1.4 shows the IR spectra of the m-CNTs. The peak at 1571 cm^{-1} can be assigned to the C=C asymmetric stretching vibration of the graphene sheet. The IR spectrum also shows obvious O-H and C-O-C stretchings at 3420 cm^{-1} and 1182 cm^{-1}, respectively. Another peak with very weak intensity at 1710 cm^{-1} can be assigned to the –COOH stretch [141]. These functional groups make the m-CNTs amenable to the deposition of highly dispersed metal nanoparticles [142].

5.1.3.2 Nanoparticle synthesis

Figure 5.1.5 was the TEM image of silver nanoparticles which were synthesized by using 0.02 g resorcinol as reducing agents and without any stabilizing agents. The particles or agglomerations had quite a large size distribution, from 10 to 100 nm. This indicated that

the proper stabilizing agents or substrates were necessary in controlling the nanoparticle size, distribution and preventing nanoparticles from agglomeration.

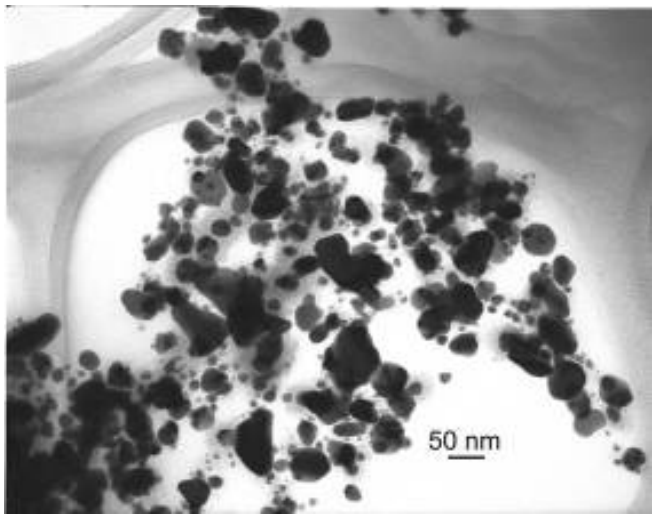

Figure 5.1.5. TEM image of silver nanoparticles synthesized by using 0.02 g resorcinol as reducing agents and without any stabilizing agents.

Figure 5.1.6 (a) showed the TEM image of silver nanoparticles which were synthesized by using 0.02 g resorcinol as reducing agents and 1.0 mg m-CNTs as stabilizing substrates. The silver particle size was less than 5 nm. It can be seen that almost all the silver nanoparticles grow along the axis of the CNTs. With the nanotubes acting as backbone, the nanoparticles were lined up to form a stable assembly. This indicated that there were active sites on the m-CNT walls which aided the nucleation and growth of silver nanoparticles on the surface. Figure 5.1.6 (b) was the TEM image of silver nanoparticles which were synthesized by using resorcinol as reducing agents and p-CNTs as stabilizing substrates. In this figure, the silver particles or agglomerations, larger than 50nm, randomly mixed with the CNTs without any order, indicating no stabilization effects of p-CNTs. Rao *et al.* also mentioned that depositions of metal clusters directly on

the surface of pristine CNTs were not quite successful but gave rise to considerable agglomeration of the clusters [143]. Therefore, the m-CNTs were much more effective stabilizing substrates for silver nanoparticle synthesis due to the oxygen elements on the m-CNT walls and prevented the synthesized nanoparticles from agglomeration.

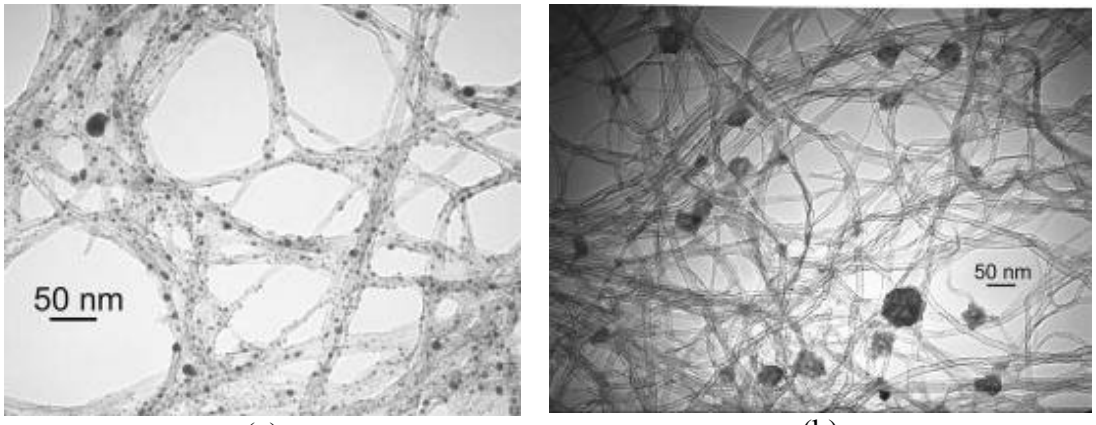

(a) (b)

Figure 5.1.6. TEM images of silver nanoparticles synthesized by using (a) m-CNTs and (b) p-CNTs as stabilizing substrates.

The stabilization effects of m-CNTs were also proved by the gold nanoparticle synthesis. Figure 5.1.7 (a) showed the TEM image of the gold particles which were synthesized by using m-CNTs as stabilizing substrates. The particles were all attached to the m-CNT walls and well dispersed. The sizes were all less than 5 nm. Nevertheless, with p-CNTs as stabilizing substrates, the gold nanoparticles were formed with large size-distribution, from 100 nm to 300 nm (Figure 5.1.7 (b)). These observations suggested that the m-CNTs could be used as good stabilizing substrates for gold nanoparticle synthesis. The gold nanoparticles can be well stabilized, and this is attributed to the unique structure of the m-CNTs which were modified during the CVD synthesis process.

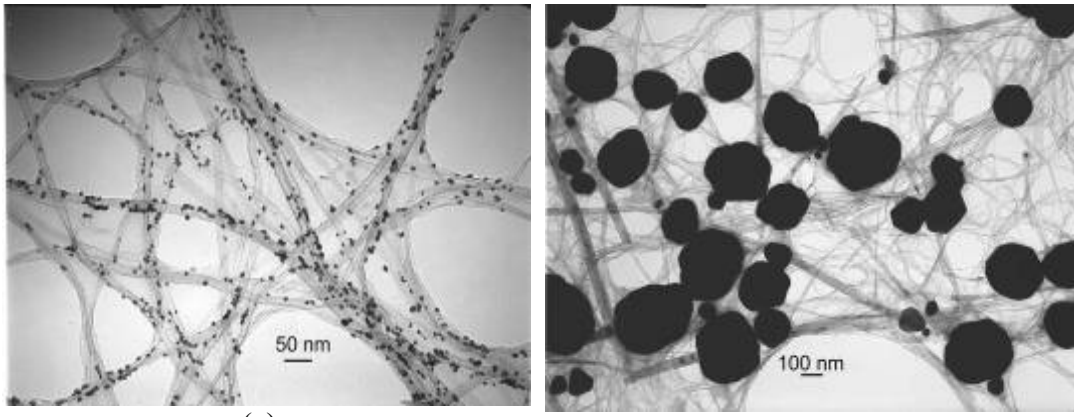

(a) (b)

Figure 5.1.7. TEM images of gold nanoparticles synthesized by using (a) m-CNTs and (b) p-CNTs as stabilizing substrates.

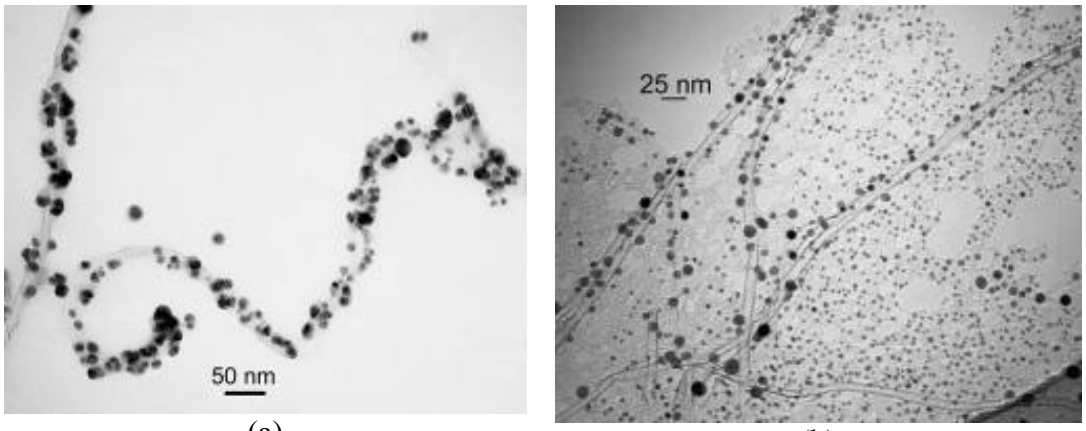

(a) (b)

Figure 5.1.8. TEM images of silver nanoparticles which were synthesized by using m-CNTs (a), PVP and m-CNTs (b) as stabilizing substrates.

In another experiment, 1.00 mg of the as-grown m-CNTs and 0.01 g silver nitrate were put in 15 ml ethylene glycol in two small vials with and without 0.1 g PVP, respectively. The two solutions were sonicated for 2 hours. Figure 5.1.8 (a) shows the TEM image of silver nanoparticles which were synthesized by using the as-grown m-CNTs as stabilizing substrates. It was found that almost all the particles were stabilized by the outside wall of the m-CNTs and the particle size was around 10-15 nm. This means that there are active sites on the outside wall of the as-grown m-CNTs which helps the nucleation of silver

nanoparticles on the surface. Compared with Figure 5.1.6 (a), the particle size by this method is around 5-10 nm larger. This is possibly due to the different reducing capability of resorcinol and ethylene glycol. Figure 5.1.8 (b) shows the TEM image of silver nanoparticles which were synthesized by using both PVP and m-CNTs as stabilizing substrates. The silver nanoparticles were either stabilized by the m-CNT walls or well dispersed by PVP with the size around 4-10 nm. PVP is one of the widely used stabilizing agents for silver nanoparticle synthesis [34,35,123], which stabilizes nanoparticles through multisite absorption of the polymer on the particle surface [143]. From Fig. 8 (a) and (b), it can be seen that both m-CNTs and PVP are very efficient stabilizing substrates or agents for silver nanoparticle synthesis in preventing the nanoparticles from agglomeration.

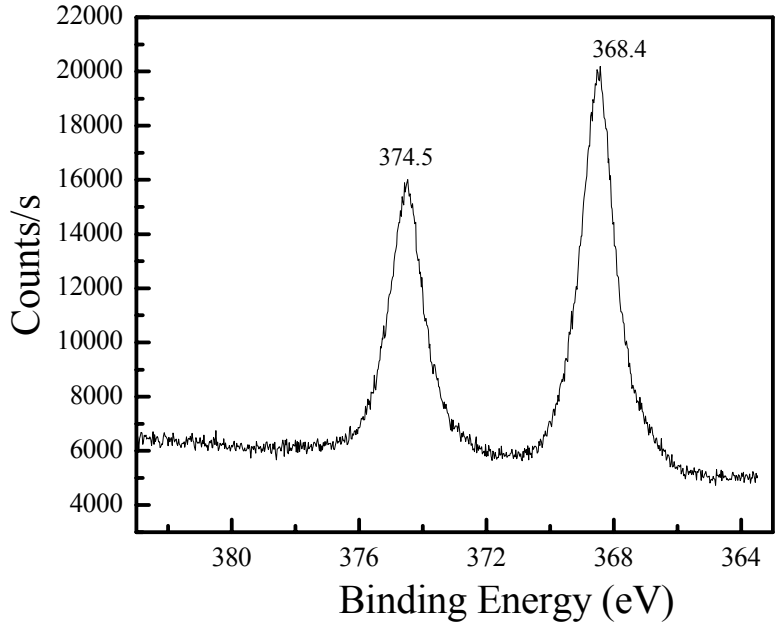

Figure 5.1.9. XPS spectrum of Ag3d from the as-prepared m-CNTs stabilized Ag nanoparticles in Figure 5.1.8(a).

The XPS spectrum of Ag3d from the as-prepared m-CNTs stabilized Ag nanoparticles in Figure 5.1.8(a) is shown in Figure 5.1.9. Two peaks with binding energies of 368.4 and 374.5 eV correspond to Ag $3d_{5/2}$ and Ag $3d_{3/2}$, respectively. These are typical values for Ag^0 [144], indicating the formation of Ag nanoparticles on the sidewalls of the m-CNTs [145]. No additional peak beyond the Ag3d doublet is observed, which means that no chemical reaction between the Ag nanoparticles and m-CNTs can be claimed [146].

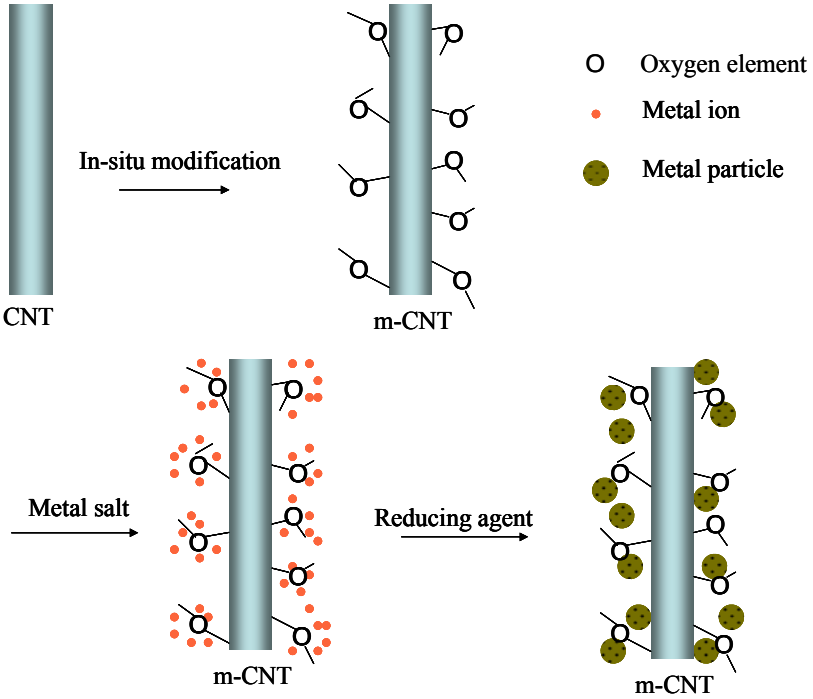

Figure 5.1.10. Proposed mechanisms of m-CNTs as stabilizing substrates for metal nanoparticle synthesis.

From the above analysis, it is evident that the m-CNTs were considerably effective in stabilizing silver and gold nanoparticles in preventing the nanoparticles from agglomeration. The stabilizing effects of the m-CNTs were proposed as the followings: The oxygen elements on the m-CNT walls provided the nucleation centers for metal ion and then stabilized the nanoparticles after they were formed. The m-CNTs act as the

template on which the as-formed nanoparticles can line up to form a stable assembly due to their special structures (Figure 5.1.10).

5.1.4 Summary

CNTs were first surface-modified by weak oxidant during the CVD synthesis process. FTIR showed that there were C-OH and C-O-C functional groups on the m-CNT walls. These as-grown m-CNTs without any post-treatments can be used as excellent stabilizing substrates for silver and gold nanoparticle synthesis. The stabilizing effects of the m-CNTs were compared with p-CNTs and PVP. The silver and gold nanoparticles synthesized by using m-CNTs as stabilizing substrates can be achieved as low as 5 nm and are monodispersed. However, the p-CNTs could not be used as stabilizing substrates for metal nanoparticle synthesis, resulting in agglomerations and large size distribution. On the other hand, the fact that silver and gold nanoparticles can be well stabilized by m-CNTs further confirmed that there are active sites on the m-CNT walls, which is attributed to the surface modification of CNTs during production.

5.2 Carbon Nanotube Film Transfer via Conductive Adhesives

5.2.1 Introduction

As we discussed in Chapter 1.4, some technical issues hurdle the full utilization of the CNTs in microelectronic and photonic manufacturing, which include high processing temperature and poor adhesion: First, the typical CVD is done at 700–900 °C, at which many substances of the electronic or photonic devices cannot withstand. Second, the adhesion between the silicon substrate and CNTs is very poor and the low adhesion

strength limits the application of CNTs as interconnect materials in the microelectronic packaging due to high contact resistance and the long term reliability issue. Consequently, a novel CNT transfer technology is needed, rather than growing CNTs directly on the devices.

A CNT transfer technology was first proposed by which an open-ended CNT film was transferred to a copper surface via eutectic tin/lead (Sn/Pb) solder [16]. The hollow cavity of the open-ended CNTs will allow the wicking of solder due to the capillary force after the solder melt. This process could overcome the serious obstacles of integration of CNTs into integrated circuits and microelectronic device packages by offering low processing temperatures and improved adhesion of CNTs to substrates. The transferred CNTs can be used to simultaneously form electrical and mechanical connections between chips and substrates. However, the solder has technical barriers as CNT transfer medium, such as limited options of substrate surfaces for wetting, adhering and low flexibility in design.

Silver pastes [17] and 70 nm thickness of gold layer [18] were also used to transfer the CNT bundles or films to conductive substrates. However, the process temperatures used are 530 °C and 800 °C, respectively, which are too high to be compatible with microelectronic processes.

Recently, we have demonstrated an ultra highly conductive polymer composite for the lead-free interconnect application, which was composed of nano sized Ag particles, micron sized Ag flakes and an epoxy resin [147]. The resistivity of this composite material could be achieved as low as 5×10^{-6} Ω.cm, which was even lower than that of eutectic Sn/Pb solder (2×10^{-5} Ω.cm). In this section, this ultra highly conductive polymer composite was used as a transfer medium instead of Sn/Pb, which transfers the

aligned CNT films to a copper surface. This process can take the advantage of polymers, such as low temperature, high compatibility on substrates and flexible design, etc. The morphologies of the joint structures were investigated and the electrical properties of CNT films transferred via the conductive polymer composites were studied.

5.2.2 Experimental

5.2.2.1 Synthesis of aligned CNT films

The CVD was performed in a horizontal alumina tube (3.8 cm diameter; 92 cm long) housed in a Lindberg Blue furnace. The substrates were (001) silicon wafers coated with SiO_2 (500nm) formed by thermal oxidation. The catalyst layers of Al_2O_3 (15nm)/Fe (1 or 3nm) were deposited onto the silicon wafer by sequential e-beam evaporation. CVD growth of CNTs was carried out with ethylene (150 sccm) as the carbon source, hydrogen (200 sccm) and argon (350 sccm) as carrier gases. The water vapor concentration in the CVD chamber was controlled by bubbling a small amount of argon gas through water held at 22 °C. In all experiments, the water concentration in the furnace tube was maintained at 1000 ppm until the CVD process was terminated.

5.2.2.2 Preparation of conductive polymer composites

The Ag nanoparticles with an average diameter of 20 nm were first surface functionalized with surfactants [13]. The as-prepared surface functionalized silver nanoparticles and micron sized silver flakes (6:4) were incorporated into a mixture of bisphenol A and hexahydro-4-methylphthalic anhydride (weight ratio: 1:0.75) to form the polymer composite. The composite was then soniacted for one hour to disperse the fillers in the epoxy resin. Thereafter, an imidazole type catalyst (0.5% weight to the polymers) was

incorporated and the mixture was sonicated again for 5 mins. The resistivity of the as-prepared highly conductive polymer composite in this section is 3.1×10^{-5} Ω.cm. As a reference, a high resistance formulation was created by dispersing 50 wt% Ag nanoparticles without any surface functionalization into the epoxy resin, the resistivity of which was 58.6 Ω.cm.

5.2.2.3 Characterizations

Scanning electron microscopy (SEM) was used to characterize the morphologies of the as-synthesized CNTs and the conductive polymer composite transferred ones. The SEM is JEOL 1530 equipped with a thermally assisted field emission gun operating at 10 KeV. To measure the electrical performance of CNT film transferred by the conductive polymer composites, the copper top electrodes were deposited on the surface of CNT film with a diameter of 2.1 mm. This test coupon was measured by a four probe method. A Keithley 2000 multimeter equipped with probe station was used to measure the current-voltage response of CNT film by contacting with the bottom and top electrodes.

5.2.3 Results and Discussion

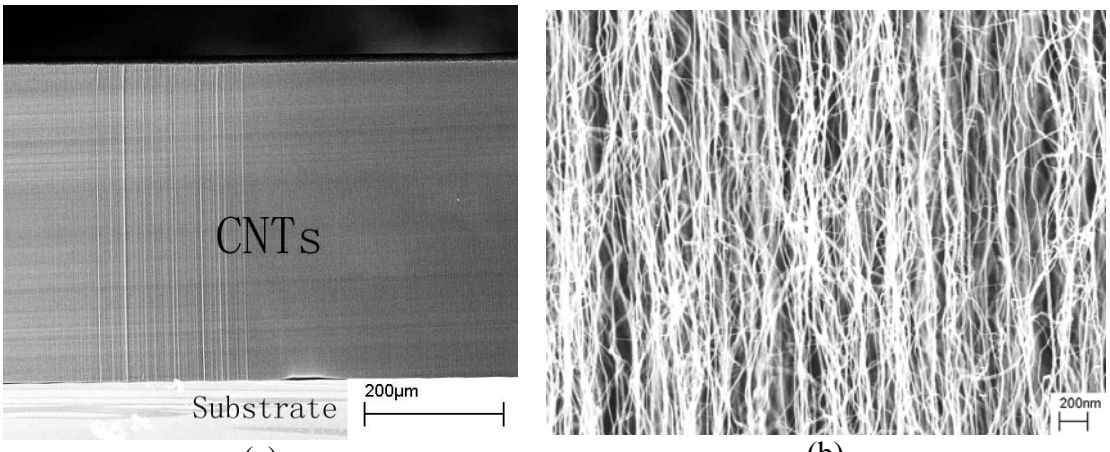

(a) (b)

Figure 5.2.1. SEM images of (a) CNT films grown at temperatures of 750 ºC, (b) high magnification SEM image of CNT film in (a).

Figure 5.2.1 showed the SEM images of the as-synthesized aligned CNT film. Due to the high density of the catalyst layer, the CNTs formed a dense film with good alignment. No other residual particles were observed on the CNT walls, as shown in the high magnification SEM image of CNTs (Figure 1 (b)). The surfaces of the CNTs were smooth, and the diameter of each tube was approximately 10 nm.

The substrate was a flame retardant level-4 (FR-4) board coated by copper foil. The conductive polymer composite was stencil-printed on the FR-4 board. The silicon substrate with a CNT film was flipped over and pressed down to the composites with a certain pressure by hands. The polymer composite was cured at 150 °C for one and a half hours. Thereafter, the silicon substrate was removed (Figure 5.2.2). Thus, the CNT film can form the electrical and mechanical connections onto the copper surface by the conductive polymer composite. This process enables CNTs to be transferred and implemented into integrated circuits and microelectronic device packages at low temperature (150 °C) and with improved adhesion of CNT films or arrays to the substrates.

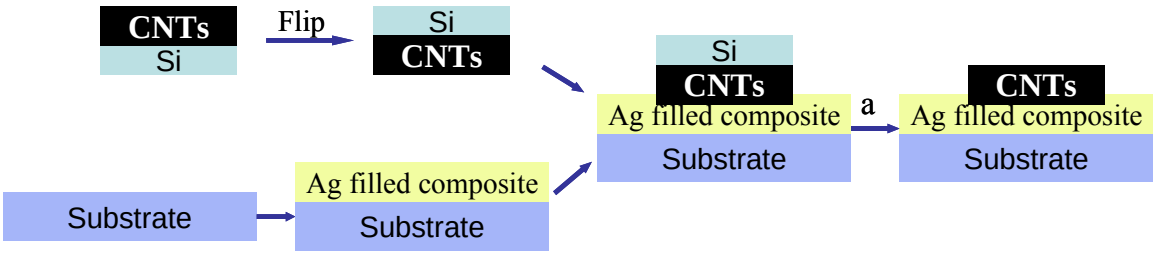

a: Cure the polymer composite and remove Si.

Figure 5.2.2. Schematic diagram of CNT films transferred via conductive polymer composites.

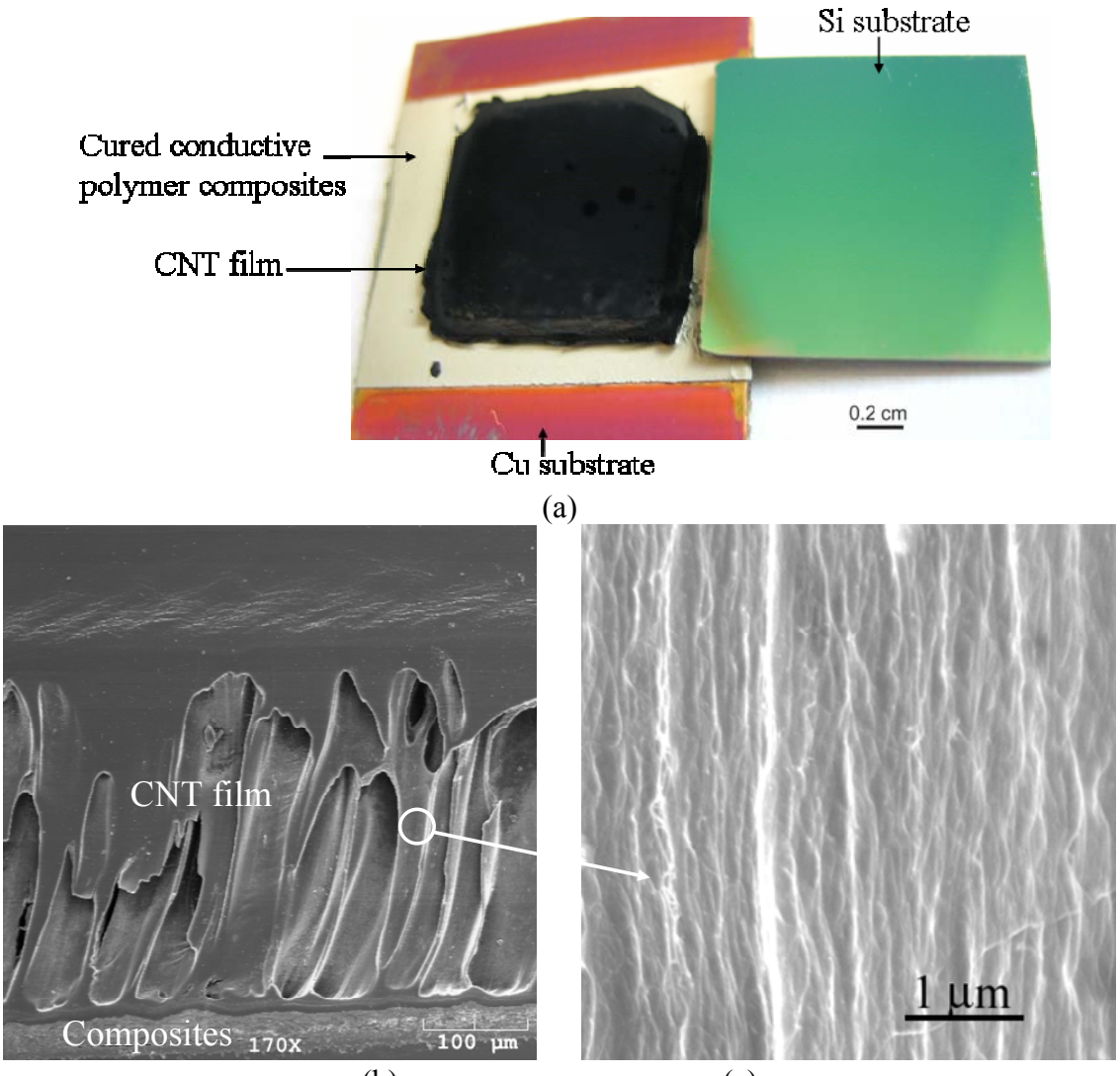

Figure 5.2.3. (a) Photograph of a CNT film transferred onto the copper surface via conductive polymer composites. (b) A cross-sectional SEM image of the well aligned CNT film transferred by polymer composites. (c) The higher magnification image of CNT film after the transfer process.

Figure 5.2.3 (a) shows a CNT film transferred onto a Cu-clad FR-4 substrate via a conductive polymer composite. This figure indicates that the entire CNT film was successfully transferred onto the substrate because no trace amount of CNTs was observed on the silicon substrate. A cross-sectional SEM image (Figure 5.2.3 (b)) clearly shows that the aligned CNT film was bonded to the polymer composites. CNTs in the

form of bundles were observed after curing due to the polymer wetting along the CNT surfaces by capillary force in/between tubes. In the higher magnification SEM image (Figure 5.2.3 (c)), it can be observed that the nanotubes inside the bundles still maintain their original aligned structures.

For the electrical measurement of CNT films, the Cu surface of the substrate was used as bottom electrode and Cu top electrodes with a 2.1 mm diameter were created onto the end surface of CNTs by DC-sputter after the transfer process, where four Pt coated probes with tip sizes around 6 μm were used for the four-probe measurement. The configuration of the four-probe experiment was shown in Figure 5.2.4. The resistance between two electrodes can be directly obtained from the applied current and the measured voltage.

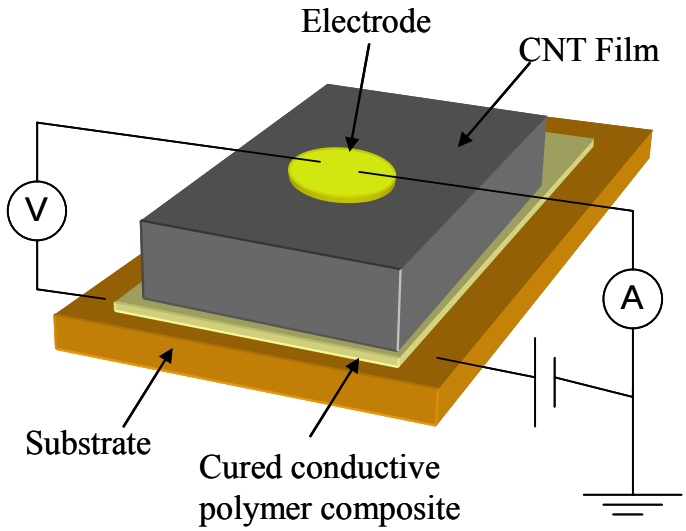

Figure 5.2.4. Schematic of the setup for the I-V curve measurement.

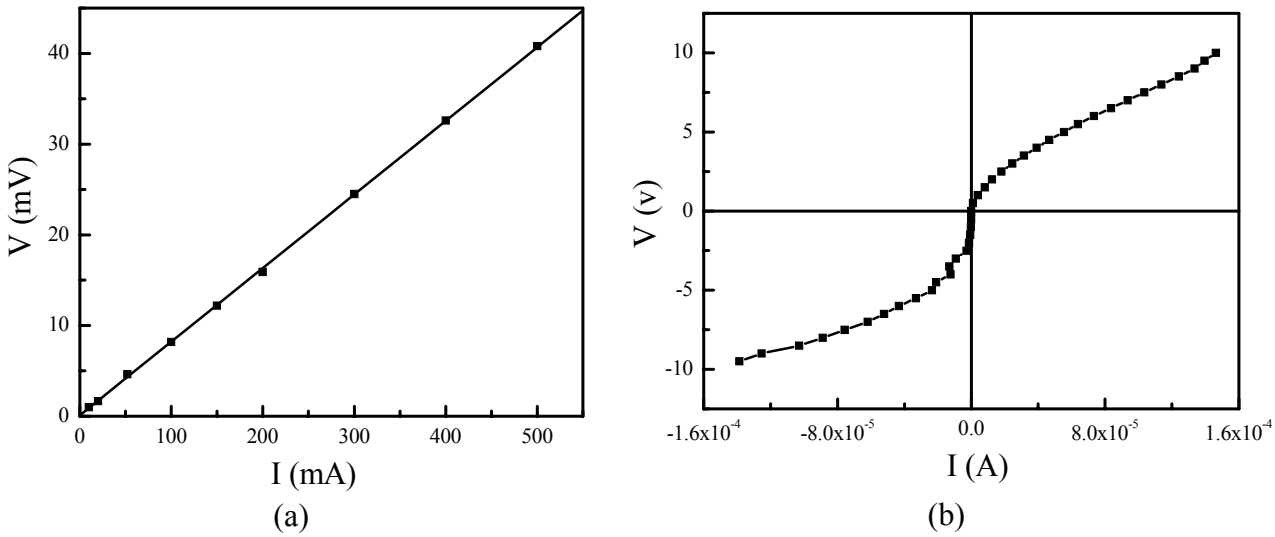

Figure 5.2.5. I-V curve of (a) the ultra highly and (b) the very low conductive polymer composite transferred CNT films.

The I-V characteristics of the as-transferred CNT film (~790 μm in length) via an ultra highly conductive polymer composite (~60 μm in thickness) were shown in Figure 5.2.5 (a). A linear relationship between current and voltage was obtained, which indicated that an ohmic contact was formed between the CNT film and the highly conductive polymer composite. The resistance of the resulting CNT films, R_{CNTs}, from the four-probe measurement was 0.08 Ω. Thus, the resistivity of the transferred CNT film based on the area of the top electrodes and the height of the CNT film was ~3.5×10^{-4} Ω.m. A relatively high resistivity polymer composite (ρ = 58.6 Ω.cm) was also used to transfer the CNT films to copper surface. Figure 5.2.5 (b) shows the I-V characteristics of the CNT film transferred by the high resistivity polymer composite, where a nonlinear I-V behavior was observed which can be typically found at non-ohmic contacts such as a joint between a semiconductor and a metal connection. Therefore, the electrical properties of the whole device can be altered by the delivery medium (polymer

composites). Ohmic or non-ohmic joints can be easily formed by just changing the resistivity of the polymer composites.

5.2.4 Summary

The CNT films were successfully transferred to the copper surface via conductive polymer composites at a low temperature, 150 °C. The CNT films formed bundles due to the polymer wetting along the tubes by capillary force in/between tubes. The nanotubes inside the bundles still maintained the aligned structures. An ohmic contact can be formed between a CNT film and a highly conductive polymer composite. The resistance of the as-transferred CNT film was 0.08 Ω. The significance of the transfer method in this section is not only to provide a low temperature CNT transfer technique, but also a highly conductive CNT film or array for lead-free interconnect applications. At the same time, the polymer materials can provide a flexible design and easily wet on many surfaces, which enables the feasibility of transferring CNTs to different kinds of substrates.

CHAPTER VI

SUMMARY AND FUTURE WORK

6.1 Summary

This thesis is devoted to the research and development of low processing temperature lead-free interconnect materials for microelectronic packaging applications with an emphasis on fundamental studies of nanoparticles synthesis, dispersion and oxidation prevention, and nanocomposites fabrication.

6.1.1 Nano lead-free solder pastes

Sn, SnAg and SnAgCu alloy nanoparticles with different sizes were successfully synthesized by a low temperature chemical reduction method. An organic surfactant was used not only for the dispersion of the nanoparticles, but also cover on the particle surfaces to prevent them from oxidation. HRTEM image clearly showed the particles had a core-shell structure, namely metallic core and amorphous surfactant shell (Figure 2.4.2). Differential Scanning Calorimeter studies showed that both the size dependent melting point and latent heat of fusion of the synthesized nanoparticles were obtained. The SnAg or SnAgCu alloy nanoparticles were dispersed into an acidic type flux to make the nano lead-free solder pastes. Their wetting properties on cleaned copper surfaces were studied. The nano solder pastes spread and wet on the Cu surface and the intermetallic compound (Cu_6Sn_5) was formed after the reflow process. This study demonstrated the viability of the SnAg or SnAgCu alloy nanoparticles pastes as a

candidate for the low processing temperature lead-free interconnect applications in microelectronic packaging.

6.1.2 Highly conductive ECAs

Figure 1.5.2 and 4.2.1 showed that too many contact interfaces between fillers resulted in a lower electrical conductivity of the isotropic conductive adhesives (ICAs). Therefore, an ultra highly conductive ICA could be obtained by making the Ag nanoparticles sintering together to reduce the contact interface between fillers.

Surface functionalized silver nanoparticles and silver fakes were used as fillers for electrically conductive adhesives (ECAs) applications. During the curing of epoxy resin (150 ^{o}C), the surfactants were debonded from the particles and at the same time the oxide layers on the particle surfaces were removed which facilitated the sintering of Ag nanoparticles. The contact interfaces between fillers were significantly reduced and an ultra highly conductive ECA with a resistivity of 5×10^{-6} Ω.cm was obtained (Figure 4.2.5 and 4.2.7).

A high performance non conductive adhesive/film (NCA/NCF) was also successfully created by dispersing a small amount of surface functionalized carbon nanotubes (CNTs). CNTs have many excellent properties, such as extremely high thermal conductivity, excellent electrical and mechanical properties and also a lower CTE values. The small amounts of CNTs (0.03 wt%) in the NCAs/NCFs lowered down the CTE value by 11 ppm/^{o}C. This significant CTE reduction resulted in a higher thermal mechanical reliability of the device. At the same time, the current carrying capability was increased from 3.7 A to 4.2 A, an enhancement of 14 %, which is due to the high thermal conductivity of the CNTs and the generated heat can be dissipated out more efficiently.

6.1.3 Transferred CNT films/bundles

Carbon nanotubes are proposed as the interconnect materials in microelectronic packaging due to their excellent thermal, electrical and mechanical properties. However, due to the high processing temperature and poor adhesion of CNTs to substrates, the full utilization of CNTs as interconnect materials in microelectronic packaging is limited. To enhance the adhesion of CNT films to substrates, an ultra highly conductive ECA were used as a media to transfer the CNT films to copper substrates. The polymer wetted along the CNTs during curing process by the capillary force. An ohmic contact was formed between the copper substrates and the transferred CNTs. This process could overcome the serious obstacles of integration of CNTs into integrated circuits and microelectronic device packages by offering low processing temperatures and improved adhesion of CNTs to substrates. The transferred CNTs can be used to simultaneously form electrical and mechanical connections between chips and substrates.

On the whole, a low melting temperature SnAg or SnAgCu alloy nanoparticles pastes, an ultra highly conductive adhesives and CNT films or bundles with an improved adhesion to substrates have been successfully prepared for low processing temperature lead-free interconnect applications in this thesis.

6.2 Future Work

6.2.1 Prevention the oxidation of Sn, SnAg, SnAgCu alloy nanoparticles by studying the 1,10-phenanthroline with different side chain length effects

Effective capping capability can reduce or eliminate agglomeration of nanoparticles as well as protect them from oxidation. We have found that 1,10-phenanthroline (Figure

6.2.1 (a)) was an effective capping agent in forming crystalline SnAg or SnAgCu alloy nanoparticles. When the SnAg alloy nanoparticles were formed, they were instantly coordinated to 1,10-phenanthroline through the pair of chelating nitrogen donor sites adjoining the two heterocylic aromatic rings. The HRTEM characterizations (Figure 2.4.2) showed that the particles were covered by capping agents and the capping agents could provide an effective barrier against the penetration of atmospheric oxygen to the nanoparticles. However, more extensive studies on interactions between environments, precursors, reducing agents, additives and capping agents are needed.

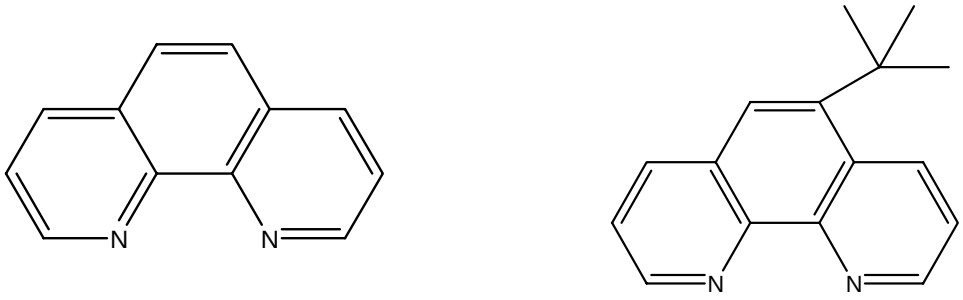

(a) 1,10-phenanthroline

(b) 1,10-phenanthroline with electron donating side groups

Figure 6.2.1. Chemical structures of the capping agents.

By using 1,10-phenanthroline as capping agents, the particle size could only be decreased to around 10 nm (average diameter) without obvious oxidation. When the particle size was further decreased (less than 10 nm), oxidation occurred. Therefore stronger coordinating capping agents are necessary to anchor on the particle surface and prevent the particles from oxidation when the particle size is further reduced. Our target is to obtain SnAg or SnAgCu alloy nanoparticles with a melting point close to that of eutectic SnPb (183 °C). For such a lower melting temperature, the particle diameters need to be decreased to around 5-7 nm according to our group's simulation results. As thus, we need

to use the chemicals of 1,10-phenanthroline with strong electron donating side groups (Figure 6.2.1 (b)). Hence, the 1,10-phenanthroline will have stronger coordination towards the particle surface and will give a better protection of the nanoparticles from oxidation.

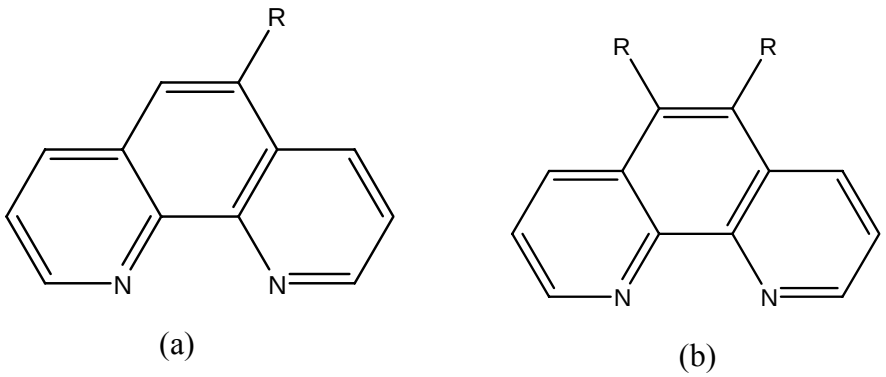

Figure 6.2.2. The chemical structures of the proposed capping agents for preventing oxidation of nanoparticles (R represents different length of side chains).

Whitesides [148] and Rieley [149] have found that the self-assembled monolayers (SAMs) could prevent the oxidation of copper and gold by providing an effective barrier against the penetration of oxygen to the substrates, respectively. The longer chain length of SAMs could decrease the oxidation rates of the substrates. Therefore, the use of 1,10-phenanthroline with longer hydrophobic side chains (Figure 6.2.2 (a) and (b)) for preventing the oxidation of Sn alloy nanoparticles and the absorption of moisture might be more effective. The effects of different chain lengths and number of side chains for preventing oxygen diffusion and moisture absorption need to be studied.

The dendritic polymer will be studied as the capping agents/surfactants too, in order to capture the metal alloys, to restrict the size growth of the alloy particles and to prevent the particles from oxidation. Dendrimers are monodispersed macromolecules built with

the highest level of synthetic control. The dendritic architecture consists of connectors and branching units built around a small molecule or linear polymer (core). This type of architecture leads to spherical dendrimers or rod-like macromolecules, respectively. The interior and exterior of a dendritic polymer can be very different, depending on the chemistry of terminal groups. Either the interior or the exterior can be hydrophilic (cationic, anionic, neutral) or hydrophobic. Commercially available dendrimers such as ethylenediamine core poly (aminoamine) (PAMAM) can be used. Various surfaces and generational combinations, for example, amino and carboxylate surfaces generation 3.5, 4 or 5, need to be studied. These combinations will offer cationic and strong electron donor, NH_2, polar and weak proton donor $-C(CH_2OH)_3$ groups, as well as anionic carboxylate terminal groups and apolar aliphatic surfaces with a comparable number of internal and external nitrogen ligands.

In order to accomplish the goal of protecting smaller size (less than 10 nm) SnAg or SnAgCu alloy nanoparticles from oxidation, the following issues need to be investigated:

1.) Study the capping effects of 1,10-phenanthroline with different side chain length of electron donating groups on SnAg or SnAgCu alloy nanoparticles and their effects on protecting the nanoparticles from oxidation.

2.) Study the capping, dispersing, and preventing oxidation effects of dendrimers (such as PAMAM) on SnAg or SnAgCu alloy nanoparticles.

6.2.2. Rare Earth Elements Improving Wetting of Lead-free Solders

6.2.2.1 Background information

Wetting is the behavior of a liquid towards a solid surface with a contact. In order to attain successful soldering, a certain degree of wetting of molten solder on the solid substrate surface is required. A proper metallurgical bond must be formed at the interface between the solder and the substrate, which means an interfacial reaction takes place to form a certain amount of intermetallic layer at the interface. These intermetallics act as an adhesion layer to join the solder and substrate together.

The solderability of the SnPb alloy is good on general metallic substrates. When changing from SnPb to lead-free alloys, the solderability can be a concern. There are two common ways to characterize the wetting properties of solders, namely spread area test and wetting balance test.

In a spread test, the ability of the molten solder to spread over the substrate is used to measure the wetting behavior. The increase in contact area or the ratio of the as-bonded contact area to the original contact area indicates the wetting behavior of solder. The extent of wetting of solders on substrates is measured by the contact angle.

$$\gamma_{SF} = \gamma_{SL} + \gamma_{LF}\cos\theta_c \quad (6.2.1)$$

$$\cos\theta_c = (\gamma_{SF} - \gamma_{SL})/\gamma_{LF} \quad (6.2.2)$$

Where γ_{SF}, γ_{SL} and γ_{LF} are the surface tensions of the substrate/flux, substrate/liquid solder interfaces and liquid solder/flux, respectively. When good wetting occurs, the contact angle should be smaller.

In the wetting balance test, molten solders climb up the coupon due to the wetting force exerted on it. A typical wetting curve is shown in Figure 6.2.3. The wetting time, t_w, is the time at which the solder contact angle to the coupon is 90^o (point B). The shorter wetting time is considered to be better.

In order to improve the wetting ability of lead-free alloys, the wetting behaviors of Sn/37Pb solder and Pb-free solders with or without rare earth elements addition were studied by using the wetting balance method [150-152]. The wetting curves of SnAg, SnAg-0.25RE and SnAg-0.5RE are compared with SnPb in Figure 6.2.4. It can be seen that all the alloys have roughly the same wetting time. However, the wetting force of the SnPb is the highest. The effect of adding certain amount of rare earth elements (mainly La and Ce) was shown in Figure 6.2.4, in which the wetting force achieved by SnAg-0.25 RE was very close to that of SnPb. However, SnAg-0.5Re showed the lowest wetting force which was due to the oxidation of the excessive amount of rare earth elements.

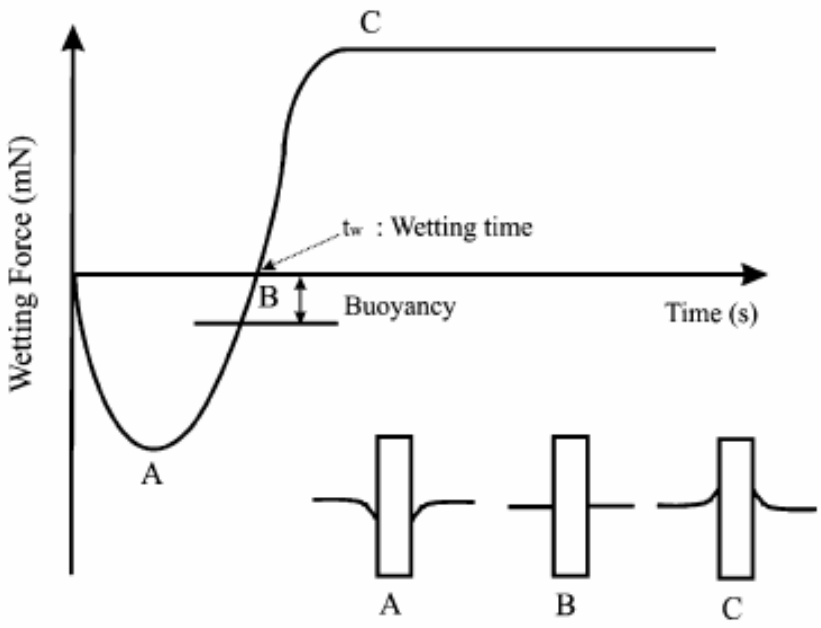

Figure 6.2.3 The variation of wetting force with time.

The SnAgCu alloy also has similar wetting improvement with 0.1 wt% of rare earth elements addition as shown in Figure 6.2.5.

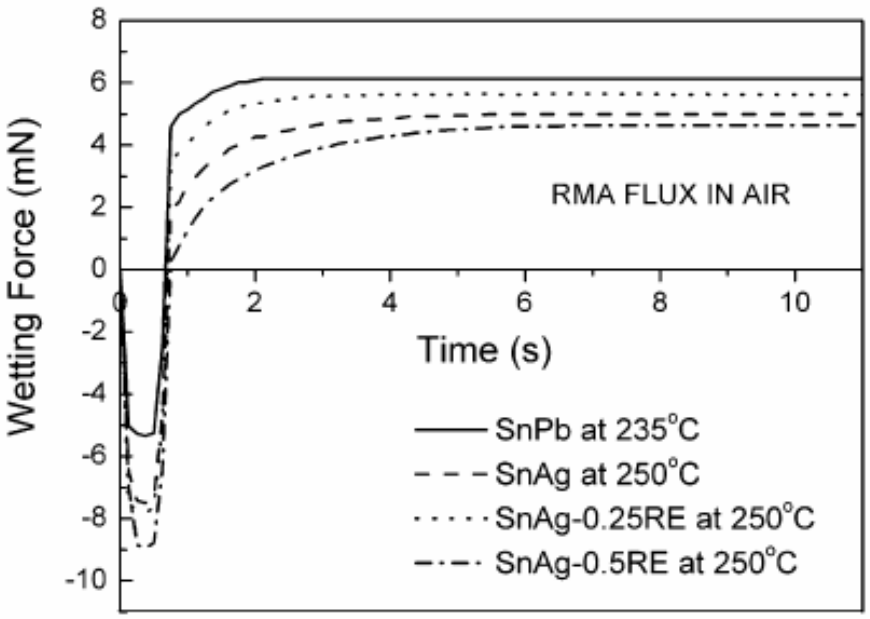

Figure 6.2.4 The wetting curves of SnAg-RE solders compared with SnPb.

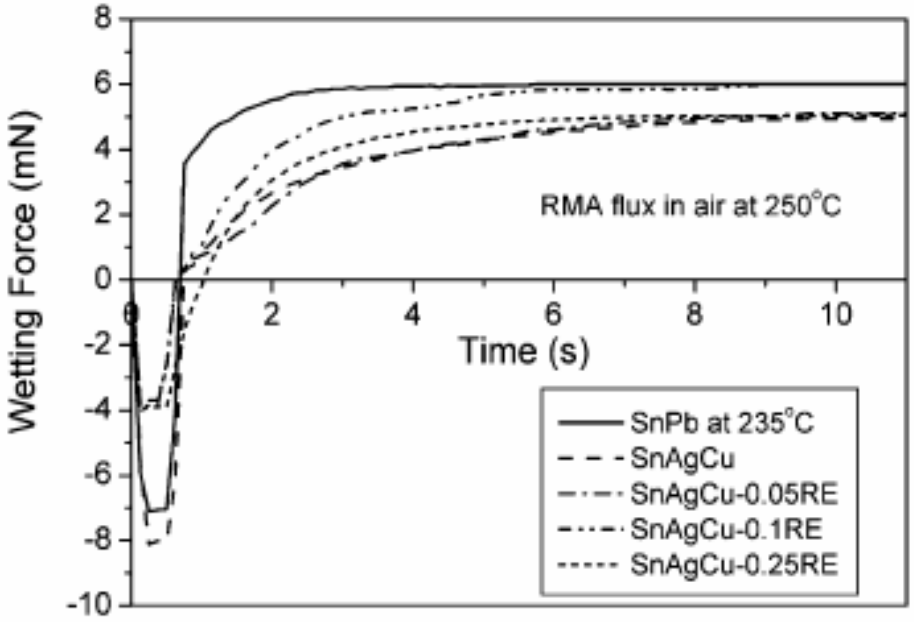

Figure 6.2.5 The wetting curves of SnAgCu-RE solders compared with SnPb.

The enhancement of the wetting force by adding a small amount of rare earth elements is due to the effects of rare earth elements on the interfacial tensions, $\gamma_{SF,}$ $\gamma_{SL,}$ and γ_{LF}. The rare earth elements are easier to accumulate at the solder/flux interface in the molten state due to their high activity, and the interfacial surface tension, $\gamma_{LF,}$ is then decreased [153]. From equation 6.2.2, the reduction of γ_{LF} results in a smaller contact angle, which is a better wetting quality.

6.2.2.2 Future work on rare earth element nanoparticles synthesis

In order to improve the wetting properties of our nano lead-free solders to the copper substrates, we propose to add a certain amount of rare earth elements nanoparticles to the synthesized SnAg or SnAgCu alloy nanoparticles. The small amount of rare earth elements will enhance the wetting force of the molten solders. In order to accomplish this goal, the following issues need to be investigated:

1.) Synthesis and characterization of rare earth element (La, Ce, etc.) nanoparticles

The synthesis of rare earth element nanoparticles or their alloys are still challenging due to their low chemical potential. The selection of the precursors, reducing agents and reduction methods are very important.

2.) Prevention oxidation of rare earth element nanoparticles

Rare earth elements are active and easily oxidized. Nano sized particles, due to their high surface area to volume ratio, are more easily oxidized. Therefore, proper capping agents/surfactants are necessary to cover on the particle surfaces and prevent them from oxidization.

APPENDIX A

AUTHOR'S AWARDS AND PUBLICATIONS

A.1 Awards

[1] Chinese Government Award for Outstanding Self-Financed Students Abroad, 2007.

[2] Finalist for the 15th Motorola-IEEE/CMPT Fellowship at 57th Electronic Component & Technology Conference, 2007.

[3] Initiation Publication Award, School of Materials Science and Engineering, Georgia Institute of Technology (2006)

A.2 Journal Publications

[1] **H. Jiang**, K. Moon, Y. Sun, C. P. Wong, F. Hua, T. Pal, A. Pal, "Tin/indium nanobundle formation from aggregation or growth of nanoparticles", Journal of Naonoparticle Research 10(1): 41-46 (2008)

[2] **H. Jiang**, K. Moon, F. Hua, C. P. Wong, "Synthesis, thermal and wetting properties of tin/silver alloy nanoparticles for low melting point lead-free solders", Chemistry of Materials 19(18): 4482-4485 (2007)

[3] **H. Jiang**, L. Zhu, K. Moon, C. P. Wong, "Low temperature carbon nanotube film transfer via conductive polymer composites", Nanotechnology 18(12): Art. No. 125203 (2007)

[4] **H. Jiang**, L. Zhu, K. Moon, C. P. Wong, "The preparation of stable metal nanoparticles on carbon nanotubes whose surface were modified during production", Carbon 45(3): 655-661 (2007)

[5] **H. Jiang**, K. Moon, Y. Li, C. P. Wong, "Surface Functionalized Silver Nanoparticles for Ultra-Highly Conductive Polymer Composites", Chemistry of Materials 18(13): 2969-2973 (2006)

[6] **H. Jiang**, K. Moon, H. Dong, F. Hua, C. P. Wong, "Size-dependent melting properties of tin nanoparticles", Chemical Physics Letters 429(4-6): 492-496 (2006)

[7] **H. Jiang**, K. Moon, Z. Zhang, S. Pothukuchi, C. P. Wong, "Variable Frequency Microwave Synthesis of Silver Nanoparticles", Journal of Nanoparticle Research 8(1): 117-124 (2006)

[8] **H. Jiang**, K. Moon, J. Lu, and C. P. Wong, "Conductivity Enhancement of Nano Ag Filled Conductive Adhesives by Particle Surface Functionalization", Journal of Electronic Materials 34(11): 1432-1439 (2005)

[9] **H. Jiang**, K. Moon, and C. P. Wong, "Tin/silver/copper alloy nanoparticles for low temperature solder pastes interconnect", submitted to Journal of Electrochemical Society

[10] **H. Jiang**, M. Yim, K. Moon, W. Lin, and C. P. Wong, "Novel nonconductive adhesives/films with carbon nanotubes for high performance interconnect", submitted to Journal of Electronic Materials

[11] Y. Sun, **H. Jiang**, L. Zhu, C. P. Wong, "A novel nanocomposites with photo-polymerization for wafer level application" IEEE transactions on components and packaging technologies (in press)

[12] H. Dong, A. Meininger, **H. Jiang**, K. Moon, C. P. Wong, "Magnetic nanocomposite for potential ultrahigh frequency microelectronic application", Journal of Electronic Materials 36(5): 593-597 (2007)

[13] L. Zhu, J. Xu, F. Xiao, **H. Jiang**, D. Hess, C. P. Wong, "The growth of carbon nanotube stacks in the kinetics-controlled regime", Carbon 45(2): 344-348 (2007)

[14] Y. Sun, L. Zhu, **H. Jiang**, C. P. Wong, "A paradigm of carbon nanotube interconnects in microelectronic packaging", Journal of Electronic Materials (revision)

[15] S. Panigrahi, S. Praharaj, S. Basu, K. Sujit, S. Jana, S. Pande, T. Vo-Dinh, **H. Jiang**, T. Pal, "Self-assembly of silver nanoparticles: synthesis, stabilization, optical properties, and application in surface-enhanced Raman scattering", Journal of Physical Chemistry B 110(27): 13436-13444 (2006)

A.3 Conference/Presentations

[16] H. Jiang, K. Moon, C. P. Wong, "Tin/Silver/Copper alloy nanoparticles pastes for low temperature lead-free interconnect applications", the IEEE 58th Electronic Components & Technology Conference, Orlando, Florida, May 27-30, (2008) (accepted)

[17] H. Jiang, M. Yim, K. Moon, Y. Li, C. P. Wong, "Novel nonconductive adhesives/films with carbon nanotubes for high performance interconnects", the IEEE 58th Electronic Components & Technology Conference, Orlando, Florida, May 27-30, (2008) (accepted)

[18] H. Jiang, K. Moon, F. Hua, C. P. Wong, "Thermal properties of tin/silver alloy nanoparticles for low temperature lead-free interconnect technology", the IEEE 57th

Electronic Components & Technology Conference, Reno, Nevada, May 29- June 1, p. 54-58 (2007)

[19] H. Jiang, L. Zhu, K. Moon, C. P. Wong, "Low temperature carbon nanotube film transfer via conductive adhesives", the IEEE 57th Electronic Components & Technology Conference, Reno, Nevada, May 29- June 1, p. 463-466 (2007)

[20] H. Jiang, K. Moon, F. Hua, C. P. Wong, "Tin/silver alloy nanoparticles for low temperature lead-free interconnect applications", Proceedings of 12th International Symposium on Advanced Packaging Materials: Processes, Properties and Interfaces, San Jose/Silicon Valley, CA, Oct. 3-5, 2007.

[21] H. Jiang, K. Moon, Y. Li and C. P. Wong, "Ultra High Conductivity of Isotropic Conductive Adhesives", The IEEE Proceedings of the 56th Electronic Components & Technology Conference 485-491 (2006).

[22] H. Jiang, K. Moon, F. Hua and C. P. Wong, "Thermal Properties of Oxide Free Nano Non Noble Metal for Low Temperature Interconnect Technology", The IEEE Proceedings of the 56th Electronic Components & Technology Conference 1969-1974 (2006).

[23] H. Jiang, K. Moon, Y. Li and C. P. Wong, "Ultra High Conductivity Polymer Composites for Lead-free Interconnect", PMSE preprints 94, 373-374 (2006).

[24] H. Jiang, K. Moon, H. Dong, F. Hua and C. P. Wong, "Synthesis and Thermal Properties of Tin Nanoparticles", The 231st ACS National Meeting, Atlanta, GA, March 26-30, 2006.

[25] H. Jiang, K. Moon, Y. Li and C. P. Wong, "Ultra Highly Conductive Polymer Composites for Lead-free Interconnect", Proceedings of 11th International Symposium on Advanced Packaging Materials: Processes, Properties and Interfaces, Atlanta, GA, March 15-17, 2006.

[26] H. Jiang, K. Moon, L. Zhu, J. Lu and C. P. Wong, "The Role of Self-Assembled Monolayer (SAM) on Ag Nanoparticles for Conductive Nanocomposite", Proceedings of 10th International Symposium on Advanced Packaging Materials, Irvine, CA, p. 266-271 (2005).

[27] H. Jiang, K. Moon and C. P. Wong, "Synthesis of Ag-Cu Alloy Nanoparticles for Lead-Free Interconnect Materials", Proceedings of 10th International Symposium on Advanced Packaging Materials, Irvine, CA, p. 173-177 (2005).

A.4 Patents/Invention Disclosures

[28] H. Jiang, L. Zhu, K. Moon, C. P. Wong, "Low Temperature Carbon Nanotube Film/Array Transfer via Polymer Composites" GT Invention No. 4094, (2007).

[29] M. Yim, H. Jiang, K. Moon, C. P. Wong, "Novel Anisotropic Conductive Adhesives/Films (ACA/Fs) and Nonconductive Adhesives/Films (NCA/Fs) with Carbon Nanotubes for High Performance Interconnects", GT Invention No. 4375, (2007).

[30] H. Jiang, K. Moon, and C. P. Wong, "Novel capping agents for oxide-free non noble metal nanoparticles", GT Invention No. 3955, (2006).

[31] H. Jiang, K. Moon, Y. Li, and C. P. Wong, "Ultra High Conductivity of Isotropic Conductive Adhesives", GT Invention No. 3648, (2005).

REFERENCES

[1] R. R. Tummala, “Fundamentals of Microsystems Packaging”, McGraw-Hill, New York, 2001.

[2] R. R. Tummala and V. Madisetti, "System on Chip or System on Package," IEEE Design and Test of Computer, Vol. 4, 48, 1999.

[3] M. Abtew and G. Selvaduray, “Lead-free Solders in Microelectronics**”,** *Mater. Sci. & Engi.: R: Rep.,* Vol. 27, 95, 2000.

[4] H. Jiang, K. Moon, Y. Li and C. P. Wong, “Surface functionalized silver nanoparticles for ultrahigh conductive polymer composites”, *Chem. of Mater.,* Vol. 18, 2969, 2006.

[5] Y. Li, K. Moon and C. P. Wong, “Enhancement of electrical properties of anisotropically conductive adhesive joints via low temperature sintering”, *J. Appl. Polym. Sci.* Vol. 99, 1665, 2006.

[6] M. J. Yim, S. J. Hwang, W. Kwon, K. W. Jang, K. W. Paik, “Highly reliable non-conductive adhesives for flip chip CSP applications”, *IEEE Trans. on Elec. Pack. Manu.* Vol. 26, 150, 2003.

[7] H. Xu, “Nanotubes: The logical choice for electronics?”, *Natur. Mater.,* Vol. 4, 649, 2005.

[8] A. P. Graham, G. S. Duesberg, W. Hoenlein, F. Kreupl, M. Liebau, R. Martin, B. Bajasekharan, W. Pamler, R. Seidel, W. Steinhoegl and E. Unnger, “How do carbon nanotubes fit into the semiconductor roadmap?”, *Appl. Phys. A,* Vol. 80, 1141, 2005.

[9] S. Berber, Y. K. Kwon and D. Tomanek "Unusually high thermal conductivity of carbon nanotubes", *Phys. Rev. Lett.,* Vol. 84, 4613, 2000.

[10] P. M. Ajayan, "Nanotubes from carbon", *Chem. Rev.,* Vol. 99**,** 1787, 1999.

[11] M. S. Dresselhaus, G. Dresselhaus and P. Avouris, *Carbon Nanotubes*; Springer: Berlin, 2001.

[12] L. B. Zhu, Y. H. Xiu, D. W. Hess and C. P. Wong, "Aligned carbon nanotube stacks by water-assisted selective etching", *Nano Lett.,* Vol. 5, 2641, 2005.

[13] L. B. Zhu , J. W. Xu, Y. H. Xiu, Y. Y. Sun, D. W. Hess and C. P. Wong, "Growth and electrical characterization of high-aspect-ratio carbon nanotube arrays", *Carbon,* Vol. 44, 253, 2006.

[14] G. Y. Zhang, D. Mann, L. Zhang, A. Javey, Y. M. Li, E. Yenilmez, Q. Wang, J. P. McVittie, Y. Nishi, J. Gibbons and H. J. Dai, "Ultra-high-yield growth of vertical single-walled carbon nanotubes: Hidden roles of hydrogen and oxygen", *Proceed. of Natal. Acad. Sci. U.S.A.* Vol. 102**,** 16141, 2005.

[15] H. J. Li, W. G. Lu, J. J. Li, X. D. Bai and C. Z. Gu, "Multichannel Ballistic Transport in Multiwall Carbon Nanotubes", *Phys. Rev. Lett.,* Vol. 95**,** 086601 1, 2005.

[16] L. B. Zhu, Y. Y. Sun, D. W. Hess and C. P. Wong, "Well-Aligned Open-Ended Carbon Nanotube Architectures: An Approach for Device Assembly", *Nano Lett.,* Vol. 6, 243, 2006.

[17] C. C. Chiu, T. Y. Tsai and N. H. Tai, "Field emission properties of carbon nanotube arrays through the pattern transfer process", *Nanotechnology,* Vol. 17, 2840, 2006.

[18] M. J. Kim, N. Nicholas, C. Kittrell, E. Haroz, H. Shan, T. J. Wainerdi, S. Lee, H. K. Schmidt, R. E. Smalley and R. H. Hauge, "Efficient transfer of a VA-SWNT film by a flip-over technique", *J. Am. Chem. Soc.,* Vol. 128, 9312, 2006.

[19] S. L. Lai, J. Y. Guo, V. Petrova, G. Ramanath, L. H. Allen, "Size-dependent Melting Properties of Small Tin Particles: Nanocalorimetric Measurements" *Phys. Rev. Lett.,* Vol. 77, 99, 1996.

[20] T. Bachels, H. J.Guntherodt and R. Schafer, "Melting of Isolated Tin Nanoparticles", *Phys. Rev. Lett.*, Vol. 85, 1250, 2000.

[21] R. Kofman, P. Cheyssac and F.Celestini, "Comment on "melting of isolated tin nanoparticles", *Phys. Rev. Lett.*, Vol. 86, 1388, 2001.

[22] M. Schmidt, R. Kusche, B. Issendroff and H. Haberland, "Irregular variations in the melting point of size-selected atomic clusters", *Nature,* Vol. 393, 238, 1998.

[23] S. J. Zhao, D. Y. Wang, H. Q. Cheng and H. Q. Ye, "Three distinctive melting mechanisms in isolated nanoparticles", *J. of Phys. Chem. B,* Vol. 105, 12857, 2001.

[24] F. Baletto, A. Rapallo, G. Rossi and R. Ferrando, "Dynamical effects in the formation of magic cluster structures", *Phys. Rev. B,* Vol. 69, 235421, 2004.

[25] F. G. Shi, "Size-dependent thermal vibrations and melting in nanocrystals", *J. Mater. Res.,* Vol. 9, 1307, 1994.

[26] J. Y. Kim, M. Kim, H. M. Kim, J. Joo and J. H. Choi, "Electrical and optical studies of organic light emitting devices using SWCNTs-polymer nanocomposites", *Opt. Mater.* Vol. 21, 147, 2003.

[27] W. Caseri, "Nanocomposites of polymers and metals or semiconductors: Historical background and optical properties", *Macromol. Rapid Commun.* Vol. 21, 705, 2000.

[28] A. Taleb, F. Silly, A. O. Gusev, F. Charra and M. P. Pileni, "Electron transport properties of nanocrystals: isolated, and "supra"-crystalline phases", *Adv. Mater.* Vol. 12, 633, 2000.

[29] S. Pothukuchi, Y. Li, and C. P. Wong, "Development of a novel polymer-metal nanocomposite obtained through the route of in situ reduction for integral capacitor application", *J. App. Polym. Sci.* Vol. 93, 1531, 2004.

[30] N. R. Jana, T. K. Sau, and T. Pal, "Growing small silver particle as redox catalyst", *J. Phys. Chem. B* Vol. 103, 115, 1999.

[31] M. P. Andrews and G. A. Ozin, "Liquid-phase agglomeration of silver atoms in olefinic and ether media: electrocatalytic application 2", *J. Phys. Chem.* Vol. 90, 2929, 1986.

[32] W. P. McConnell, J. P. Novak, L .C. Brousseau III, R. R. Fuierer, R. C. Tenent and D. L. Feldheim, "Electronic and optical properties of chemically modified metal nanoparticles and molecularly bridged nanoparticle arrays", *J. Phys. Chem. B* Vol. 104, 8925, 2000.

[33] C. P. Collier, R. J. Saykally, J. J. Shiang, S. E. Henrichs and J. R. Heath, "Reversible tuning of silver quantum dot monolayers through the metal-insulator transition", *Science* Vol. 277, 1978, 1997.

[34] Y. G. Sun and Y. N. Xia, "Shape-controlled synthesis of gold and silver nanoparticles", *Science* Vol. 298, 2176, 2002.

[35] Y. G. Sun, B. Mayers, T. Herricks and Y. N. Xia, "Polyol synthesis of uniform silver nanowires: A plausible growth mechanism and the supporting evidence", *Nano Lett.* Vol. 3, 955, 2003.

[36] M. P. Mallin and C. J. Murphy, “Solution-phase synthesis of sub-10 nm Au-Ag alloy nanoparticles”, *Nano Lett.* Vol. 2, 1235, 2002.

[37] C. Petit, P. Lixon and M. P. Pileni, “In situ synthesis of silver nanocluster in AOT reverse micelles”, *J. Phys. Chem*. Vol. 97, 12974, 1993.

[38] S. T. He, J. N. Yao, P. Jiang, D. X. Shi, H. X. Zhang, S. S. Xie, S. J. Pang and H. J. Gao, “Formation of silver nanoparticles and self-assembled two-dimensional ordered superlattice”, *Langmuir*, Vol. 17, 1571, 2001.

[39] T. Pal, D. S. Maity and A. Ganguly, “Use of a silver-gelatin complex for the determination of micro-amounts of hydrazine in water”, *Analyst*, Vol. 111, 1413, 1986.

[40] S. Link, Z. L. Wang and M. A. El-Sayed, “Alloy formation of gold-silver nanoparticles and the dependence of the plasmon absorption on their composition”, *J. Phys. Chem. B* Vol. 103, 3529, 1999.

[41] I. Pastoriza-Santos and L. M. Liz-Marzan, “Formation of PVP-protected metal nanoparticles in DMF”, *Langmuir* Vol. 18, 2888, 2002.

[42] G. Carotenuto, G. P. Pepe and L. Nicolais, “Preparation and characterization of nano-sized Ag/PVP composites for optical applications”, *Eur. Phys. J. B* Vol. 16, 11, 2000.

[43] T. Yamamoto, Y. Wada, T. Sakata, H. Mori, M. Goto, S. Hibino and S. Yanagida, “Microwave-assisted preparation of silver nanoparticles”, *Chem. Lett.* Vol. 33, 158, 2004.

[44] Y. H. Chen and C. S. Yeh, “A new approach for the formation of alloy nanoparticles: laser synthesis of gold-silver alloy from gold-silver colloidal mixtures”, *Chem. Commun.* Vol. 4, 371, 2001.

[45] M. C. Treguer, de Cointet, H. Remita, J. Khatouri, M. Mostafavi, J. Amblard, J. Belloni and R. de Keyzer, "Dose rate effects on radiolytic synthesis of gold-silver bimetallic clusters in solution", *J. Phys. Chem. B,* Vol. 102, 4310, 1998.

[46] S. Komarneni, D. S. Li, B. Newalkar, H. Katsuki and A. S. Bhalla, "Microwave-polyol process for Pt and Ag nanoparticles", *Langmuir* 18, 5959, 2002.

[47] T. Itakura, K. Torigoe and K. Esumi, "Preparation and characterization of ultrafine metal particles in ethanol by UV irradiation using a photoinitiator", *Langmuir* Vol. 11, 4129, 1995.

[48] W. Y. Yu, W. X. Tu and H. F. Liu, "Synthesis of nanoscale platinum colloids by microwave dielectric heating", *Langmuir* Vol. 15, 6, 1999.

[49] X. M. Fang and D. A. Scola, "Investigation of microwave energy to cure carbon fiber reinforced phenylethynyl-terminated polyimide composites, PETI-5/IM7", *J. Polym. Part A: Polym. Chem.* Vol. 37, 4616, 1999.

[50] K. Moon, Y. Li, J. W. Xu and C. P. Wong, "Lead-free solder interconnect by variable frequency microwave (VFM)", *IEEE Proceeding of the 54th Electronics Packaging Technology Conference*, Vol. 54, 1989, 2004.

[51] D. N. Fuelong, A. Launikonis and W. H. F. Sasse, "Colloidal platinum sols. preparation, characterization and stability towards salt", *J. Chem. Soc., Faraday Trans. 1*. Vol. 80, 571, 1984.

[52] S. A. Galema, "Microwave chemistry", *Chem. Soc. Rev.* Vol. 26, 233, 1997.

[53] R. N. Gedye, W. Rank and K. C. Estaway, "The rapid synthesis of organic-compounds in microwave-oven. 2", *Can. J. Chem.* Vol. 69, 706, 1991.

[54] S. M. Heard, F. Grieser, C. G. Barraclough and V. J. Sanders, "The characterization of Ag sols by electron microscopy, optical absorption, and electrophoresis", *J. Colloid Interface Sci.* Vol. 93, 545, 1983.

[55] H. H. Huang, X. P. Ni, G. L. Loy, C. H. Chew, K. L. Tan, F. C. Loh, J. F. Deng and G. Q. Xu, "Photochemical formation of silver nanoparticles in poly(*N*-vinylpyrrolidone)", *Langmuir* Vol. 12, 909, 1996.

[56] M. Mandal, S. K. Ghosh, S. Kundu, K. Esumi and T. Pal, "UV photoactivation for size and shape controlled synthesis and coalescence of gold nanoparticles in micelles", *Langmuir* Vol. 18, 7792, 2002.

[57] I. Lisiecki and M. P. Pileni, "Synthesis of copper metallic clusters using reverse micelles as microreactors", *J. Am. Chem. Soc.* Vol. 115, 3887, 1993.

[58] A. Henglein, "Small-particle research: physicochemical properties of extremely small colloidal metal and semiconductor particles", *Chem. Rev.* Vol. 89, 1861, 1989.

[59] Y. H. Chen and C. S. Yeh, "A new approach for the formation of alloy nanoparticles: laser synthesis of gold–silver alloy from gold–silver colloidal mixtures", *Chem. Commun.* Vol. 4, 371, 2001.

[60] M. P. Mallin and C. J. Murphy, "Solution-phase synthesis of sub-10 nm Au–Ag alloy nanoparticles", *Nano Lett.* Vol. 2, 1235, 2002.

[61] K. Mallik, M. Mandal, N. Pradhan and T. Pal, "Seed mediated formation of bimetallic nanoparticles by UV irradiation: A photochemical approach for the preparation of "core-shell" type structures", *Nano Lett.* Vol. 1, 319, 2001.

[62] Y. B. Zhao, Z. J. Zhang and H. X. Dang, "Fabrication and tribological properties of Pb nanoparticles", *J. Nano. Res.* Vol. 6, 47, 2004.

[63] Y. B. Zhao, Z. J. Zhang and H. X. Dang, "Synthesis of In-Sn alloy nanoparticles by a solution dispersion method", *J. Mater. Chem.* Vol. 14, 299, 2004.

[64] B. J. Wiley, Z. Wang, J. Wei, Y. Yin, D. H. Cobden and Y. N. Xia, "Synthesis and electrical characterization of silver nanobeams", *Nano Lett.* Vol. 6, 2273, 2006.

[65] H. H. Huang, X. P. Ni, G. L. Loy, C. H. Chew, K. L, Tan, F. C. Loh, J. F. Deng and G. Q. Xu, "Photochemical formation of silver nanoparticles in poly(*N*-vinylpyrrolidone)", Langmuir Vol. 12, 909, 1996.

[66] A. Pal, K. Esumi and T. Pal, "Preparation of nanosized gold particles in a biopolymer using UV photoactivation", *J. Coll. Int. Sci.* Vol. 288, 396, 2005.

[67] J. Petroski and M. A. El-Sayed, "FTIR study of the adsorption of the capping material to different platinum nanoparticle shapes", *J. Phys. Chem. A* Vol. 107, 8371, 2003.

[68] P. Buffat, J. P. Borel, "Size effect on melting temperature of gold particles", *Phys. Rev. A* Vol. 13, 2287, 1976.

[69] Y. Kwon, M. G. Kim, Y. Kim, Y. Lee, J. Cho, "Effect of capping agents in tin nanoparticles on electrochemical cycling", *Electrochemical and Solid-State Lett.* Vol. 9, A34, 2006.

[70] Y. Wang, J. Y. Lee, T. C. Deivaraj, "Controlled Synthesis of V-shaped SnO_2 Nanorods", *J. Phys. Chem. B* Vol. 108, 13589, 2004.

[71] Y. Imry, D. Bergman, "Critical points and scaling laws for finite system", *Phys. Rev. A* Vol. 3, 1416, 1971.

[72] K. J. Hanszen, "Theoretische untersuchungen uber den schmelzpunkt kleiner kugelchen – ein beitrag zur thermod ynamik der grenzflachen", *Z. Phys.* Vol. 157, 523, 1960.

[73] F. Ercolessi, W. Andreoni, E. Tosatti, "Melting of small gold particles – mechanism and size effect", *Phys. Rev. Lett.* Vol. 66, 911, 1991.

[74] I. Artaki, A. M. Jackson and P. T. Vianco, "Evaluation of lead-free solder joints in electronic assemblies", *J. Electron. Mater.* Vol. 23, 757, 1994.

[75] L. Y. Hsiao and J. G. Duh, "Synthesis and characterization of lead-free solders with Sn-3.5Ag-xCu (x=0.2, 0.5, 1.0) alloy nanoparticles by the chemical reduction method", *J. Electrochem. Soc.* Vol. 152, J105, 2005.

[76] H. J. Jiang, K. Moon, H. Dong, F. Hua and C. P. Wong, "Size-dependent melting properties of tin nanoparticles", *Chem. Phys. Lett.* Vol. 429, 492, 2006.

[77] H. J. Jiang, K. S. Moon and C. P. Wong, *US Patent Pending*.

[78] H. L. Lai, J. G. Duh, "Lead-free Sn-Ag and Sn-Ag-Bi solder powders prepared by mechanical alloying", *J. Electron. Mater.* Vol. 32, 215, 2003.

[79] L. Balan, R. Schneider, D. Billaud, and J. Ghanbaja, "A new organometallic synthesis of size-controlled tin(0) nanoparticles", *Nanotechnol.* Vol. 16, 1153, 2005.

[80] F. Banhart, E. Hernandez, and M. Terrones, "Extreme superheating and supercooling of encapsulated metals in fullerenelike shells", *Phys. Rev. Lett.* Vol. 90, 185502-1, 2003.

[81] H. K. Christenson, "Confinement effects on freezing and melting", *J. Phys. Condens. Matter.* Vol. 13, R95, 2001.

[82] Y. Imry, and D. Bergman, "Critical points and scaling laws for finite systems", *Phys.*

Rev. A Vol. 3, 1416, 1971.

[83] R. Garrigos, P. Cheyssac, R. Kofman, "Melting for lead particles of very small sizes-influence of surface phenomena", *Z. Phys. D* Vol. 12, 497, 1989.

[84] W. Y. Hu, S. F. Xiao, J. Y. Yang and Z. Zhang, "Melting evolution and diffusion behavior of vanadium nanoparticles", *Eur. Phys. J. B* Vol. 45, 547, 2005.

[85] C. Wu, D. Yu, C. Law and L. Wang, "Properties of lead-free solder alloys with rare earth element additions", *Mater. Sci. Eng. R* Vol. Vol. 44, 1, 2004.

[86] H. Jiang, K. Moon, F. Hua, and C. P. Wong, "Synthesis and thermal and wetting properties of tin/silver alloy nanoparticles for low-melting point lead-free solders", *Chem. Mater.* Vol. 19, 4482, 2007.

[87] B.T. Alpert and A.J. Schoenberg, "*Conductive adhesives as a soldering alternative"*, (Electronic Packaging and Production, 1991), pp. 130-132.

[88] S. K. Kang, R. S. Rai, and S. Purushothaman, "Development of High Conductivity Lead (Pb)-free Conducting Adhesives," *IEEE Transactions on Components, Packaging, and Manufacturing Technology, Part A*, Vol. 21,18, 1998.

[89] B. Trumble, "Get the Lead Out," IEEE spectrum, May p. 55-60, 1998.

[90] S. K. Kang and A. Sarkel, "Lead (Pb)-free Solders for Electronic Packaging," *J. Electron. Mater.* Vol. 23, 701, 1994.

[91] C. P. Wong, K. Moon and Y. Rao, "Fundamental Understandings of Anisotropic Conductive Adhesives for Flip-Chip Application," *2003, NSF Design, Service and Manufacturing Grantees and research Conference*, Jan 2003.

[92] Y. Li, K. Moon and C. P. Wong, "Formation of Self Assembled Monolayer (SAM) on Metal Surfaces for High Performance Anisotropically Conductive Adhesives," *9th Int'l*

Symposium on Advanced Packaging Materials, p. 139-144, 2004.

[93] S. Corbett and M. J. Dominao, "Processing with Polymer Solders," *Surface Mount Technology,* 48, June 1997.

[94] D. J. Small, B. Eisenach, A. Lewis, and A. Babiarz, "Electrically Conductive Adhesives as an Alternative to Solder," *Advanced Packaging*, 38, Jan, 1999.

[95] S. Kotthaus, B.H. G¨unther, R. Haug, and H. Sch¨afer, "Study of isotropically conductive bondings filled with aggregates of nano-sized Ag-particles", *IEEE Trans. Comp. Packaging Manufacturing Technol. Part A* 20, 15, 1997.

[96] L. Ye, Z.H. Lai, J. Liu and A. Th¨ol´en, "*IEEE Trans. Electron. Packaging Manufacturing* 22, 1999.

[97] H. Dong, K.S. Moon, C.P. Wong, "Molecular dynamics study on coalescence of Cu nanoparticles and their deposition on Cu substrate", *J. Electron. Mater.* 34, 40, 2005.

[98] H. Dong, K.S. Moon, C.P. Wong, "Molecular dynamics study of nano silver particles for low temperature lead free interconnect applications", *J. Electron. Mater.* 33, 1326, 2004.

[99] A. Singhal, G. Skanda, A. Wang, N. Glumac, B.H. Kear, R.D. Hunt, "On nanoparticle aggregation during vapor phase synthesis", *Nanostructured Mater.* 11, 545, 1999.

[100] J. Y. Kim, M. Kim, H. M. Kim, J. Joo and J. H. Choi, "Electrical and optical studies of organic light emitting devices using SWCNTs-polymer nanocomposites", *Opt. Mater.* Vol. 21, 147, 2003.

[101] T. Vu-Khanh, B. Sanschagrin and B. Fisa, "Fracture of mica-reinforced polypropylene – Mica concentration effect", *Polym. Compos.* Vol. 6, 249, 1985.

[102] V. Khrenov, M. Klapper, M. Koch and K. Mullen, “Surface functionalized ZnO particles designed for the use in transparent nanocomposites”, *Macromol. Chem. Phys.* Vol 206, 95, 2005.

[103] C. J. Sandroff, S. Garoff and K. P. Leung, “Surface-enhanced Raman-study of the solid-liquid interface – conformational –changes in absorbed molecules”, *Chem. Phys. Lett.* Vol. 22, 547, 1983.

[104] J. A. Creighton, “Surface Raman electroma gnetic enhancement factors for molecules at the surface of small isolated metal spheres – The determination of adsorbate orientation from sers relative intensitivities”, *Surf. Sci.* Vol. 124, 209, 1983.

[105] M. Moskovits and J. S. Suh, “Conformation Of Mono-Carboxylic and Dicarboxylic-acids Adsorbed On Silver Surfaces”, *J. Am. Chem. Soc.* Vol. 107, 6826, 1985.

[106] H. Wolfson and G. Elliott, “Electrically Conducting Cements Containing Epoxy Resins and Silver”, *U.S. Patent* 2774747, 1956.

[107] Y. Li, K. Moon and C. P. Wong, “Electronics without Lead", *Science* Vol. 308, 1419, 2005.

[108] J. M. Kim, K. Yasuda and K. Fujimoto, “Novel interconnection method using electrically conductive paste with fusible filler”, *J. Electron. Mater.* Vol. 34, 600, 2005.

[109] L. Q. Cao, Z. H. Lai and J. H. Liu, “Interfacial adhesion of anisotropic conductive adhesives on polyimide substrate”, *J. Electron Packaging*, Vol. 127, 43, 2005.

[110] Y. Li, K. S. Moon and C. P. Wong, “Adherence of self-assembled monolayers on gold and their effects for high-performance anisotropic conductive adhesives”, *J. Electron. Mater.* Vol. 34, 266, 2005.

[111] H. Chiang, C. Chung, L. Chen, Y. Li and C. P. Wong, "Processing and shape effects on silver paste electrically conductive adhesives (ECAs)", *J. Adhesion. Sci. Technol.* Vol**.** 19, 565, 2005.

[112] S. K. Kang, R. S. Rai, and S. Purushothaman, "Development of high conductivity lead (Pb) free conducting adhesives", *IEEE Trans. Comp. Packaging Manufacturing Technol. Part A*, Vol. 21, 18, 1998.

[113] H. J. Jiang K. S. Moon, Y. Li and C. P. Wong, "Ultra high conductive isotropic conductive adhesives", *Invention Disclosure GTID 3648*: Atlanta, 2005.

[114] N. J. Welham, "Formation and characterization of germanium nanoparticles", *J. Mater. Res.* Vol. 15, 2400, 2000.

[115] L. Qi, B. I. Lee, S. Chen, W. D. Samuels and G. J. Exarhos, "High-dielectric-constant silver-epoxy composites as embedded dielectrics", *Adv. Mater.* Vol. 17, 1777, 2005.

[116] Y. Yosida, "High-temperature shrinkage of single-walled carbon nanotube bundles up to 1600K", *J. Appl. Phys.* Vol. 87, 3338, 2000.

[117] H. Jiang, L. Zhu, K. Moon and C. P. Wong, "The preparation of stable metal nanoparticles on carbon nanotubes whose surfaces were modified during production" *Carbon* Vol. 45, 655, 2007.

[118] M. B. Bryning, D. E. Milkie, M. F. Islam, J. M. Kikkawa and A. G. Yodh, "Thermal conductivity and interfacial resistance in single-wall carbon nanotube epoxy composites", *Appl. Phys. Lett.* Vol. 87, 161909-1-3, 2005.

[119] F. H. Gojny, M. G. Wichmann, B. Fiedler, I. A. Kinloch, W. Bauhofer, A. H. Windle and K. Schutle, "Evaluation and identification of electrical and thermal

conduction mechanisms in carbon nanotube/epoxy composites", *Polymer* Vol. 47, 2036, 2006.

[120] A. Moisala, Q. Li, I. A. Kionloch and A. H. Windle, "Thermal and electrical conductivity of single- and multi-walled carbon nanotube-epoxy composites", *Comp. Sci. Tech.* Vol. 66, 1285, 2006.

[121] X Peng, L. Manna, W. Yang, J. Wickham, E. Scher, A. Kadavanich, et al. "Shape control of CdSe nanocrystals", *Nature* Vol. 404, 59, 2000.

[122] H. Weller, "Colloidal semiconductor Q-particles-chemistry in the transition region between solid-state and molecules", *Angew. Chem. Int. Ed. Engl.* Vol. 32, 41, 1993.

[123] Y. G. Sun, Y. D. Yin, B. T. Mayers, T. Herricks, Y. N. Xia, "Uniform silver nanowires synthesis by reducing $AgNO_3$ with ethylene glycol in the presence of seeds and poly(vinyl pyrrolidone)", *Chem. Mater.* Vol. 14, 4736, 2002.

[124] G. S. Metraux, Y. C. Cao, R. C. Jin, C. A. Mirkin, "Triangular nanofrarnes made of gold and silver", *Nano. Lett.* Vol. 3, 519, 2003.

[125] T. Yamamoto, Y. Wada, T. Sakata, H. Mori, M. Goto, S. Hibino, et al. "Microwave-assisted preparation of silver nanoparticles", *Chem. Lett.* Vol. 33,158, 2004.

[126] J. P. Gao, J. Fu, C. K. Lin, J. Lin, Y. C. Han, X. Yu, et al. "Formation and photoluminescence of silver nanoparticles stabilized by a two-armed polymer with a crown ether core", *Langmuir* Vol. 20, 9775, 2004.

[127] K. C. Chin, A. Gohel, W. Z. Chen, H. I. Elim, W. Ji, G. L. Chong, et al. "Gold and silver coated carbon nanotubes: An improved broad-band optical limiter", *Chem. Phys. Lett.* Vol. 409, 85, 2005.

[128] D. J. Guo, H. L. Li, "Highly dispersed Ag nanoparticles on functional MWNT surfaces for methanol oxidation in alkaline solution", *Carbon* Vol. 43,1259, 2005.

[129] B. Xue, P. Chen, Q. Hong, J. Y. Lin, K. L. Tan, "Growth of Pd, Pt, Ag and Au nanoparticles on carbon nanotubes", *J. Mater. Chem.* Vol. 11, 2378, 2001.

[130] Y. T. Kim, K. Ohshima, K. Higashimine, T. Uruga, M. Takata, H. Suematsu, et al. "Fine size control of platinum on carbon nanotubes: From single atoms to clusters", *Angew. Chem. Int. Ed.* Vol. 45, 407, 2006.

[131] M. A. Correa-Duarte, J. Perez-Juste, A. Sanchez-Iglesias, M. Giersig, L. M. Liz-Marzan, "Aligning an nanorods by using carbon nanotubes as templates", *Angew. Chem. Int. Ed.* Vol. 44, 4375, 2005.

[132] B. Yoon, C. M. Wai, "Microemulsion-templated synthesis of carbon nanotube-supported Pd and Rh nanoparticles for catalytic applications", *J. Am. Chem. Soc.* Vol. 127, 17174, 2005.

[133] L. T. Qu, L. M. Dai, E. Osawa, "Shape/size-control led syntheses of metal nanoparticles for site-selective modification of carbon nanotubes", *J. Am. Chem. Soc.* Vol. 128, 5523, 2006.

[134] B. C. Satishkumar, E. M. Vogl, A. Govindaraj, C. N. R. Rao, "The decoration of carbon nanotubes by metal nanoparticles", *J. Phys. D: Appl. Phys.* Vol. 29, 3173, 1996.

[135] L. H. Qiu, V. G. Pol, Y. Wei, A. Gedanken, "Sonochemical decoration of multi-walled carbon nanotubes with nanocrystalline tin", *New. J. Chem.* Vol. 28, 1056, 2004.

[136] S. D. Oh, B. K. So, S .H. Choi, A. Gopalan, K. P. Lee, K. R. Yoon, et al. "Dispersing of Ag, Pd, and Pt-Ru alloy nanoparticles on single-walled carbon nanotubes by gamma-irradiation", *Mater. Lett.* Vol. 59,1121, 2005.

[137] S. C. Tsang, P. J. F. Harris, M. L. H.Green, "Thinning and opening of carbon nanotubes by oxidation using carbon-dioxide", *Nature* Vol. 362, 520, 1993.

[138] C. Gomez-Navarro, P. J. De Pablo, J. Gomez-Herrero, B. Biel, F. J. Garcia-Vidal, A. Rubio, F. Flores, "Tuning the conductance of single-walled carbon nanotubes by ion irradiation in the Anderson localization regime", *Nature Mater.* Vol. 4, 534, 2005.

[139] A. Felten, C. Bittencourt, J. J. Pireaux, G. Van Lier, J. C. Charlier, "Radio-frequency plasma functionalization of carbon nanotubes surface O_2, NH_3, and CF_4 treatments", *J. Appl. Phys.* Vol. 98, 074308-1, 2005.

[140] C. D. Stinespring, J. C. Wormhoudt, "Surface studies relevant to silicon carbide chemical vapor deposition", *J. Appl. Phys.* Vol. 65, 1733, 1999.

[141] B. Kim, W .M. Sigmund, "Functionalized multiwall carbon nanotube/gold nanoparticles composites", *Langmuir* Vol. 20, 8239, 2004.

[142] R. V. Hull, L. Li, Y. C. Xing, C. C. Chusuei, "Pt nanoparticles binding on functionalized multiwalled carbon nanotubes", *Chem. Mater.* Vol. 18, 1780, 2006.

[143] Y. Wang, J. Y. Lee, T. C. Deivaraj, "Tin nanoparticle loaded graphite anodes for Li-ion battery applications", *J. Electrochem. Soc.* Vol. 151, A1804, 2004.

[144] S. W. Gaarenstroom, N. Winograd, "Initial and final state effects in the ESCA sectra of cadmium and silver oxides", *J. Chem. Phys.* Vol. 67, 3500, 1977.

[145] X. Hu, T. Wang, X. Qu, S. Dong, "In situ synthesis and characterization of multiwalled carbon nanotube/Au nanoparticle composite materials", *J. Phys. Chem. B* Vol. 110, 853, 2006.

[146] C. Bittencourt, A. Felten, B. Douhard, J. Ghijsen, R L. Johnson, W. Drube, J. J. Pireaux, "Photoemission studies of gold clusters thermally evaporated on multiwall carbon nanotubes", *Chem. Phys.* Vol. 328, 385, 2006.

[147] H. J. Jiang, K. S. Moon, Y. Li and C P Wong, "Surface functionalized silver nanoparticles for ultrahigh conductive polymer composites", *Chem. Mater.* Vol. 18, 2969, 2006.

[148] P. Laibinis, G. M. Whitesides, "Self-assembled monolayers of n-alkanethiolates on copper are barrier films that protect the metal against oxidation by air", *J. Am. Chem. Soc.* Vol. 114, 9022, 1992.

[149] H. Rieley, G. K. Kemdall, F. W. Zemicael, T. L. Smith and S. Yang, "X-ray studies of self-assembled monolayers on coinage metals. 1. Alignment and photooxidation in 1,8-octanedithiol and 1-octanethiol on Au", *Langmuir* Vol. 14, 5147 1998.

[150] C. M. L. Wu, D. Q. Yu, C. M. T. Law and L. Wang, "Improvements of microstructure, wettability, tensile and creep strength of eutectic Sn–Ag alloy by doping with rare earth elements", *J. Mater. Res.* Vol. 31, 3146–3154, 2002.

[151] C. M. L. Wu, D. Q. Yu, C. M. T. Law and L. Wang, "Microstructure and mechanical properties of new lead-free Sn–Cu–RE solder alloys", *J. Electron. Mater.* Vol. 31, 928–932, 2002.

[152] C. M. L. Wu, C. M. T. Law, D. Q. Yu and L. Wang, "The wettability and microstructure of Sn–Zn–RE alloys", *J. Electron. Mater.* Vol. 32, 63–69, 2003.

[153] C. M. L. Wu, D. Q. Yu, C. M. T. Law and L. Wang, "Properties of lead-free solder alloys with rare earth element additions", *Mater. Sci. Engi. R*, Vol. 44, 1-44, 2004.